

**Universität
Rostock**



Traditio et Innovatio

Suspended Sediment Transport near Sloping Topography

Dissertation

zur

Erlangung des akademischen Grades

doctor rerum naturalium (Dr. rer. nat.)

der Mathematisch-Naturwissenschaftlichen Fakultät

der Universität Rostock

vorgelegt von

Kirstin Schulz, geb. am 10. Januar 1988 in Clausthal-Zellerfeld

Gutachter:

1. Gutachter:

PD Dr. Lars Umlauf,

Leibniz Institute for Baltic Sea Research, Warnemünde

2. Gutachter:

Assistent Professor Dr. Henk Schuttelaars,

Delft Institute of Applied Mathematics, TU Delft

Datum der Einreichung: 07. Oktober 2016

Datum der Verteidigung: 17. Februar 2017

Abstract

Sediment transport is governed by the complex interplay of many different processes. Near sloping topography, sediment transport can be triggered by asymmetries in the density stratification during an oscillatory current going up and down the slope. This process was investigated in detail by means of an idealized numerical model. It was found that the process depends on the strength of the vertical stratification and the slope angle, and residual sediment transport is directed upslope for most of the parameter constellations. A more profound numerical model was used to successfully reproduce observations of this process from the East China Sea, and to investigate the effect of Earth rotation. Another data set was analyzed to investigate sediment dynamics across the rim of a deep basin in the Baltic Sea. It was found that parts of the sediment transported there are dispersed across the bottom slope into shallower areas.

Zusammenfassung

Der Transport von Sedimenten wird von dem komplexen Zusammenspiel vieler verschiedener Prozesse bestimmt. Nahe eines geneigten Meeresbodens können Asymmetrien in der vertikalen Dichteschichtung während der Phasen einer oszillierenden Strömung quer zum Hang einen residuellen Sedimenttransport verursachen. Dieser Prozess wurde mit der Hilfe eines idealisierten numerischen Modells detailliert untersucht. Es hat sich gezeigt, dass die Stärke der vertikalen Dichteschichtung und der Winkel des Hanges großen Einfluss auf diesen Prozess haben, der residuelle Sedimenttransport aber für den Großteil der Parameterkombinationen hangaufwärts gerichtet ist. Das Modell wurde erweitert, um erfolgreich Beobachtungen dieses Prozesses aus dem Ostchinesischen Meer zu reproduzieren und um den Einfluss der Erdrotation zu bestimmen. Ein weiteres Datenset wurde analysiert um die Sedimentdynamik am Hang eines tiefen Beckens in der Ostsee zu untersuchen. Es wurde herausgefunden, das Sediment, welches einmal in das Becken hinein transportiert wurde, auch wieder in Richtung flacherer Gebiete verteilt werden kann.

Acknowledgements

I like to express my deep gratitude to the people who surrounded and supported me during my PhD time. In the last three years I did not only get to know a totally new field of scientific work, but I met unbelievably wonderful people that made my time in Rostock to be a great experience.

In first place, I thank my supervisor Lars Umlauf, who invested so much time and energy to make a physicist out of me. Thank you for encouraging me all the time and thank you for all your advice, and for helping me through the hard times when nothing went right.

I also thank the other three members of my thesis committee: Hans Burchard, thank you for introducing me to all the people on the conferences and for always offering your help. You were like a second supervisor for me. Henk Schuttelaars, thank you for all the wonderful conversations, in Havard as well as on the Christmas Market, and your advice on my work and my future. And finally Gregor Rehder, who was the most sympathetic chief scientist I ever went on a cruise with.

I greatly thank my working group and the colleagues from the project. Thanks to all the people that shared some time in room 214 with me: Mahdi Mohammadi-Aragh, who helped me so much during my first time and provided me with the most important schedule ever, Kaveh Purkiani and Johannes Becherer, Merten Siegfried, Selina Müller and Madline Kniebusch, who all contributed to the familiar and relaxed atmosphere in our office. Special thanks goes to Chris Lappe, who untiringly answered all my questions about oceanography and who tried to explain internal waves to me at least a hundred times. Thanks to GETMan Knut Klingbeil, for permanent support with everything related to computers, and for your ability to encourage me. Thanks to Elisabeth Schulz, who I always looked up to. Thanks to Peter Holtermann for showing me Galvano, to Ulf Gräwe, Xaver Lange and Berkay Basdurak for providing support and a wonderful and relaxed working atmosphere. Thanks to Berit Recklebe for being the shield to protect me from administration and for being a friend from my first working day on. I also want to thank Toralf Heene and Sebastian Beier for the technical support and their patience with me, and of course the crew members of the research vessels Alkor, Elisabeth Mann Borgese and Maria S. Merian. Thanks to my biologist Dr. David Kaiser, and Claudia Morys, Dennis Bunke, Jana Wölfel, Mayya Gogina, Florian Cordes and Julia Regnery, who made the ships cruises an unforgettable experience and became my closest friends during my time in Rostock.

I am so grateful that I had the opportunity to meet all of you and I hope we will stay in touch.

I also want to express my gratitude to Prof. Dr. Margit Rösler, who was my mentor during my years at the Technical University of Clausthal-Zellerfeld, and who taught me to never surrender to a problem. I would also like to thank Wiebke Klünder and Markus Schreiber for always being there for me, during study times and beyond.

In the end, I want to thank my perfect flatmate Josephina Seltenheim, for providing me shelter when I came to Rostock and for being such a wonderful person, and all my other friends in Berlin. I always loved to have you around. I want to thank my best friend Jennifer Smoch for your endless support with anything and the wonderful times we have together and my partner Christian Meier for his patience and for moving to the Netherlands with me. I thank my family, my grandmother Eva Eggeling and especially my mother Maike, for creating a wonderful childhood for me and for supporting me in every possible way. Everything I have achieved so far I owe to you. I thank my amazing brother Paul for all the years we have been together and my father Uwe for everything he did for me. Finally, I particularly want to thank Marko Lipka, who shared his apartment, Socke the dog and his small family with me for the last two years. You and Klara were such a huge and wonderful part of my life here and I will miss you so much. Goodbye und Guten Flug.

Regarding the publications in chapter 2 and 3: These studies were carried out in the context of the interdisciplinary project SECOS, funded by the German Federal Ministry of Education and Research under grant 03F0666A, WP 2.1 (PI: Lars Umlauf). We are grateful to Henk Schuttelaars (TU Delft), Hans Burchard, Ulf Gräwe, Knut Klingbeil, and Jan-Torben Witte (all IOW) for modeling support and helpful comments on the manuscripts. Computations were carried out with a modified version of General Ocean Turbulence Model (GOTM, www.gotm.net) with the SPM component implemented using the Framework for Aquatic Biogeochemical Models (FABM, www.sf.net/projects/fabm). Observational data used in chapter 3 are available from co-author T. Endoh upon request

Contents

1. Introduction	1
2. Suspended material transport by tidal straining near sloping topography	3
2.1. Introduction	3
2.2. Geometry and governing equations	6
2.2.1. Geometry	6
2.2.2. Equations of motion	8
2.2.3. Boundary-layer forcing and resonance	9
2.2.4. Erosion and transport of suspended material	10
2.2.5. Residual transports	11
2.3. Boundary-layer dynamics and sediment transport	12
2.3.1. Boundary-layer dynamics	12
2.3.2. Residual results	15
2.3.3. Supercritical slopes	19
2.4. Non-dimensional description	22
2.4.1. Non-dimensional equations	22
2.4.2. Non-dimensional fluxes	24
2.4.3. Parameter space	24
2.5. Non-dimensional simulations	25
2.5.1. Supercritical forcing	26
2.5.2. Subcritical forcing	28
2.5.3. The effect of the slope angle	29
2.6. Discussion and conclusions	30
3. Slope-induced tidal straining: Analysis of rotational effects	35
3.1. Introduction	35
3.2. Model description	38
3.2.1. Model geometry	38
3.2.2. Model equations	39

3.2.3. Model properties	41
3.3. Study site and methods	43
3.3.1. Study site	43
3.3.2. Methods	45
3.3.3. Analysis of tidal motions	46
3.4. Observations and model parameters	47
3.4.1. Observations	47
3.4.2. Model parameters	50
3.5. Modeling slope-induced tidal straining	52
3.6. Dynamics of suspended material	55
3.6.1. Temporal variability	55
3.6.2. Residual transports	57
3.6.3. Variable sinking speed and stratification	60
3.6.4. Rotational effects	62
3.7. Conclusions	65
4. The Baltic Sea	67
4.1. Present hydrography and dynamics	67
4.2. Wave climate	70
4.2.1. Wave model setup and verification	71
4.2.2. Wave-Induced Bottom Friction Velocity Distribution	72
4.3. German Coastal Seas and Sediment	75
5. Near-bottom turbulence and sediment transport in the Western Baltic Sea	77
5.1. Introduction	77
5.2. Study Area	79
5.2.1. Hydrography and dynamics	79
5.2.2. Sedimentology	85
5.3. Instrumentation	86
5.4. Observations	88
5.4.1. Arkona Basin	89
5.4.2. Transect from basin to the coast	90
5.4.3. Tromper Wiek	91
5.5. Discussion	95
5.6. Conclusions	97
A. Numerical boundary conditions for SPM concentrations	i

B. Sensitivity with respect to other model parameters (study in chapter 3)	v
C. Second-order Turbulence Closure Models	vii
C.1. Introduction	viii
C.2. Pressure Redistribution Models	ix
C.3. Explicit Algebraic Models	ix
C.4. Closure for k	x
C.5. Closure for l or ε	xi
C.5.1. Calculation of c_{mn3}	xii
C.6. Stability functions	xiii
C.7. Parameters for the Turbulence Model	xiii
D. State of the art wind wave modeling	xv
D.1. Evolution of Waves	xv
D.1.1. Wave Generation by Wind	xv
D.1.2. Wave-wave Interaction	xvii
D.1.3. Dissipation of Energy	xviii
D.2. Sea State Description	xviii
D.3. Third Generation Wave Model SWAN	xx
D.3.1. Wave generation by wind	xxi
D.3.2. Nonlinear wave – wave interaction	xxii
D.3.3. Dissipation	xxiii

Bibliography

xxvii

Chapter 1.

Introduction

The state of marine sediments is closely linked to the conditions and processes prevailing in the overlying water column. Discharged material, nutrients as well as pollutants, can be stored and transformed in the sediment, and released into the water column again. Additionally, the sea floor provides a habitat for numerous species in complex and fragile ecosystems. Sediment resuspension, transport, and deposition highly influence the above, and sediment dynamics are therefore of great interest for the understanding of this complex system. An interplay of countless physical processes determines the spreading of sediments. In this thesis, a process for sediment transport in the vicinity of a sloping bottom is investigated.

Motivated by the outcome of studies on estuarine dynamics controlling sediment transport processes, a basic process study on sediment transport, induced by an oscillatory current moving over sloping topography, was carried out. The prerequisite of the investigated sediment transport process is, besides the vicinity to a bottom slope, only a vertical density stratification of the water column. These conditions are prevailing in many regions throughout the ocean, for example on continental shelves or near underwater basins. The investigated sediment transport process might therefore play an important role for the sediment dynamics all over the ocean. It was found that sediment is transported up the slope under most of the naturally occurring conditions. This study was published in 2016 in the *Journal of Physical Oceanography* under the title "Residual transport of suspended material by tidal straining near sloping topography" and is found in chapter 2 of this thesis.

During the creation of the model study, observational data from the East China Sea, which gave evidence for the natural occurrence of the investigated process, was analyzed and is now published in Endoh et al. [2016]. A second model study was

carried out, aiming on the reproduction of the observations. Therefore, the numerical model was extended to include the effects of Earth rotation, which had been neglected in the previous study. Even though the model domain is only one-dimensional, the important points of the observed process were reproduced and the natural occurrence of slope-induced tidal straining was confirmed. Another important aim of this study was the investigation of the influence of the Coriolis force on the process, which had been neglected previously. This study was submitted to the *Journal of Geophysical Research* in October 2016, and the submitted version is included as chapter 3 in this thesis.

Besides the two model studies, ship-based field campaigns in coastal areas of the Baltic Sea were performed in the context of this thesis. An extensive data set, including microstructure turbulence data, was obtained. Parts of these data, which were obtained in the transition zone from a shallow area near the coast to a deeper basin, have been analyzed to investigate the sediment dynamics in the vicinity of the basin slope. Evidence for processes that transport parts of the sediment from the deep parts of the basin back to the shore were found. In chapter 4, general information about the Baltic Sea, with focus on near-bottom processes important for sediment resuspension and transport, are summarized. The data are the discussed in chapter 5.

Chapter 2.

Suspended material transport by tidal straining near sloping topography

Tidal straining is known to have an important impact on the generation of residual currents and the transport of suspended material in estuaries and the coastal ocean. Essential for this process is an externally imposed horizontal density gradient, typically resulting from either freshwater runoff or differential heating. Here, we show that near *sloping* topography, tidal straining may effectively transport suspended material across isobaths even if freshwater runoff and differential heating do not play a significant role. A combined theoretical and idealized modeling approach is used to illustrate the basic mechanisms and implications of this new process. The main finding of this study is that, for a wide range of conditions, suspended material is transported upslope by a pumping mechanism that is in many respects similar to classical tidal pumping. Downslope transport may also occur, however, only for the special cases of slowly sinking material in the vicinity of slopes with a slope angle larger than a critical threshold. The effective residual velocity at which suspended material is transported across isobaths is a significant fraction of the tidal velocity amplitude (up to 40% in some cases), suggesting that suspended material may be transported over large distances during a single tidal cycle. [Schulz and Umlauf 2016]

2.1. Introduction

Subtidal circulation and residual transport of suspended material in estuaries and the coastal ocean is known to be tightly connected to the presence of horizontal density

gradients, generated by either river runoff, differential heating, or differential evaporation. The most obvious dynamical implication of such horizontal density differences is the generation of a gravitationally-driven residual circulation with a landward transport of dense waters near the bottom, and a seaward return current above [Pritchard 1952; MacCready and Geyer 2010].

Residual currents may also be triggered by periodic variations of stratification induced by the oscillatory vertical shear of a tidal flow acting on the horizontal density gradient. This mechanism leads to a periodic “tidal straining” of the horizontal density gradient [Simpson et al. 1990], resulting in weak or even convectively unstable stratification during flood, and therefore in significantly larger turbulent diffusivities compared to the more stably stratified ebb period (Fig. 2.1a,c).

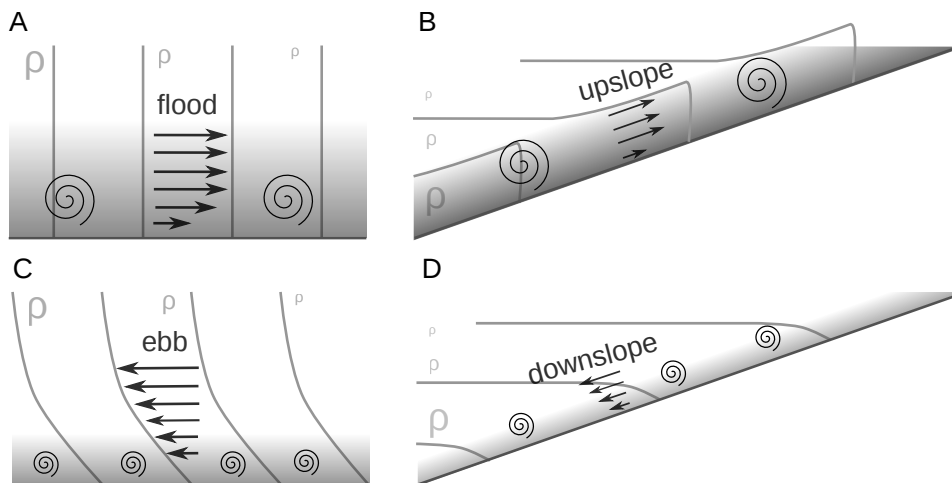


Figure 2.1.: Sketch of density structure during tidal straining (a,c) in an estuary or a region of fresh water influence, and (b,d) near sloping topography. Arrows show the instantaneous currents; suspended material is indicated by the gray-shaded areas near the bottom.

Jay and Musiak [1994] proposed that this tidal asymmetry in turbulent mixing may have a profound impact on the tidally averaged momentum budget. They pointed out that the stronger vertical homogenization of momentum during the more turbulent flood phase leads to a residual current that augments the gravitationally-driven residual circulation [see MacCready and Geyer 2010]. Exploring the physically relevant parameter space with a one-dimensional numerical model, Burchard and Hetland [2010] concluded that the residual circulation due to tidal straining typically dominates over the gravitational circulation in tidally energetic environments.

Whereas the residual circulation described above largely determines the horizontal transport of dissolved substances, additional effects have to be considered when modeling the residual transport of suspended particulate matter (SPM) with a sinking motion relative to the moving fluid. During the more turbulent flood phase (Fig. 2.1a), SPM concentrations are typically larger due to enhanced erosion, and suspended material is mixed up higher into the water column compared to the less turbulent ebb phase (Fig. 2.1c). The correlation between these asymmetries in concentration and the oscillating current results in a “tidal pumping” mechanism that induces a net landward transport of suspended material [Uncles et al. 1985; Jay and Musiak 1994; Scully and Friedrichs 2007]. Using a one-dimensional coupled sediment transport model, Burchard et al. [2013] showed that, for a broad range of parameters, tidal pumping is much more effective in transporting suspended material compared to advection by the residual current. This finding is in line with Scully and Friedrichs [2003], who pointed out that the transport due to tidal straining may even adverse the residual advective transport.

A related periodic straining process, not requiring any externally imposed horizontal density gradients, has recently been identified near the slopes of stratified lakes [Lorke et al. 2005]. In this case, a cross-slope (i.e., an approximately horizontal) density gradient is generated by the projection of the purely vertical interior stratification onto the sloping topography of the lateral boundaries of the basin (Fig. 2.1b,d). In the presence of oscillating up- and downslope currents, associated with basin-scale internal-wave motions in the case studied by Lorke et al. [2005], a shear-induced straining of the cross-slope density gradient is observed, analogous to classical tidal straining. During upslope flow, dense water is advected on top of lighter near-bottom water, leading to a reduction of vertical stratification, and ultimately to convection (Fig. 2.1b). Vice-versa, during periods of downslope flow, stable stratification evolves due to the downslope advection of lighter water on top of denser near-bottom fluid, resulting in a suppression of turbulent mixing (Fig. 2.1d). This effect has been observed in lakes of different size and geometry [Lorke et al. 2005, 2008; Cossu and Wells 2013], and could be reproduced in three-dimensional numerical modeling studies [Becherer and Umlauf 2011; Lorrai et al. 2011]. A recent study by Endoh et al. [2016] provided first direct observational evidence for the occurrence of slope-induced tidal straining on the continental shelf, and suggested that this process may also be important for the cross-slope transport of suspended material.

Umlauf and Burchard [2011] used an idealized one-dimensional numerical model to study the relevance of these findings for the oceanographically relevant parameter space. Their simulations revealed that shear-induced periodic stratification (SIPS) in sloping BBLs is expected to occur for virtually any parameter constellation, and triggers a residual circulation that is in many respects similar to classical tidal straining. The transport of suspended material was, however, not investigated in this study.

In view of these similarities, and relevance of classical tidal straining for the transport of suspended material in estuaries and the coastal ocean, it would be interesting to understand under which conditions and by which mechanisms tidal straining near sloping topography may be able to transport suspended material across isobaths. Here, we investigate this question with the help of a combined theoretical and idealized modeling approach, focusing on the identification of the basic mechanisms that determine cross-isobath transport of suspended material. The model, described in detail in Section 2.2, builds up on the model by Umlauf and Burchard [2011], extended here by adding a simple erosion and transport model for suspended material. In Section 2.3, we investigate the basic SPM transport mechanisms due to tidal straining near sloping topography with the help of a few idealized examples. The relevant (non-dimensional) parameters are identified in Section 2.4, and the parameter space is then explored in Section 2.5 before we draw some conclusions in Section 2.6.

2.2. Geometry and governing equations

2.2.1. Geometry

We investigate the motion of a Boussinesq fluid in a semi-infinite domain bounded by a uniform slope with slope angle α (Fig. 2.2). For simplicity, we ignore the effects of rotation, and assume that the geometry is two-dimensional with the horizontal and vertical coordinates referred to as \hat{x} and \hat{z} , respectively. Vertical stratification is quantified with the help of the squared buoyancy frequency,

$$N^2 = \frac{\partial b}{\partial \hat{z}}, \quad (2.1)$$

where b denotes the buoyancy of the fluid (all quantities are Reynolds-averaged unless noted otherwise). Outside the BBL, we assume that b approaches the undisturbed

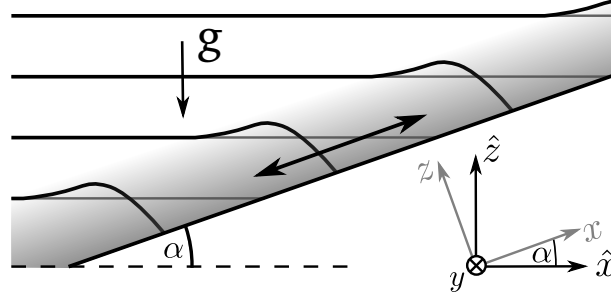


Figure 2.2.: Schematic view of isopycnal structure (black lines) in the vicinity of a uniform plane slope with slope angle α . Suspended material is indicated by the gray-shaded region near the bottom. The double arrow indicates the oscillatory current up and down the slope, the gray lines show the equilibrium levels of the isopycnals. The upslope and slope-normal coordinates are denoted by x and z , respectively.

equilibrium buoyancy b_∞ , which is characterized here by strictly horizontal isopycnals (gray lines in Fig. 2.2) and constant stratification:

$$N_\infty^2 = \frac{\partial b_\infty}{\partial \hat{z}} \quad . \quad (2.2)$$

It should be noted that, although N_∞ is constant by definition, b_∞ may vary in space and time due to up- and down-slope advection as discussed in more detail below.

Umlauf and Burchard [2011] showed that this two-dimensional problem can be reduced to one dimension by introducing the rotated upslope and slope-normal coordinates x and z ($z = 0$ at the bottom), and assuming that all upslope gradients except the buoyancy gradient vanish (see Fig. 2.2). Under these conditions, it is easy to show that the upslope buoyancy gradient is constant, and given by

$$\frac{\partial b}{\partial x} = N_\infty^2 \sin \alpha \quad . \quad (2.3)$$

The slope-normal buoyancy gradient is defined as

$$\check{N}^2 = \frac{\partial b}{\partial z} \quad , \quad (2.4)$$

which does not depend on x , and converges to

$$\check{N}^2 = N_\infty^2 \cos \alpha \quad \text{for } z \rightarrow \infty \quad , \quad (2.5)$$

far away from the bottom and thus outside the BBL.

2.2.2. Equations of motion

Starting from the Reynolds-averaged Boussinesq equations, Umlauf and Burchard [2011] showed that under the above assumptions, the equations of motion can be expressed as

$$\begin{aligned}\frac{\partial u}{\partial t} &= (b - b_\infty) \sin \alpha + \frac{\partial u_\infty}{\partial t} - \frac{\partial \tau}{\partial z}, \\ \frac{\partial b}{\partial t} &= -u N_\infty^2 \sin \alpha - \frac{\partial G}{\partial z},\end{aligned}\tag{2.6}$$

where t denotes time, u the cross-slope velocity, τ the slope-normal turbulent flux of momentum (normalized by some reference density ρ_0), and G the slope-normal turbulent buoyancy flux. The latter two are defined as

$$\begin{aligned}\tau &= \overline{u'w'} = -\nu_t \frac{\partial u}{\partial z}, \\ G &= \overline{w'b'} = -\nu_t^b \frac{\partial b}{\partial z},\end{aligned}\tag{2.7}$$

where the primes indicate turbulent fluctuations, and the overbar the Reynolds average (w is the slope-normal velocity). The turbulent diffusivities of momentum and buoyancy, ν_t and ν_t^b , are computed from a second-moment turbulence closure model with two transport equations for the turbulent kinetic energy k and the turbulence dissipation rate ε [see Umlauf and Burchard 2005]. We assume high Reynolds numbers, and therefore ignore the molecular fluxes of momentum and buoyancy in (2.6). The turbulence model and all model parameters are identical to the model used in Umlauf and Burchard [2011] and Umlauf et al. [2015], where a more detailed model description may be found.

The term $\partial u_\infty / \partial t$ appearing in (2.6) is an integration constant that, in general, depends on time, and plays the role of a prescribed external pressure gradient used to force the model. Internal pressure gradients are represented by the term $(b - b_\infty) \sin \alpha$, which mirrors the tendency of isopycnals to relax back towards their equilibrium levels (see Fig. 2.2). The equilibrium buoyancy b_∞ is computed from an evolution equation

of the form

$$\frac{\partial b_\infty}{\partial t} + u_\infty N_\infty^2 \sin \alpha = 0 , \quad (2.8)$$

which represents the up- or downslope advection of the undisturbed buoyancy field [Umlauf and Burchard 2011].

At the lower boundary, we use a no-slip condition for the velocity, and assume that the buoyancy flux vanishes:

$$\begin{aligned} u &= 0 , \\ \frac{\partial b}{\partial z} &= 0 . \end{aligned} \quad (2.9)$$

Boundary conditions for the turbulence quantities are discussed in Umlauf and Burchard [2011], who assumed that the bottom is hydrodynamically rough (which introduces the bottom roughness z_0 as an additional external parameter), and that a logarithmic wall-layer exists very close to the bottom. Far away from the lower boundary ($z \rightarrow \infty$), boundary conditions are derived from the assumptions that u and N are uniform, and that all turbulent fluxes vanish.

Assuming that there are no hydrodynamic feedbacks resulting from the suspended material, equations (2.6) and (2.8) fully describe the evolution of the unknowns u , b , and b_∞ . This system of equations has been numerically solved for different parameters, using a time step and grid size small enough to exclude any significant numerical errors. Mathematical and numerical implementation details are described in Umlauf et al. [2005].

2.2.3. Boundary-layer forcing and resonance

We restrict our analysis to the special case of an oscillatory outer flow,

$$u_\infty = U \sin \omega t , \quad (2.10)$$

where U is the fixed velocity amplitude, $\omega = 2\pi/T_f$ the forcing frequency, and T_f the forcing period. Here, we focus exclusively on motions at the M_2 tidal frequency ($T_f =$

12.4 h) such that u_∞ provides a simple representation of the near-bottom currents induced by barotropic or baroclinic tides.

Umlauf and Burchard [2011] showed that BBL motions relative to the interior contain both kinetic and potential energy, which suggests the possibility of reversible BBL oscillations. It can be shown that these oscillations occur at the frequency

$$\omega_c = N_\infty \sin \alpha , \quad (2.11)$$

which happens to coincide with the frequency for the critical reflection of internal waves impinging on a slope with slope angle α [see Thorpe 2005]. Close to resonant forcing ($\omega \approx \omega_c$), it is therefore likely that the geometric assumptions outlined above break down, and the model can no longer be applied [Umlauf and Burchard 2011]. We therefore exclude this parameter range from the following analysis, and only consider the cases $\omega \gg \omega_c$ (strongly supercritical forcing) and $\omega \ll \omega_c$ (strongly subcritical forcing). Note that for given forcing frequency ω , (2.11) may be inverted to compute the critical slope angle, α_c . Evidently, supercritical forcing corresponds to subcritical slopes, and vice-versa.

2.2.4. Erosion and transport of suspended material

Focusing on the basic physical mechanisms determining the transport of suspended material near sloping topography, we use a relatively simple erosion and transport model. Suspended material is assumed to sink vertically down with a constant settling velocity w_s but is otherwise considered to behave like a passive tracer (no hydrodynamical feedbacks). Processes like aggregation or disintegration of suspended particles are ignored. The evolution equation for the concentration c of suspended material is thus of the form

$$\frac{\partial c}{\partial t} = -\frac{\partial}{\partial z} (F_z - cw_s \cos \alpha) , \quad (2.12)$$

where the slope-normal turbulent sediment flux is defined as

$$F_z = -\nu_t^b \frac{\partial c}{\partial z} . \quad (2.13)$$

Clearly, the cross-slope advection term $\partial(uc)/\partial x$ does not appear in (2.12) due to the assumed cross-slope homogeneity in our geometry. This assumption is formally valid

only if the length-scale L_c of cross-slope variations in SPM concentration is much larger than the tidal excursion scale: $L_c \gg U/T_f$. The concentration of suspended material, however, may vary on smaller scales in many situations, which should be kept in mind when interpreting the results from this study.

At the lower boundary, the turbulent SPM flux F_z in (2.13) equals the erosion flux, here determined from the classical expression

$$F_z = \alpha_e \max \left\{ \frac{|\tau_b|}{\tau_c} - 1, 0 \right\} \quad \text{for } z = 0, \quad (2.14)$$

where α_e is the erosion coefficient, τ_b the bottom shear stress, and τ_c the critical shear stress for resuspension, both normalized by the constant reference density ρ_0 [see Krone 1962; Sanford and Chang 1997; Amoudry and Souza 2011]. The availability of erodible material is assumed to be unlimited in this idealized study.

Note that, in general, the SPM parameters appearing in (2.12) and (2.14) are not independent. E.g., for the relatively simple case of non-cohesive material, van Rijn [1984b] suggests a relation between w_s , τ_c , and the grain size. The situation becomes, however, considerably more complex if unsorted or non-cohesive material is considered [e.g., Dade et al. 1992; Sassi et al. 2015], or if biological activity (bioturbation, biofilms) play a significant role [Grant et al. 1986; Grant and Daborn 1994]. Because a generally valid relation is not available at the moment, we consider w_s , τ_c , and α_e as independent parameters in our study. The physically relevant range for these parameters is explored in detail in Section 2.5.

2.2.5. Residual transports

In order to quantify the tidally-averaged transport of SPM, we define the total cross-slope residual flux,

$$F_x = \langle uc \rangle - \langle c \rangle w_s \sin \alpha, \quad (2.15)$$

where the angular brackets denote the tidal average. The last term in (2.15) is recognized as the projection of the vertical sinking velocity onto the downslope direction. For the small slope angles considered here, however, this “sinking flux” is negligible, and will therefore be ignored in the following.

Following Burchard et al. [2013], we further decompose the residual flux into contributions from the residual current and the tidal fluctuations:

$$\langle uc \rangle = \langle u \rangle \langle c \rangle + \langle \tilde{u}\tilde{c} \rangle , \quad (2.16)$$

where the tilde indicates deviations from the tidal average. The first term on the right hand side in (2.16) represents the contribution of the residual current to the total residual flux, whereas the second term, referred to as the “tidal pumping” term in the following, mirrors the effect of tidal straining. Dividing (2.16) by the average concentration $\langle c \rangle$, we find an expression of the form

$$u_c = \langle u \rangle + \frac{\langle \tilde{u}\tilde{c} \rangle}{\langle c \rangle} , \quad (2.17)$$

which may be interpreted as the effective velocity at which suspended material is transported across the slope. Note from (2.17) that the transport velocity u_c may be significantly different from the residual velocity $\langle u \rangle$ (both may even have opposite sign) if tidal pumping is important.

2.3. Boundary-layer dynamics and sediment transport

As an example to illustrate the basic processes, we consider in the following a case with a relatively mild slope ($\alpha = 0.002$), a typical tidal velocity amplitude ($U = 0.5 \text{ m s}^{-1}$), and some other typical parameters summarized in Tab. 2.1 (Case 1).

According to (2.11), in this example the resonance period of the BBL is $T_c = 2\pi\omega_c^{-1} \approx 87 \text{ h}$ and the critical slope $\alpha_c \approx 0.014$, indicating that tidal forcing is strongly supercritical. Correspondingly, the slope is strongly subcritical. All results discussed here and in the following sections correspond to fully periodic conditions.

2.3.1. Boundary-layer dynamics

As the sediment model has no feedback on the hydrodynamic part of the problem, the evolution of the near-bottom velocities, stratification, and mixing parameters is qualitatively similar to that discussed in Umlauf and Burchard [2011]. Here, we only briefly

Table 2.1.: Parameters used for the simulation discussed in section 2.3. Note that supercritical forcing corresponds to subcritical slopes, and vice-versa.

case	forcing	U	ω	z_0	α_e
1	supercritical	0.5 m s^{-1}	$1.41 \times 10^{-4} \text{ s}^{-1}$	10^{-2} m	$10^{-4} \text{ kg s}^{-1} \text{ m}^{-2}$
2	subcritical	0.5 m s^{-1}	$1.41 \times 10^{-4} \text{ s}^{-1}$	10^{-2} m	$10^{-4} \text{ kg s}^{-1} \text{ m}^{-2}$
3	subcritical	0.5 m s^{-1}	$1.41 \times 10^{-4} \text{ s}^{-1}$	10^{-2} m	$10^{-4} \text{ kg s}^{-1} \text{ m}^{-2}$

case	forcing	τ_c	w_s	N_∞^2	α
1	supercritical	$10^{-4} \text{ m}^2 \text{ s}^{-2}$	$5 \times 10^{-3} \text{ m s}^{-1}$	10^{-4} s^{-2}	2×10^{-3}
2	subcritical	$10^{-4} \text{ m}^2 \text{ s}^{-2}$	$2 \times 10^{-4} \text{ m s}^{-1}$	10^{-3} s^{-2}	5×10^{-2}
3	subcritical	$10^{-4} \text{ m}^2 \text{ s}^{-2}$	$9 \times 10^{-4} \text{ m s}^{-1}$	10^{-3} s^{-2}	5×10^{-2}

summarize the main hydrodynamical characteristics of this type of flow to provide the context for the following discussion of resuspension and residual SPM transports.

Fig. 2.3a,b shows that, for the parameters compiled in Tab. 2.1, the oscillating tidal currents generate a BBL of approximately 40 m thickness, characterized by strongly reduced stratification below a sharp pycnocline that separates the BBL from the non-turbulent interior region. During periods of upslope flow, a large fraction of the BBL becomes gravitationally unstable (light gray lines in Fig. 2.3), whereas during downslope flow it remains stably stratified throughout. Umlauf and Burchard [2011] showed that the periodic destabilization of the BBL can be explained by a differential advection mechanism resulting from the interaction of the frictional near-bottom shear and the constant upslope density gradient, analogous to tidal straining. More specifically, they showed that during upslope flow, dense fluid may be transported on top of the lighter, more slowly moving fluid in the immediate vicinity of the bottom, resulting in unstable stratification, and thus turbulent convection. It is worth noting that Endoh et al. [2016] reported recent observations of this processes for a tidal BBL of similar vertical scale on a sloping continental shelf.

The periodic changes in stratification visible in Fig. 2.3b are directly mirrored in the turbulent diffusivities shown in Fig. 2.3c. During periods of upslope flow, when weak or unstable stratification develops, diffusivities are strongly enhanced compared to the stratified period with downslope flow. This variability in ν_t^b caused by tidal straining induces a tidal asymmetry that is, besides gravitational forcing, the key trigger for residual cross-slope transports inside the BBL.

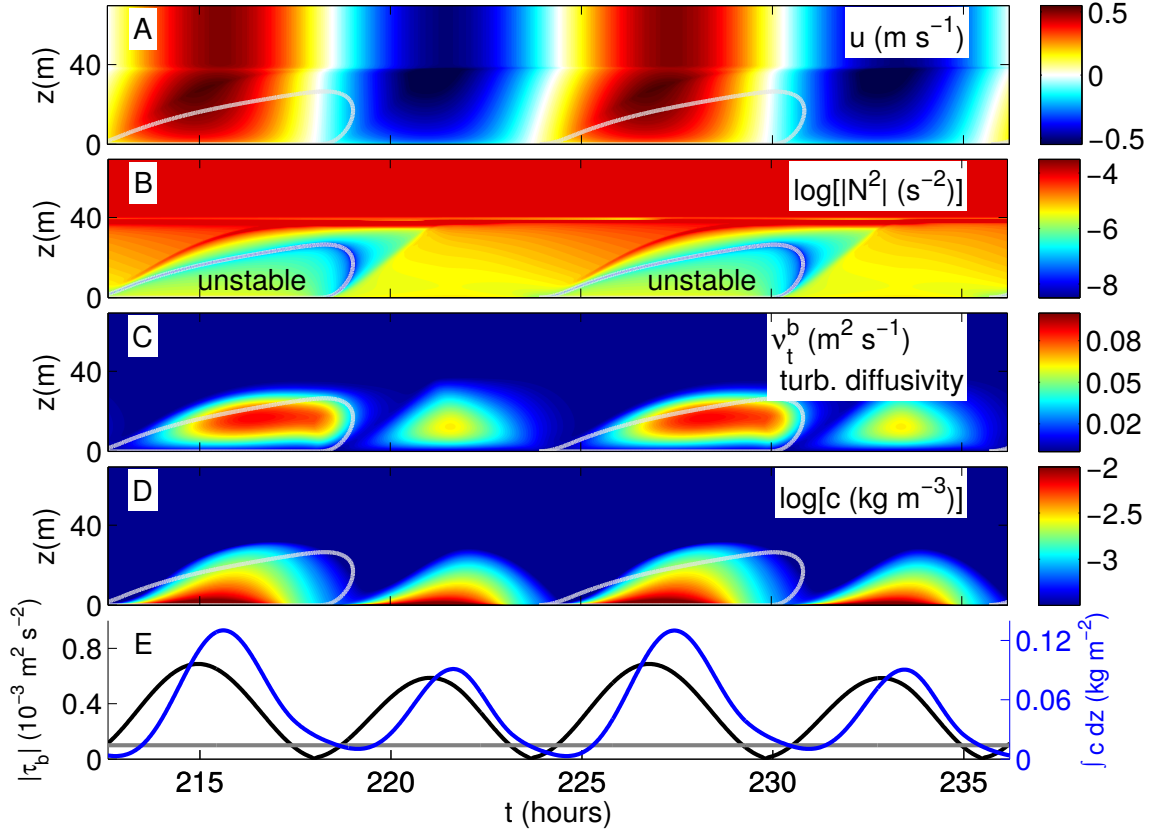


Figure 2.3.: Temporal variability of (a) velocity, (b) magnitude of the squared buoyancy frequency, (c) turbulent diffusivity, (d) SPM concentration, and (e) magnitude of the bottom shear stress (black), critical shear stress for re-suspension (gray), and integrated sediment concentration (blue). Gray lines in panels (a)–(d) indicate gravitationally unstable regions. All results represent fully periodic conditions (time refers to the start of the simulation). Parameters correspond to Case 1 in Tab. 2.1.

SPM properties shown in Fig. 2.3d,e are consistent with these tidal asymmetries in mixing. During periods of upslope flow, a larger amount of material is resuspended (Fig. 2.3e), SPM is mixed up higher into the water column, and SPM concentrations are somewhat larger compared to periods with downslope flow (Fig. 2.3d). These asymmetries can be interpreted as a consequence of the larger turbulent diffusivities during upslope flow, and the larger bottom shear stress, which, according to (2.14) determines the resuspension of settled material.

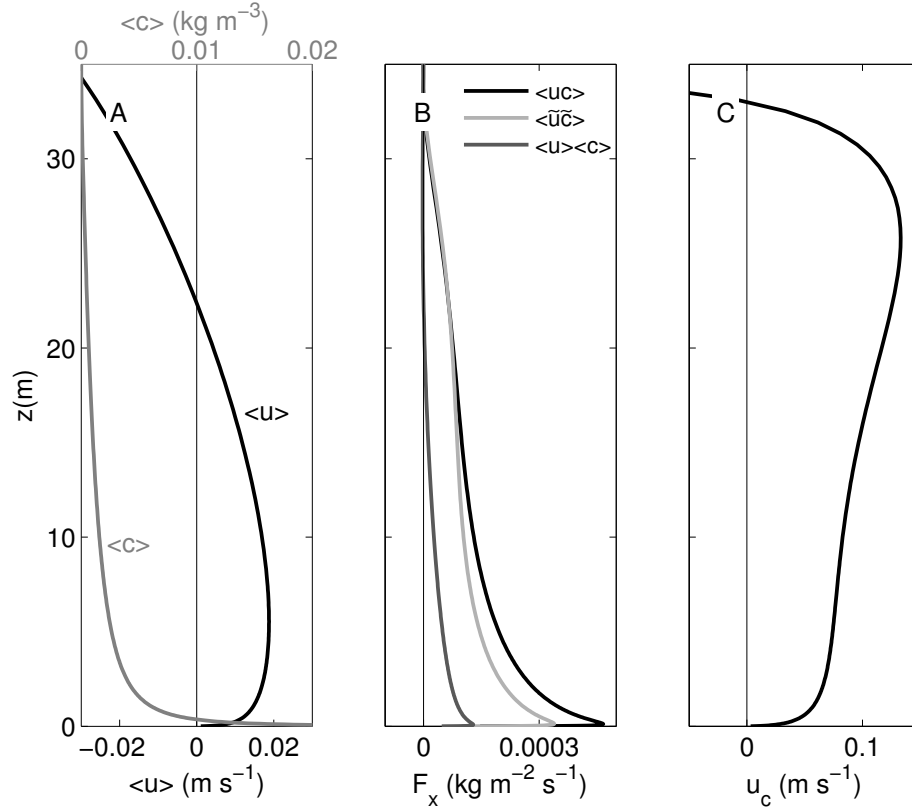


Figure 2.4.: Vertical profiles of (a) residual current (black) and tidally-averaged SPM concentration (gray), (b) cross-slope residual flux, decomposed into contributions from the residual current and tidal pumping, and (c) effective cross-slope transport velocity computed from (2.17). Note that for clarity only the lower part of the domain is displayed. Parameters correspond to Case 1 in Tab. 2.1.

2.3.2. Residual results

Fig. 2.4 shows some tidally-averaged key parameters like the residual velocity, the SPM concentration, and the cross-slope flux of SPM, based on the simulation shown in Fig. 2.3. The residual currents are of the order of 0.01 m s^{-1} , directed upslope near the bottom and downslope in the upper part of the BBL (Fig. 2.4a). In this context, it should be noted that, for fully periodic conditions and negligible mixing outside the BBL, it can be mathematically shown that the total cross-slope transport vanishes for the geometry investigated here [Umlauf and Burchard 2011]:

$$\int_0^{\infty} \langle u \rangle dz = 0 \quad . \quad (2.18)$$

This implies that the upslope residual current near the bottom is exactly compensated by the negative (downslope) residual flow in the upper part of the BBL.

The tidally-averaged SPM concentration (gray line in Fig. 2.4a) shows a strong increase towards the bottom, as expected from the classical Rouse-type balance between sinking and upward turbulent transport of suspended material. Fig. 2.4b shows that the residual upslope current in the lower part of the BBL leads to a weak upslope advection of suspended material. This transport, however, is negligible in the upper part of the BBL ($z > 20$ m), and several times smaller than the contribution from tidal pumping in the lower part. This is also mirrored in the effective SPM transport velocity defined in (2.17), which is several times larger than the residual current (see Fig. 2.4c). Similar to classical tidal straining, therefore, we find that tidal pumping is crucial for the total residual transport of suspended material.

The physical mechanisms inducing tidal pumping in this example are easily identified from Fig. 2.3. As discussed above, sediment concentrations during upslope flow are larger than during downslope flow due to enhanced erosion and stronger upward mixing of suspended material. This leads to a positive correlation between \tilde{u} and \tilde{c} , and thus to a residual upslope transport of suspended material. The magnitude of the transport velocity ($u_c \sim 0.1$ m s⁻¹) suggests that suspended material is transported several kilometers upslope during a single tidal cycle in this example. This supports our main hypothesis that tidal straining in the BBL near sloping topography constitutes an effective mechanism for the transport of suspended material across isobaths.

To investigate how this process is affected by the properties of the suspended material, we compare in Fig. 2.5 the effects of different sinking speeds and critical shear stresses, leaving all other parameters unchanged (see Case 1 in Tab. 2.1). For the lowest sinking speed ($w_s = 10^{-4}$ m s⁻¹), shown in Fig. 2.5a, downward sinking of suspended material cannot compete with upward mixing, and SPM concentrations inside the BBL therefore fluctuate only marginally around the tidal average ($\tilde{c}/\langle c \rangle \ll 1$), except in the upper few meters of the BBL (not shown). In this case, tidal pumping is not effective ($\langle \tilde{u}\tilde{c} \rangle \ll \langle u \rangle \langle c \rangle$), and transports are largely determined by the two-layer structure of the residual current shown in Fig. 2.4a.

This situation is contrasted by the case with the highest sinking speeds ($w_s = 10^{-2}$ m s⁻¹), displayed in Fig. 2.5c, which is physically similar to the classical tidal pumping mechanism described already in the context of Fig. 2.4b above: higher SPM concentrations during the less stratified and more turbulent upslope flow phase result in a residual upslope transport of suspended material. Due to the higher sinking velocity compared to Fig. 2.4b, however, the pumping process is now confined to the lowest

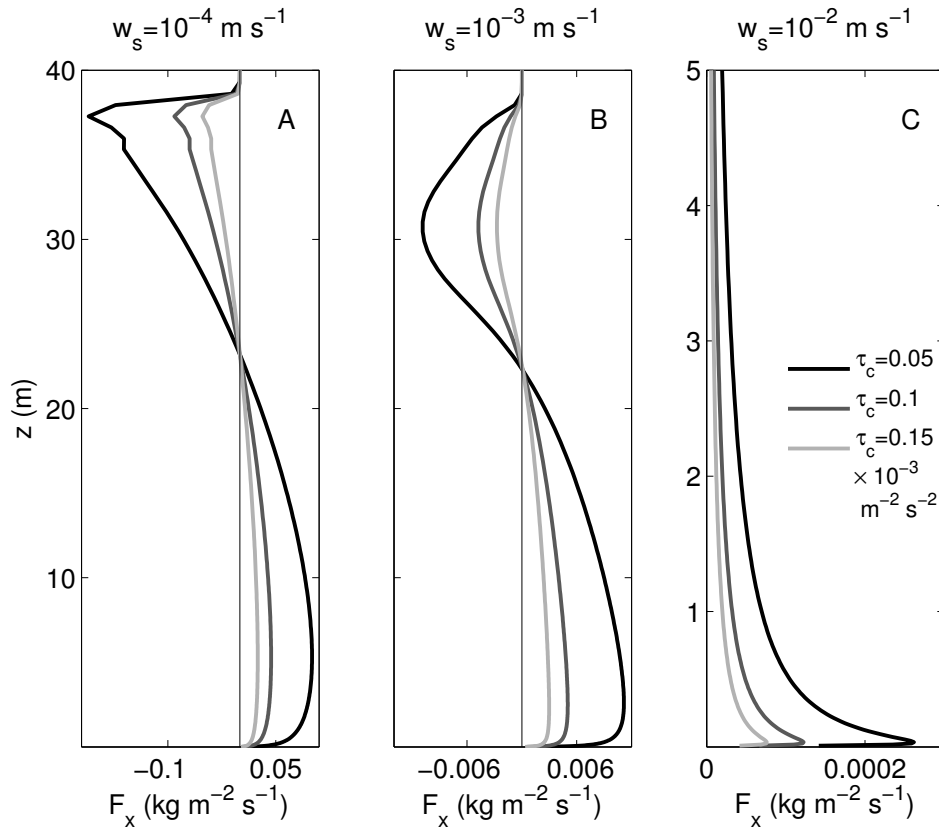


Figure 2.5.: Vertical profiles of residual SPM transports for different critical shear stresses (as indicated) and settling velocities: (a) $w_s = 10^{-4} \text{ m s}^{-1}$, (b) $w_s = 10^{-3} \text{ m s}^{-1}$, and (c) $w_s = 10^{-2} \text{ m s}^{-1}$. All other parameters correspond to Case 1 in Tab. 2.1.

few meters of the water column as shown in Fig. 2.5c (note the different vertical scale in this panel).

Physically most interesting is the intermediate case shown in Fig. 2.5b, corresponding to a sinking velocity of $w_s = 10^{-3} \text{ m s}^{-1}$. Although the vertical structure of the profile suggests a similarity with the well-mixed case in Fig. 2.5a, the underlying processes are entirely different. Here, the upslope transport of SPM in the lower part of the BBL (see Fig. 2.5b) is driven by classical tidal pumping, analogous to the cases with higher sinking velocities shown in Figs. 2.4b and 2.5c. The downslope transport observed in the upper part of the BBL, however, is triggered by a modified (inverse) pumping mechanism resulting from a phase shift in the SPM concentrations. This is most easily understood from Fig. 2.3b, showing that the well-mixed near-bottom layer reaches its maximum thickness not before the point of flow reversal. Because newly eroded material is confined to this turbulent near-bottom layer, maximum SPM concentrations in the upper part of the BBL are observed with a substantial delay compared to the near-

bottom region (not shown). This phase shift results in a positive correlation between periods of downslope flow and high SPM concentrations, and therefore in a residual downslope transport of suspended material in the upper part of the BBL.

The role of the critical shear stress is investigated in Fig. 2.5, where again all other parameters correspond to Case 1 in Tab. 2.1. According to (2.14), a lower critical shear stress leads to a larger erosion flux, and thus, for otherwise unchanged parameters, to a larger SPM concentration in the water column. Fig. 2.5 reveals that the net effect is an increase of the residual SPM fluxes without, however, affecting the basic mechanisms described above. Similar effects are observed if the bottom roughness is changed (Fig. 2.6).

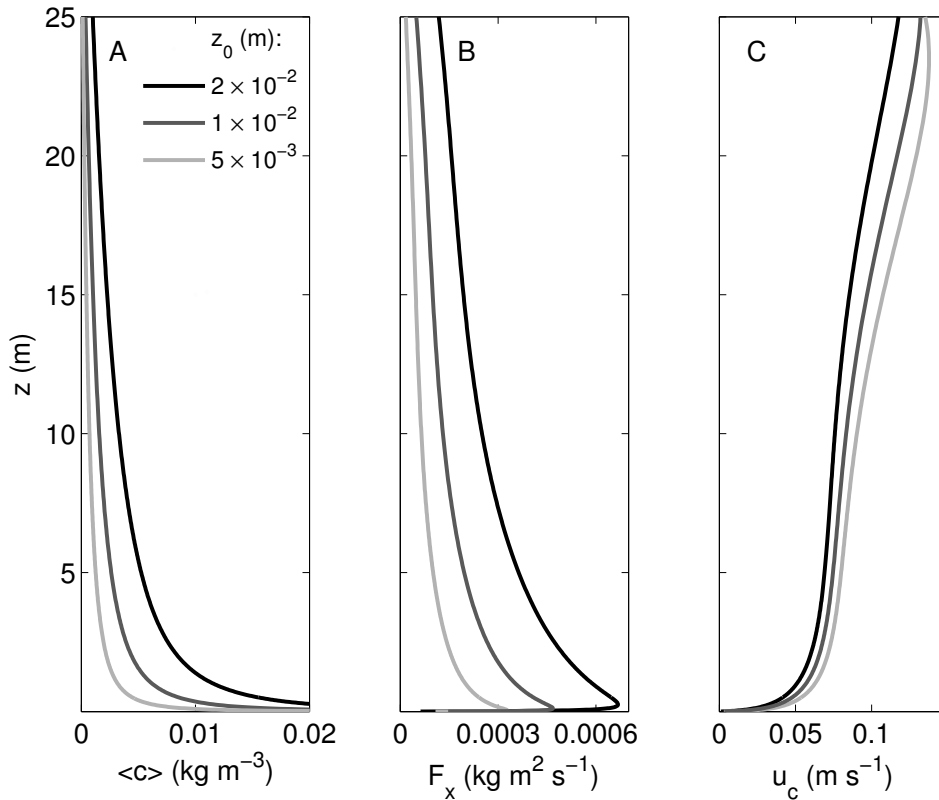


Figure 2.6.: Profiles of (a) tidally-averaged SPM concentration, (b) residual SPM transport, and (c) effective transport velocity for different bottom roughnesses (as indicated). All other parameters correspond to Case 1 in Tab. 2.1. Note that, for clarity, only the lower part of the domain is displayed.

Reducing or increasing the bottom roughness by a factor of 2 with respect to the reference case (Case 1 in Tab. 2.1), results in significant changes in the bottom stress, and, therefore, in a modified erosion flux. This results in strongly altered SPM con-

centrations and transport rates (Fig. 2.6a,b) but only in small modifications of the dynamics. The BBL thickness varies by less than 10% (not shown), and the transport velocity by less than 15% compared to the reference Case 1 (Fig. 2.6c). Keeping these basic effects of variations in τ_c and z_0 in mind, we will therefore not investigate the impact of these parameters in further detail in the following.

2.3.3. Supercritical slopes

The parameters for our second example, used to illustrate the basic transport mechanisms for subcritical forcing (i.e., supercritical slopes), are compiled in Tab. 2.1 (Cases 2 and 3). The BBL resonance period in this case is $T_c \approx 1.1$ h, indicating that tidal forcing is strongly subcritical. Correspondingly, the slope angle $\alpha = 0.05$ is more than a factor 10 larger than the critical slope angle $\alpha_c = 0.0045$.

Despite these differences in forcing, however, the observed flow patterns exhibit many similarities with Case 1 (subcritical slope) discussed above. During upslope flow, a gravitationally unstable, vigorously turbulent near-bottom layer evolves, whereas during downslope flow, turbulence is suppressed by the generation of stable stratification (Fig. 2.7a,b).

Different from Case 1, high-frequency oscillations at the BBL resonance period T_c can now be distinguished in the cross-slope velocities (Fig. 2.7a), however, without significantly modifying the overall dynamics. More important for the following discussion is the observation that, due to the stronger tendency for re-stratification, tidal asymmetries in the turbulent diffusivity and the BBL thickness are much more pronounced compared to the case with subcritical slope (Fig. 2.7b). E.g., the maximum thickness of the turbulent BBL varies between $h^{\text{up}} = 10$ m during upslope flow, and $h^{\text{down}} = 3$ m during downslope flow.

Fig. 2.7c,d, showing SPM concentrations for two different sinking speeds, reveals that this asymmetry in BBL thickness strongly impacts on the vertical SPM distribution. During upslope flow, SPM is mixed up higher into the water column, whereas during downslope flow, most of the suspended material is trapped in the much thinner turbulent BBL, resulting in extremely high near-bottom SPM concentrations. After the maximum BBL thickness h^{up} during upslope flow has been reached, the turbulent BBL collapses quickly during the restratification process (Fig. 2.7b). Particles mixed up during the strongly turbulent upslope flow phase may therefore remain suspended in

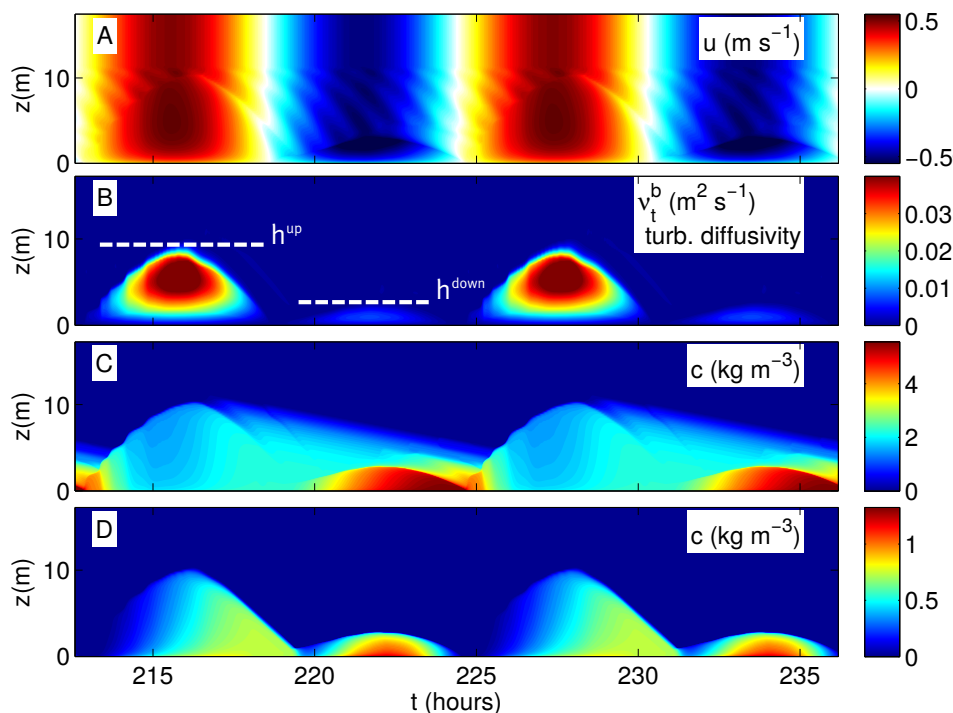


Figure 2.7.: Temporal variability of (a) velocity, (b) turbulent diffusivity, (c) SPM concentration for Case 2, and (d) SPM concentration for Case 3. All results represent fully periodic conditions (time refers to the start of the simulation). All parameters as in Tab. 2.1.

the non-turbulent region above the BBL if their sinking speed is small. Fig. 2.7c shows that this effects leads to non-zero SPM concentrations above the BBL even after the reversal to downslope flow. Quickly sinking particles, on the other hand, will always be confined to the turbulent BBL (Fig. 2.7d).

These extreme tidal asymmetries have a strong impact on the residual SPM fluxes as illustrated in Fig. 2.8. Both the near-bottom residual circulation (Fig. 2.8a) and the residual SPM flux (Fig. 2.8b) suggest a downslope transport of suspended material in the near-bottom region, which is exactly opposite to the case with subcritical slope shown in Fig. 2.4. The reversal of the residual SPM flux close to the bottom ($z < h^{\text{down}}$) is easily understood from Fig. 2.7c,d, showing that near-bottom SPM concentrations are much higher during phases of downslope flow compared to upslope flow. The net effect is a downslope tidal pumping of suspended material. The reversal of the near-bottom residual circulation for super-critical slopes, also evident from Fig. 2.8a, was already noted by Umlauf and Burchard [2011], who showed mathematically that this phenomenon occurs if convective mixing (unstable stratification) during upslope flow

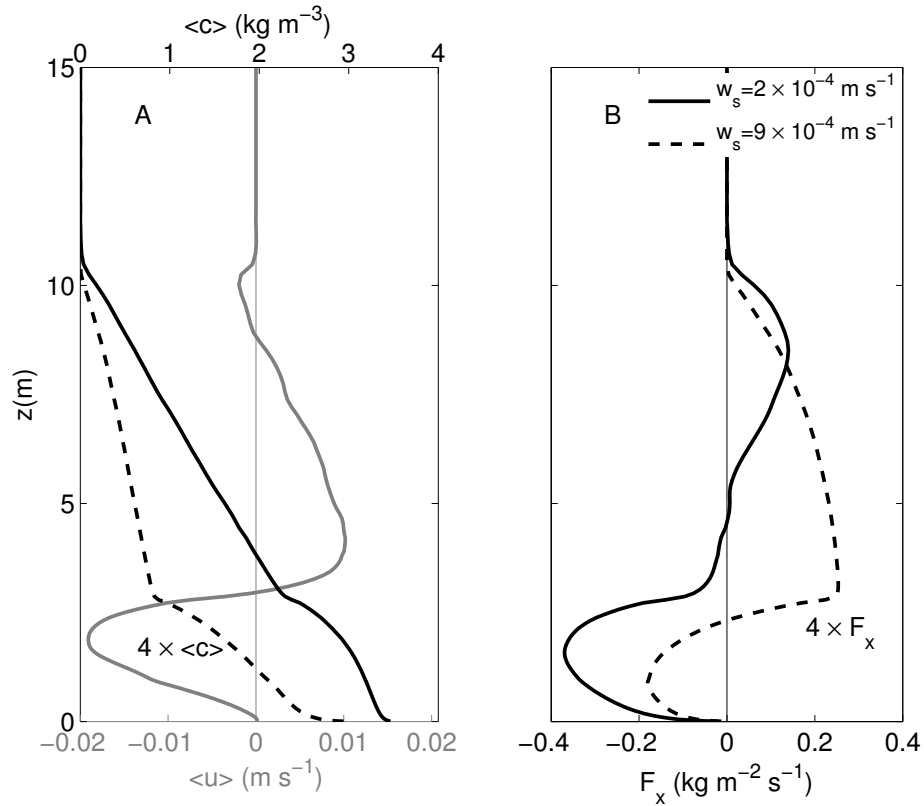


Figure 2.8.: Vertical profiles of (a) residual velocity and tidally averaged sediment concentration, and (b) residual upslope transport for two different sinking speeds as indicated. For better visibility, results for the higher sinking speed ($w_s = 9 \times 10^{-4}$ m s⁻¹) were multiplied by a factor of 4. Parameters correspond to Cases 2 and 3 in Tab. 2.1.

dominates tidally-averaged near-bottom mixing. Similar to the previous examples for subcritical slopes, however, the contribution of the residual current to the total residual SPM flux is small compared to the effect of tidal pumping.

The processes in the upper part of the BBL ($z > h^{\text{down}}$) are more similar to classical tidal pumping. Here, SPM concentrations are larger during periods of upslope flow, when strong turbulence results in enhanced resuspension and upward mixing of suspended material (Fig. 2.7c,d). While many aspects of this process resemble the situation for subcritical slopes shown in Fig. 2.3, there is one important difference. For quickly sinking material, the concentration of suspended material is zero during the downslope flow phase for $z > h^{\text{down}}$ (Fig. 2.7d), resulting in tidal pumping with maximum efficiency in this region.

The strength and even the direction of the vertically integrated residual transport are determined by the relative importance of downslope tidal pumping in the near-bottom region, and upslope tidal pumping in the region above. The crucial parameter that determines this interplay is the sinking velocity, as discussed in more detail below.

2.4. Non-dimensional description

To investigate the physically relevant parameter space in a systematic way, it is useful to identify the key non-dimensional parameters that determine the solutions of the equations described in Section 2.2. To this end, we first note that there are eight dimensional parameters appearing in the equations and boundary conditions described above. They may be grouped into parameters related to the properties of the slope (α and z_0), the interior flow (U , ω , and N_∞), and the suspended material (α_e , τ_c , and w_s). These dimensional parameters can be combined into five non-dimensional products, with one possible choice being:

$$\alpha, \quad Z = \frac{N_\infty}{\omega}, \quad R = \frac{z_0\omega}{U}, \quad P = \frac{w_s}{U}, \quad T = \frac{\tau_c}{U^2}, \quad (2.19)$$

where Z is a frequency ratio, R a non-dimensional measure of the bottom roughness, P a special form of the Rouse number, and T the non-dimensional critical shear stress. Note that for dimensional reasons, the erosion parameter α_e does not appear in this or any other set of non-dimensional products (it is the only parameter involving the dimension of a mass).

2.4.1. Non-dimensional equations

In order to understand how these non-dimensional numbers appear in the governing equations, we start by defining non-dimensional versions of the time and the slope-normal coordinate:

$$t^* = t\omega, \quad z^* = \frac{z\omega}{U}. \quad (2.20)$$

The dimensional variables appearing in the transport equations in (2.6) and (2.12) are then non-dimensionalized according to:

$$u^* = \frac{u}{U}, \quad b^* = \frac{b}{UN_\infty}, \quad \tau^* = \frac{\tau}{U^2}, \quad G^* = \frac{G}{U^2N_\infty}, \quad c^* = \frac{cU}{\alpha_e}, \quad F_z^* = \frac{F_z}{\alpha_e}. \quad (2.21)$$

This yields the following non-dimensional equations:

$$\begin{aligned} \frac{\partial u^*}{\partial t^*} &= Z\alpha(b^* - b_\infty^*) + \cos t^* - \frac{\partial \tau^*}{\partial z^*}, \\ \frac{\partial b^*}{\partial t^*} &= -Z\alpha u^* - \frac{\partial G^*}{\partial z^*}, \\ \frac{\partial c^*}{\partial t^*} &= -\frac{\partial}{\partial z^*} (F_z^* - Pc^*), \end{aligned} \quad (2.22)$$

where we used the special form of the tidal forcing term in (2.10), and assumed mild slopes ($\alpha \ll 1$). It should be noted that the variables in (2.21), although non-dimensional, are not scaled, i.e. terms appearing in (2.22) are generally not of order 1.

Only three of the five non-dimensional parameters compiled in (2.19) are seen to appear in (2.22). Non-dimensional boundary conditions, derived from (2.9) and (2.14), are of the form

$$u^* = 0, \quad \frac{\partial b^*}{\partial z^*} = 0, \quad F_z^* = \max \left\{ \frac{|\tau_b^*|}{T} - 1, 0 \right\} \quad \text{for } z^* = 0, \quad (2.23)$$

which reveals that the fourth non-dimensional parameter, the non-dimensional critical shear stress T , appears in the boundary condition of the erosion model. Umlauf and Burchard [2011] showed that parameter number five, the roughness number R , enters the problem via the lower boundary condition for the turbulence dissipation rate. These authors also pointed out that because the turbulence model does not involve any dimensional constants, no additional parameters enter the problem.

2.4.2. Non-dimensional fluxes

The total cross-slope transport of suspended material is easily quantified from the integral of the residual flux defined in (2.15):

$$F_{int} = \int_0^{\infty} F_x dz , \quad (2.24)$$

which can be re-expressed in non-dimensional form as

$$F_{int}^* = \frac{\omega}{\alpha_e U} F_{int} = \int_0^{\infty} F_x^* dz^* . \quad (2.25)$$

In order to derive a bulk expression for the effective velocity at which SPM is transported, it may seem tempting to work with the BBL average of (2.17). In view of the constraint in (2.18), however, this would eliminate the contribution from the residual current, which is small but generally not negligible. Also, it should be noted that, according to (2.17), we find $|u_c| \rightarrow \infty$ in regions where $\langle c \rangle \rightarrow 0$. Regions with the smallest SPM concentrations would therefore provide the largest contributions to the integral of u_c , which therefore cannot be considered as a sensible bulk measure for the transport velocity.

Here, we use the following alternative approach to define the bulk transport velocity:

$$U_c = \frac{\int_0^{\infty} F_x dz}{\int_0^{\infty} \langle c \rangle dz} , \quad (2.26)$$

which does not exhibit the above problems. The non-dimensional transport velocity is then defined as $U_c^* = U_c/U$. The quantities F_{int}^* and U_c^* will be central to the following analysis of cross-slope SPM transport in non-dimensional parameter space.

2.4.3. Parameter space

In the following, we investigate the variability of SPM transport across the physically relevant (non-dimensional) parameter space. All computations were carried out in dimensional space, and results were then made non-dimensional as described in the previous sections. Note that different simulations in dimensional space map onto identical non-dimensional solutions if they correspond to the same non-dimensional pa-

rameters. We used this fact to test the correctness of the mathematical and numerical implementation of our model.

Our simulations will be based on the numerical examples discussed in Section 2.3, now, however, allowing for a broader range of variations of the key non-dimensional parameters: the sinking speed P , the stratification parameter Z , and the slope angle α . For the non-dimensional sinking speed, we explored the parameter range $5 \times 10^{-4} \leq P < 5 \times 10^{-2}$ (sampled with 100 logarithmically spaced intervals), which represents a typical spectrum of sinking speeds in the ocean [e.g., Ferguson and Church 2004; Van Leussen 1988]. The stratification parameter Z is varied between $Z = 71$ and $Z = 224$, corresponding to one order of magnitude change in the vertical density gradient. Finally, the slope angle α was varied over the range $10^{-3} \leq \alpha < 10^{-1}$, which covers virtually all oceanographically relevant slopes. This range was resolved with 200 logarithmically spaced intervals to account for the large variability of the SPM fluxes in the vicinity of the critical slope angle (see below).

2.5. Non-dimensional simulations

In the following, we explore the non-dimensional parameter space defined above, focusing on the effects of variations in non-dimensional settling velocity, stratification, and slope angle. To this end, two groups of simulations with subcritical and supercritical forcing, respectively, were carried out based on the parameters summarized in Tab. 2.3 (Cases I and II). The non-dimensional parameters corresponding to Cases 1-3, discussed in the previous sections, are shown in Tab. 2.2 for reference.

Table 2.2.: Non-dimensional parameters corresponding to Cases 1-3 in Tab. 2.1. Note that supercritical forcing corresponds to subcritical slopes, and vice-versa.

case	forcing	α	Z	R	P	T
1	supercritical	2×10^{-3}	71	2.8×10^{-6}	10^{-2}	4×10^{-4}
2	subcritical	5×10^{-2}	224	2.8×10^{-6}	4×10^{-4}	4×10^{-4}
3	subcritical	5×10^{-2}	224	2.8×10^{-6}	2×10^{-3}	4×10^{-4}

Table 2.3.: Non-dimensional parameters for the simulations in Section 2.5. Note that supercritical forcing corresponds to subcritical slopes, and vice-versa.

case	forcing	α	R	P	T
I	supercritical	2×10^{-3}	2.8×10^{-6}	variable	4×10^{-4}
II	subcritical	5×10^{-2}	2.8×10^{-6}	variable	4×10^{-4}
III	variable	variable	2.8×10^{-6}	10^{-2}	4×10^{-4}

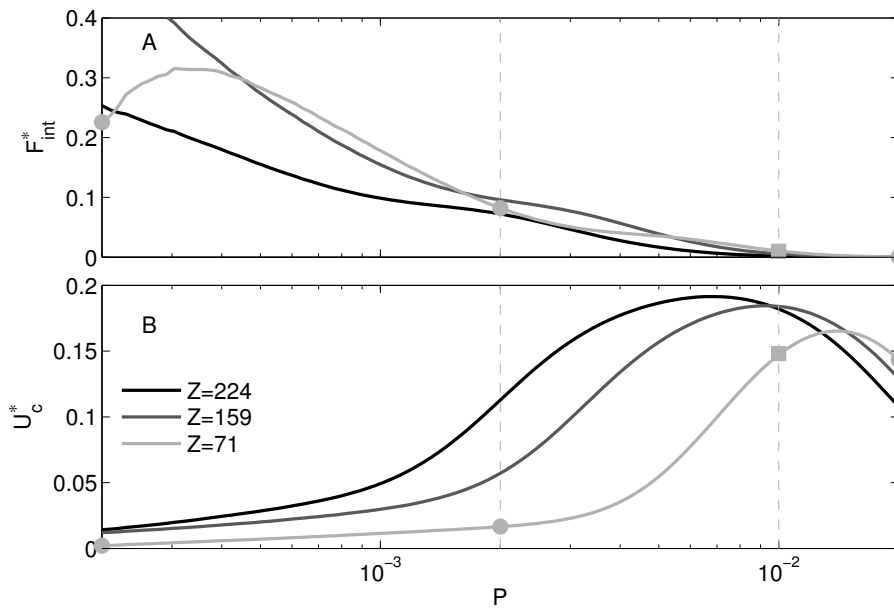


Figure 2.9.: Variability of (a) non-dimensional integrated SPM transport, and (b) non-dimensional bulk transport velocity as a function of the non-dimensional sinking speed P and stratification parameter Z . Parameters correspond to Case I (supercritical forcing, see Tab. 2.3). The square marks Case 1 (Tab. 2.2); dots indicate the variations of Case 1 shown in Fig. 2.5.

2.5.1. Supercritical forcing

Non-dimensional transports and transport velocities for the simulations with supercritical forcing and therefore subcritical slopes (Case I in Tab. 2.3) are shown in Fig. 2.9. This figure reveals, that, for the whole parameter range studied here, the non-dimensional transport F_x^* is positive, suggesting that suspended material is generally transported in the upslope direction for subcritical slopes. Transport rates exhibit a decreasing trend for increasing sinking speeds (Fig. 2.9a), which is explained, to first order, by the fact that higher sinking speeds imply smaller SPM concentrations, and thus smaller net transports. As this effect masks some of the dynamics, it is, however,

more instructive to consider the behavior of the bulk transport velocity U_c^* defined in (2.26), which may be viewed as a normalized version of F_x^* in which this direct concentration effect has been removed. Fig. 2.9b shows that the dependency of this quantity on P is similar for all values of Z , with low transport velocities observed for the smallest and largest sinking speeds, respectively, and a single maximum for moderately large values of the order of $P = 10^{-2}$.

The decay of U_c^* for the largest values of P is easily understood from the fact that in these cases, most of the SPM is located very close to the bottom, i.e. in a region with reduced velocities due to the effect of bottom friction. In the limiting case of very large P , we would therefore expect a total collapse of the upslope transport. Small values of U_c^* are also found for the opposite case of very small sinking speeds, where SPM is distributed nearly homogeneously across the BBL. As discussed above in the context of Fig. 2.5a, the transport in this case is determined by the residual flow rather than tidal pumping, implying that the upslope transport near the bottom and the downslope transport above nearly cancel. Although U_c^* tends to zero for small P , the same is not true for the transport F_x^* (Fig. 2.9a), which is largely determined by the strong accumulation of SPM in the BBL due to the reduced deposition of eroded material. These cases with very small sinking speeds, however, involve long transients before periodic conditions are reached, which may rarely be achieved in nature.

For intermediate sinking speeds, Fig. 2.9b reveals a continuous increase of U_c^* for increasing P until a maximum value of $U_c^* = 0.15 - 0.2$ is reached, depending on stratification. Assuming a M_2 tide with a typical velocity amplitude of 1 m s^{-1} , this corresponds to a distance of $\Delta x = 6.7 - 8.9 \text{ km}$ over which suspended material is transport upslope during one tidal cycle. Physically, the increase in U_c^* in this parameter range represents the transition between the situation shown in Fig. 2.5b, in which the transports in the upper and lower parts of the BBL largely compensate, and the more efficient single-layer transport due to classical tidal pumping in the near-bottom region as discussed above in the context of Fig. 2.4b,c and Fig. 2.5c (these cases are also marked in Fig. 2.9). It is remarkable that the maximum transport velocities for the different values of Z exhibit only a small variability, despite the fact that the BBL thickness varies by a factor of 2.5. The overall conclusion from these numerical experiments is that the transport of SPM is positive (upslope) for supercritical forcing (subcritical slopes), with the highest transport velocities found for moderately high sinking speeds as a result of classical tidal pumping.

2.5.2. Subcritical forcing

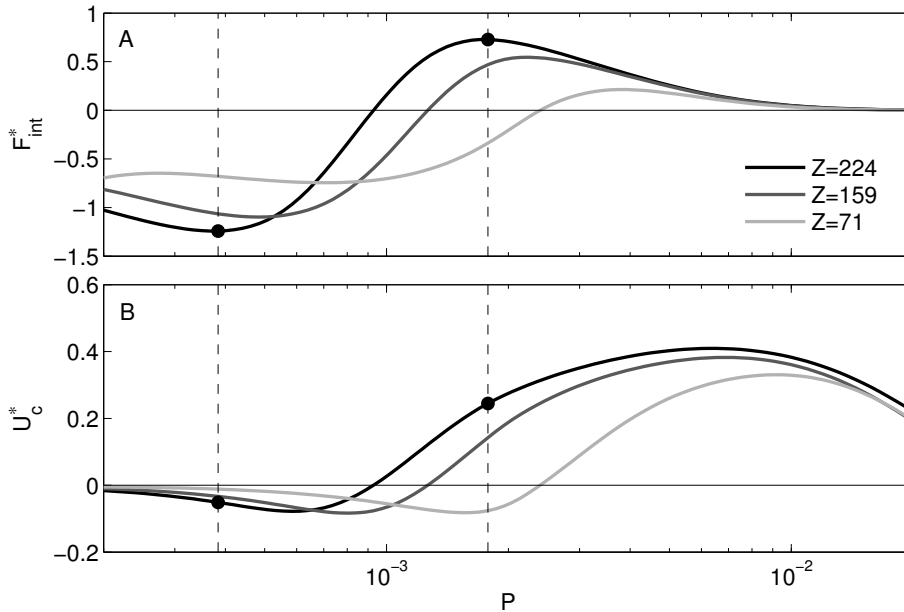


Figure 2.10.: As in Fig. 2.9 but now for Case II (subcritical forcing, see Tab. 2.3). Markers indicate Cases 2 and 3 (Tab. 2.2).

Results for Case II with subcritical forcing / supercritical slopes (Tab. 2.3) are displayed in Fig. 2.10. While the transports and transport velocities show the same trends, and do so for the same reasons, as for the cases with supercritical forcing for very small and large sinking speeds, respectively, there is one important difference. Below a certain threshold of the sinking speed P that depends on the stratification parameter Z , the transport now changes direction, and becomes negative (downslope). This transition was explained in the context of Fig. 2.8 as a result of the decreasing importance of upslope tidal pumping in the upper part of the domain for decreasing settling velocities. For slowly sinking material, part of the SPM that has been mixed up high into the water column during the energetic upslope flow phase remains suspended in the non-turbulent region above the much thinner BBL during downslope flow, thus partly compensating the previous upslope transport. Due to this compensating effect in the upper part of the domain, the total transport is therefore dominated by the near-bottom residual transport, which is downslope due to the inverse pumping mechanism described above.

For quickly sinking material, however, no suspended material is found in the non-turbulent restratified upper part of the domain that develops during downslope flow. Tidal pumping above the level of the thin downwelling BBL is therefore extremely

efficient, leading to bulk transport velocities that reach up to 40% of the tidal velocity amplitude (Fig. 2.10b). We conclude that for both super- and subcritical forcing, the most efficient upslope transport occurs for material with moderately large sinking speeds due to classical tidal pumping. The transport velocities in the subcritical regime, however, are about twice as large compared to the cases with supercritical forcing.

2.5.3. The effect of the slope angle

The parameters in all previous examples have been carefully chosen to insure that the forcing frequency ω is not in the vicinity of the critical frequency ω_c for BBL resonance, where some of the model assumptions are likely to break down (see above). In the following analysis, however, we study the model behavior across the entire range of oceanographically relevant slopes, including the transition from sub- to supercritical slopes. The parameters for these simulations correspond to Case III in Tab. 2.3.

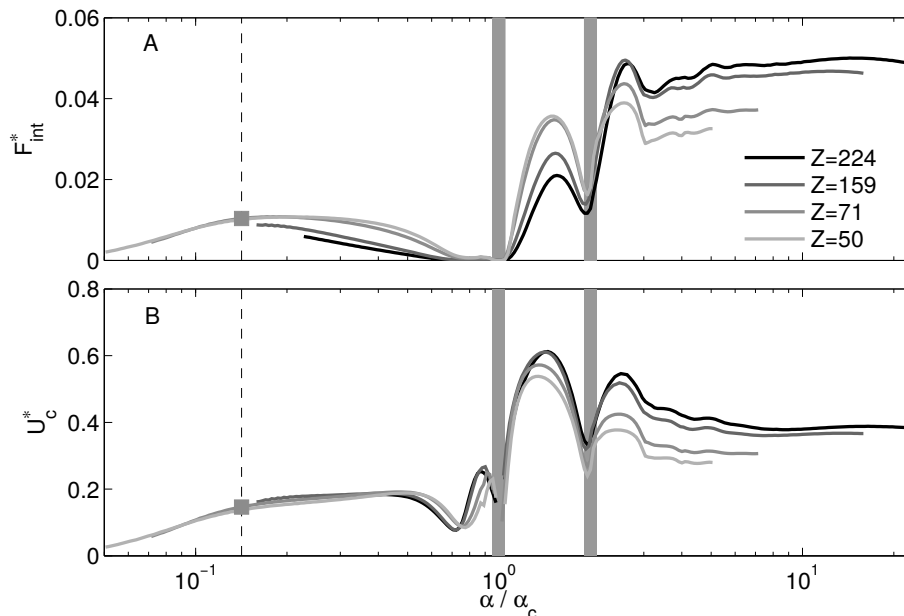


Figure 2.11.: Variability of (a) non-dimensional integrated SPM transport, and (b) non-dimensional bulk transport velocity as a function of normalized slope angle and non-dimensional stratification. Gray-shaded areas indicate the slopes for BBL resonance and the first harmonics, respectively. Parameters correspond to Case III (variable forcing, Tab. 2.3). The marker indicates Case 1 (Tab. 2.2).

To emphasize the model behavior near critical slopes, in Fig. 2.11 the slope angle has been normalized by the critical angle $\alpha_c = \omega / N_\infty$, found from inverting (2.11).

As shown in the following, the model exhibits a particular behavior near slopes that correspond to the critical ($\alpha/\alpha_c = 1$) or twice the critical slope ($\alpha/\alpha_c = 2$), which are therefore indicated in the figure. The non-dimensional sinking velocity in these examples corresponds to $P = 10^{-2}$, which is close to the efficiency maximum for tidal pumping as discussed above.

Most obvious from these simulations is the strong increase of both the SPM transport and the transport velocities at the transition from sub- to supercritical slopes, consistent with the results discussed in the preceding sections. Remarkable are the high residual transport velocities for slightly supercritical slopes ($\alpha \approx 1.4\alpha_c$), where U_c may reach up to 60% of the tidal velocity amplitude. In the immediate vicinity of critical slopes, however, where the BBL resonantly oscillates at the forcing frequency, the transport breaks down. A related observations was made by Umlauf and Burchard [2011], who pointed out the irreversible upslope buoyancy flux collapses if the BBL is resonantly forced. Interestingly, our results also reveal a reduction of the transport for $\alpha/\alpha_c = 2$, which may be understood from the fact that this case represents the first harmonic, where the BBL oscillates at exactly twice the forcing frequency.

As suggested already by the results shown in Figs. 2.9 and 2.10, the interpretation of the influence of stratification is complicated by the strong dependency of the transport rates on the non-dimensional settling velocity P . A robust result, however, seems to be that transport rates in the strongly supercritical range ($\alpha > 2\alpha_c$) show a systematic increase with increasing stratification.

2.6. Discussion and conclusions

As one of the most important results, our study suggests that periodic motions in the vicinity of sloping topography trigger a residual transport of suspended material that is, for most parameter combinations, directed upslope. The physical transport mechanisms resemble classical tidal pumping as described in the context of many previous studies on SPM transport in estuaries and regions of fresh water influence [ROFIs, Simpson 1997] in the coastal ocean. However, while classical tidal pumping critically depends on an externally imposed horizontal density gradient, tidal pumping near sloping topography only requires: a slope, vertical stratification, and an oscillating near-bottom current that may be associated with tidal motions, or, likewise, with any other energetic periodic process including near-inertial waves, topographically trapped

waves, and internal seiching motions. This combination of factors is nearly ubiquitous in the ocean and in lakes, and we expect that the same is true for the new transport mechanism described here.

Our analysis also showed that the residual transport is governed by five non-dimensional parameters, among them the ratio $P = w_s/U$ of the sinking speed and the tidal velocity amplitude, which was found to determine the effectiveness of tidal pumping. The highest transport velocities are found for values of the order of $P = 10^{-2}$, i.e. for material with moderately high sinking speeds, assuming a typical tidal velocity range. For even higher sinking speeds, suspended material remains in a thin near-bottom layer, where the transport is inhibited by the effect of bottom friction. For lower sinking speeds, tidal pumping becomes less efficient.

Beyond the non-dimensional sinking speed P , also the roughness number $R = z_0\omega/U$, the topographic slope α , and the non-dimensional stratification $Z = N_\infty/\omega$ (the latter two defining the transition from super- to subcritical forcing) turned out to be important parameters. A direct comparison of these non-dimensional parameters with those found in studies of classical tidal straining in estuaries and ROFIs is, however, complicated by the fact that the water depth H (one of the key parameters in classical tidal straining) does not appear in our geometry. Some analogies between both types of problems can nevertheless be identified, noting that the key parameters in classical tidal straining are: the Simpson number, $\text{Si} = H^2\partial b/\partial x/U^2$, the unsteadiness number, $\text{Un} = \omega H/U$, and the length scale ratio $A = z_0/H$ [e.g., Burchard and Hetland 2010; Burchard et al. 2013]. Recalling that the (quasi-)horizontal density gradient in our case can be expressed as $\partial b/\partial x = N_\infty^2\alpha$ for mild slopes ($\alpha \ll 1$), it is easy to show that $\text{Si} A^2 = \alpha Z^2 R^2$ and $\text{Un} A = R$, where the left and right hand sides represent classical and sloping tidal straining, respectively. Note that some authors identify the velocity scale U with a bulk friction velocity, $U_* \propto U$, which is qualitatively equivalent.

Our numerical experiments showed that due to the more pronounced tidal asymmetries for supercritical slopes, SPM transport by tidal pumping is substantially more efficient than for subcritical α . The sensitivity of the cross-slope fluxes with respect to variations of the slope angle and ambient stratification implies that the transport of suspended material near real oceanic slopes, which are in general neither uniform nor uniformly stratified, exhibits regions of convergence or divergence of suspended material. This is analogous to the convergence/divergence of cross-slope buoyancy fluxes discussed by Garrett [1991]. The results in Section 2.5 have shown that the upslope SPM flux strongly increases during the transition from subcritical to super-

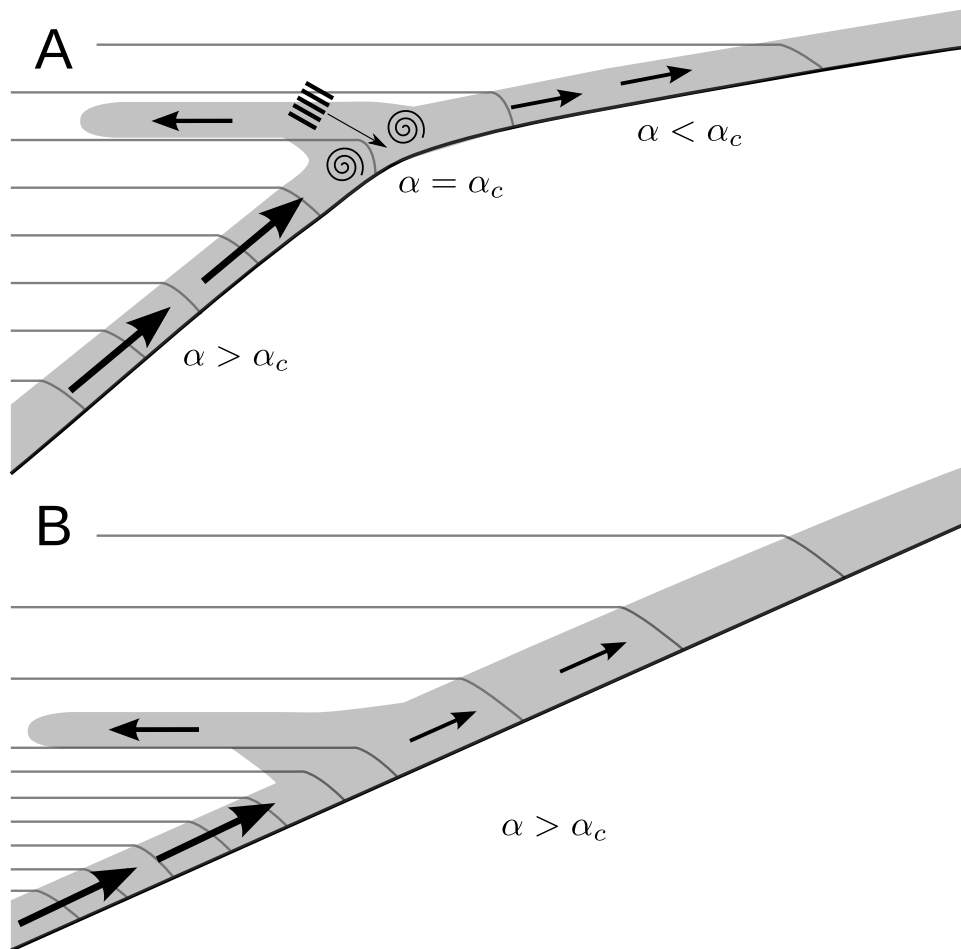


Figure 2.12.: Sketch of possible SPM transport pathways for (a) convex topography with varying slope angle and internal-wave breaking at the critical slope region as indicated, and (b) changes in stratification: a pycnocline below a less stratified water body over a supercritical slope. Gray-shaded regions indicate suspended material, arrows depict the residual transport of SPM, and gray lines denote isopycnals.

critical slopes (see Fig. 2.11). It may therefore be speculated that the convergence of suspended material in the vicinity of critical slopes is balanced by isopycnal intrusions of SPM towards the interior, possibly promoted by the strong turbulence usually associated with the critical breaking of internal waves (Fig. 2.12a). Similarly, for supercritical slopes, a convergence of upslope transports is expected at the transition from a region of strong to weak stratification (see Fig. 2.11), e.g. in the upper part of a pycnocline. As pycnoclines are often regions of enhanced internal-wave activity, it may be argued that the accumulated material is resuspended and transported inside the pycnocline towards the interior (Fig. 2.12b). These speculations can, however, only be

substantiated with the help of a two- or three-dimensional modeling approach, which is beyond the scope of our study.

In the present investigation, we have concentrated on the basic mechanisms of SPM transport due to tidal straining near sloping topography, ignoring, for simplicity, numerous effects that may become relevant in more realistic scenarios. These include, besides the effects of the cross-slope inhomogeneities mentioned above: the effects of Earth rotation, the role of secondary currents induced by topographic features like submarine channels or ridges, and the impact of turbulence on the properties of SPM that all have been shown to significantly modify the mechanisms of classical tidal straining and residual SPM transport [e.g., MacCready and Geyer 2010; Schulz et al. 2015; Scully and Friedrichs 2003]. The impact of these processes on the dynamics of tidal straining near sloping topography will have to be clarified in future studies. We have also emphasized the role of suspended material here but it should be clear that also bed load transport [van Rijn 1984a] may provide an essential contribution to the overall cross-slope transport of particulate matter. It is likely that the tidal asymmetry in the bottom stress that we observed in all our simulations (see, e.g., Fig. 2.3e) leads to a residual bed load transport — but also this aspect requires a further analysis.

Chapter 3.

Slope-induced tidal straining: Analysis of rotational effects

Tidal straining is known to be an important factor for the generation of residual currents and transports of suspended matter in the coastal ocean. Recent modeling studies and field experiments have revealed a new type of “slope-induced” tidal straining, in which the horizontal density gradient required for this process is induced by the presence of a slope rather than by river runoff (as in classical tidal straining). Slope-induced tidal straining is investigated here with the help of an idealized numerical model, and results are compared to a recent data set from the East China Sea providing first direct observational evidence. The focus of this study is on the effect of rotation that was ignored in previous investigations. The model is shown to reproduce the key features of the observations, in particular the strain-induced generation of unstable stratification in the bottom boundary layer during periods of upslope flow. Rotation effects are found to significantly reduce the upslope tidal pumping of suspended material but also give rise to a newly identified pumping mechanism that results in a vigorous transport of suspended material along the slope. It is shown that slope-induced tidal straining is likely to be relevant for a wide range of oceanic slopes exposed to tidal motions.

3.1. Introduction

In many estuaries and regions of the coastal ocean, the tidal dynamics and the generation of residual transports are strongly modified by the presence of a horizontal

density gradient, typically maintained by river runoff or differential heating. In these cases, the horizontal density gradient interacts with the vertical tidal shear to induce a periodic modulation of the vertical density structure that is usually referred to as Strain-Induced Periodic Stratification (SIPS). During flood, dense water is advected on top of lighter water, thus destabilizing the water column, whereas during ebb, light water is transported on top of denser water, inducing stable stratification [van Aken 1986; Simpson et al. 1990].

MacCready and Geyer [2014] summarized the present understanding of the dynamical implications of this tidal straining process, highlighting in particular the role of SIPS for the generation of tidal asymmetries in mixing (see their Fig. 2). They pointed out that the generally larger turbulent diffusivities observed during the less stratified flood phase are reflected in tidal asymmetries in the velocity profiles, inducing a landward residual circulation near the bottom, and a seaward return current in the upper part of the water column. From extensive numerical experiments, Burchard and Hetland [2010] concluded that in tidally energetic systems the contribution of this “tidal straining circulation” to the total residual circulation may be significantly larger than the gravitationally-driven component, challenging the classical view of estuarine circulation.

Jay and Musiak [1994] proposed that the mixing asymmetries due to SIPS may also have a profound impact on the residual transport of suspended material. These authors showed that due to stronger turbulence during the flood phase, high concentrations of suspended material are generally correlated with flood currents (directed landward), thus inducing a residual landward transport of suspended material [Uncles et al. 1985; Jay and Musiak 1994; Scully and Friedrichs 2007]. Idealized numerical experiments revealed that this “tidal pumping” mechanism generally dominates over the advection of suspended material by the residual current [Burchard et al. 2013].

In a recent modeling study, Schulz and Umlauf [2016] proposed that similar tidal straining and pumping processes may occur also in vicinity of a topographic slope — with the important difference, however, that no externally imposed horizontal density gradient (e.g., due to river runoff) is required. In this case, the (quasi-)horizontal density gradient is generated by the projection of the vertical interior density gradient onto the slope (Fig. 3.1). Slope-induced tidal straining is confined to a turbulent bottom boundary layer (BBL), but the process is otherwise completely analogous to classical tidal straining over a flat bottom: during upslope flow, dense water is advected on top of lighter water, resulting in unstable stratification, enhanced near-bottom turbu-

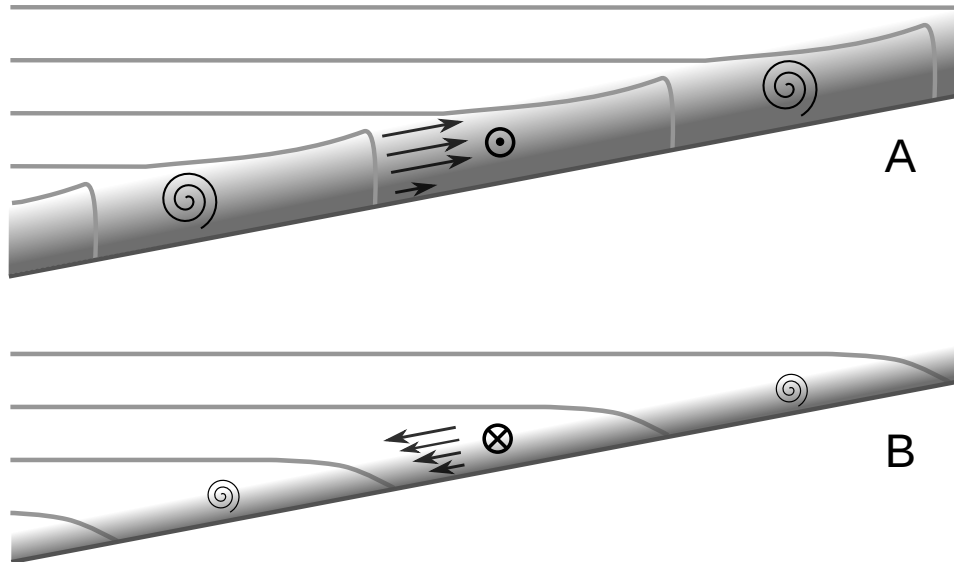


Figure 3.1.: Slope-induced tidal straining causing (a) unstable stratification during upslope flow and (b) stable stratification during downslope flow (SIPS). Gray lines denote isopycnals, arrows show the current direction. Gray-shaded areas near the bottom indicate the presence of suspended material; spirals symbolize near-bottom turbulence.

lence, and high concentrations of suspended material (Fig. 3.1a). Vice-versa, during downslope flow, the straining of the cross-slope density gradient induces a tendency for increasing stratification inside the BBL, which in turn leads to reduced BBL turbulence, smaller BBL thicknesses, and lower sediment concentrations. Using an idealized one-dimensional (slope-normal) numerical model, Schulz and Umlauf [2016] showed that tidal pumping leads to a net cross-slope transport of suspended material, similar to the tidal pumping mechanism over a flat bottom described by Jay and Musiak [1994]. In their study, Schulz and Umlauf [2016] ignored the effect of rotation, which may, however, be essential in many realistic settings. This point will therefore be investigated in detail in the following analysis.

First observational evidence for slope-induced tidal straining was recently discussed by Endoh et al. [2016], who analyzed an extensive data set, including turbulence microstructure observations, from a topographic slope exposed to strong tidal currents in the East China Sea. These authors described a periodic destabilization of the water column during periods with upslope tidal currents, induced by the presence of a persistent cross-slope density gradient. The latter turned out to be consistent with

the projection of the vertical density gradient onto the slope, and therefore with the importance of slope-induced tidal straining.

Here, we attempt to clarify the mechanisms, implications, and relevance of slope-induced tidal straining on a real oceanic shelf by combining the results from previous modeling studies by Umlauf and Burchard [2011] and Schulz and Umlauf [2016] with the experimental data by Endoh et al. [2016]. In section 3.2, we extend the model used by Schulz and Umlauf [2016] to include the effects of rotation before we briefly summarize the field observations discussed by Endoh et al. [2016] in section 3.3. After deriving model parameters from these observations in section 3.4, we discuss the model results in section 3.5, and compare them to the field data. The implications of tidal straining for the generation of residual currents and the residual transport of suspended material are analyzed in section 3.6 before we draw some conclusions in section 3.7.

3.2. Model description

3.2.1. Model geometry

Following previous modeling studies of slope-induced straining [Umlauf and Burchard 2011; Schulz and Umlauf 2016], we investigate in the following the motion of a vertically stratified Boussinesq fluid in the vicinity of a uniform slope with slope angle α . The geometry is two-dimensional with the horizontal and vertical coordinates denoted by \hat{x} and \hat{z} , respectively, and the fluid is assumed to rotate with angular velocity $f/2$ about the vertical axes (Fig. 3.2). Vertical stratification is quantified with the help of the buoyancy frequency,

$$N^2 = \frac{\partial b}{\partial \hat{z}}, \quad (3.1)$$

where b denotes buoyancy. Above the BBL, we assume that isopycnals remain strictly horizontal during all times, and that N^2 approaches the constant background value N_∞^2 . Close to the bottom, however, isopycnals will be distorted as a result of boundary mixing, and the local buoyancy b will differ from the equilibrium buoyancy b_∞ (black and gray lines Fig. 3.2).

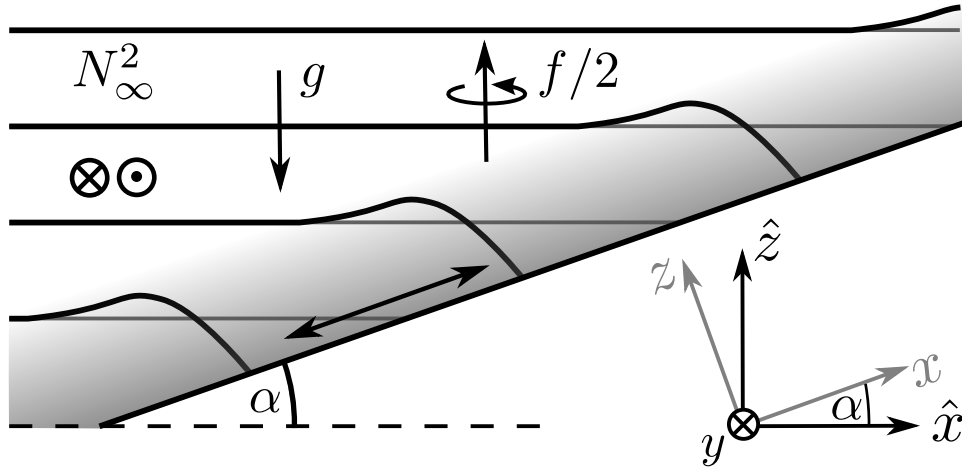


Figure 3.2.: Schematic view of the model geometry and density structure (black lines) near a uniform slope with slope angle α . Gray lines indicate isopycnal equilibrium levels ($b_\infty = \text{const.}$). Upslope and slope-normal coordinates are denoted by x and z , respectively. Arrows symbolize the oscillating near-bottom currents.

Introducing a rotated coordinate system with the cross-slope, along-slope, and slope-normal coordinates denoted by x , y , and z (see Fig. 3.2), it can be shown from simple geometrical arguments that under the above conditions also the cross-slope buoyancy gradient is constant:

$$\frac{\partial b}{\partial x} = N_\infty^2 \sin \alpha, \quad (3.2)$$

illustrating the generation of a quasi-horizontal ($\alpha \ll 1$) buoyancy gradient by the projection of the purely vertical interior stratification onto the slope [Garrett et al. 1993; Umlauf and Burchard 2011].

3.2.2. Model equations

Assuming that all cross-slope and along-slope gradients vanish, except the cross-slope buoyancy gradient defined in (3.2), the problem becomes geometrically one-dimensional in the slope-normal z -direction. The Boussinesq equations can then be written as [Um-

lauf et al. 2015]:

$$\frac{\partial u}{\partial t} - f v \cos \alpha = (b - b_\infty) \sin \alpha + P_x - \frac{\partial \tau_x}{\partial z}, \quad (3.3)$$

$$\frac{\partial v}{\partial t} + f u \cos \alpha = P_y - \frac{\partial \tau_y}{\partial z}, \quad (3.4)$$

$$\frac{\partial b}{\partial t} = -u N_\infty^2 \sin \alpha - \frac{\partial G}{\partial z}, \quad (3.5)$$

with u and v denoting the upslope and along-slope velocities, and τ_x , τ_y and G the slope-normal turbulent fluxes of momentum (per unit mass) and buoyancy, respectively. $P_x(t)$ and $P_y(t)$ are integration constants that play the role of prescribed external pressure gradients. The cross-slope buoyancy gradient in the advection term in (3.5) has been expressed with the help of (3.2). Note that in contrast to previous studies of slope-induced tidal straining that only considered the plane non-rotating case ($f = 0$, $v = 0$), equations (3.3) – (3.5) now include rotational effects that turned out to be essential to describe the motions at our study site.

The equilibrium buoyancy b_∞ appearing in the first term on the right hand side of (3.3) evolves as a result of cross-slope buoyancy advection, and can therefore be described by an advection equation of the form.

$$\frac{\partial b_\infty}{\partial t} + u_\infty N_\infty^2 \sin \alpha = 0, \quad (3.6)$$

which directly follows from (3.5) for $z \rightarrow \infty$.

Far away from the boundary ($z \rightarrow \infty$), we assume that all slope-normal gradients, except the buoyancy gradient vanish, whereas at the lower boundary ($z = 0$) we use the boundary conditions

$$u = v = 0, \quad \frac{\partial b}{\partial z} = 0. \quad (3.7)$$

Schulz and Umlauf [2016] also discussed a simple transport equation for the concentration c of suspended particulate material (SPM) exhibiting a vertical sinking motion w_s relative to the moving fluid:

$$\frac{\partial c}{\partial t} = -\frac{\partial}{\partial z} (F_z - c w_s \cos \alpha), \quad (3.8)$$

where F_z is the slope-normal turbulent SPM flux. At the bottom, this flux equals the erosion flux:

$$F_z = \alpha_e \max \left\{ \frac{|\tau_b|}{\tau_c} - 1, 0 \right\} \quad \text{at } z = 0, \quad (3.9)$$

where α_e is the erosion parameter, τ_b the bottom stress, and τ_c the critical shear stress for erosion.

The turbulent fluxes appearing in (3.3) – (3.5) and (3.8) are computed from gradient expressions of the form

$$\tau_x = -\nu_t \frac{\partial u}{\partial z}, \quad \tau_y = -\nu_t \frac{\partial v}{\partial z}, \quad G = -\nu_t^b \frac{\partial b}{\partial z}, \quad F_z = -\nu_t^b \frac{\partial c}{\partial z}, \quad (3.10)$$

where ν_t is the turbulent viscosity, and ν_t^b the turbulent diffusivity of buoyancy and SPM. The diffusivities are computed from a second-moment turbulence model that includes two prognostic equations for the turbulent kinetic energy k and the dissipation rate ε . This turbulence model is identical to that described in detail in Umlauf and Burchard [2011], Umlauf et al. [2015], and Schulz and Umlauf [2016], and, for brevity, this description is not repeated here. The general properties of this class of turbulence models are reviewed in Umlauf and Burchard [2005]; details about the numerical implementation may be found in Umlauf et al. [2005]. In the non-turbulent region above the BBL ($z \rightarrow \infty$), the turbulent fluxes are assumed to vanish. Also, as we only investigate flows at high Reynolds number in this study, all molecular fluxes are ignored.

3.2.3. Model properties

In the following, we will assume that BBL motions are driven by a harmonic horizontal pressure force pointing into an arbitrary horizontal direction, here referred to as the n -direction:

$$P_n = P \cos(\omega t + \phi), \quad (3.11)$$

where ω is the forcing frequency, ϕ the phase, and P the magnitude of the pressure force. Denoting the angle between the n - and x -directions as β , the components of P_n in the x - and y -directions are $P_x = P_n \cos \beta$ and $P_y = P_n \sin \beta$. It is straightforward to

show from (3.3) and (3.4) that for the harmonic forcing in (3.11), the velocities in the inviscid region above the BBL ($z \rightarrow \infty$) are described by

$$u_n = P \frac{\omega}{\omega^2 - f^2} \sin(\omega t + \phi) \quad (3.12)$$

$$u_s = P \frac{f}{\omega^2 - f^2} \cos(\omega t + \phi), \quad (3.13)$$

with u_n and u_s denoting the components in the n - and s -directions, respectively (the latter obtained from rotating the y -axis by the angle β). For $\omega > f$, the velocity vector is seen to anti-cyclonically trace an ellipse with axes ratio $e = \omega/f$, where the main axis points into the direction of the pressure gradient. Due to the lack of viscous damping in the non-turbulent layer above the BBL, velocities increase toward infinity if resonance is reached ($\omega = f$). The harmonic pressure term in (3.11) will be used below as a simple representation of tidal forcing in a rotating system

The situation becomes more complex inside the BBL due to the appearance of the internal pressure term $(b - b_\infty) \sin \alpha$ in (3.3). Umlauf et al. [2015] showed that this term represents the tendency of isopycnals to relax back to their equilibrium positions ($b = b_\infty$), which implies the possibility of reversible BBL oscillations at the frequency

$$\omega_c^2 = f^2 \cos^2 \alpha + N_\infty^2 \sin^2 \alpha, \quad (3.14)$$

indicating that BBL resonance occurs for $\omega = \omega_c$ [Umlauf and Burchard 2011]. Vice-versa, if N_∞ , f , and ω are considered to be given, BBL resonance will be observed if the slope α approaches the critical slope α_c found from inverting (3.14). Model properties exhibit qualitative changes during the transition from subcritical to supercritical slopes, and some of the model assumptions break down near critical slopes [Umlauf and Burchard 2011; Schulz and Umlauf 2016].

Near the geographic location investigated in this study, the parameters N_∞^2 , f , and α are derived in the chapters below and summarized in Tab. 3.1. The frequency for critical boundary layer resonance derived from these parameters is $\omega_c = 7.69 \times 10^{-5} \text{ s}^{-1}$, corresponding to a period of $T_c = 22.7 \text{ h}$. As discussed in more detail below, the proximity of T_c to the diurnal tidal period is one of the reason why the diurnal tides are neglected in our model analysis.

Finally, for the following discussion of residual transports it is useful to note that Umlauf and Burchard [2011] showed that under the above conditions (harmonic forc-

Table 3.1.: Standard parameters used for the simulations in sections 3.5 and 3.6

α	N_∞^2	f	z_0	τ_c	α_e
3×10^{-4}	$6.5 \times 10^{-4} \text{ s}^{-2}$	$7.65 \times 10^{-5} \text{ s}^{-1}$	10^{-3} m	$10^{-4} \text{ m}^2 \text{ s}^{-2}$	$10^{-4} \text{ kg s}^{-1} \text{ m}^{-2}$

ing, zero mixing above the BBL), the residual upslope transport vanishes

$$\int_0^\infty \langle u \rangle dz = 0, \quad (3.15)$$

where the angular brackets denote the average over one forcing period $T = 2\pi/\omega$.

3.3. Study site and methods

3.3.1. Study site

In July 2011, hydrographic and turbulence microstructure measurements were performed near position S in the East China Sea (Fig. 3.3). The study site was located at $31^\circ 44.9' \text{ N}$, $125^\circ 50.0' \text{ E}$ on a mildly sloping continental shelf at approximately 68 m water depth. The inertial period at this latitude is $T_f = 23.3$ hours. Based on a finite-element global ocean tidal model with a regionally refined numerical grid, Lefevre et al. [2000] showed that the East China Sea is subject of strong tidal motions with the four major constituents being: the principal lunar and solar tides, M_2 and S_2 , with semi-diurnal periods, and the luni-solar and principal lunar diurnal tides, K_1 and O_1 , respectively. The M_2 tide is dominant here, about three times stronger than the second largest tidal component, the S_2 . The two diurnal tides are of similar magnitude and about 4 times weaker than the M_2 component. Similar results were derived from observations of current velocity data at $31^\circ 45' \text{ N}$, $127^\circ 25' \text{ E}$ (east of position S) [Yoshikawa et al. 2012]. It should be noted that the inertial period is close to the periods of the diurnal tides, precluding a straightforward spectral distinction between diurnal tidal and near-inertial signals in a short time series.

Fig. 3.3 illustrates that position S is located approximately 400 km away from the Changjiang river mouth, which forms the by far largest freshwater source in this region. Endoh et al. [2016] pointed out that this large spatial separation, and the fact that the less dense river water will mainly affect the near-surface layer during the ther-

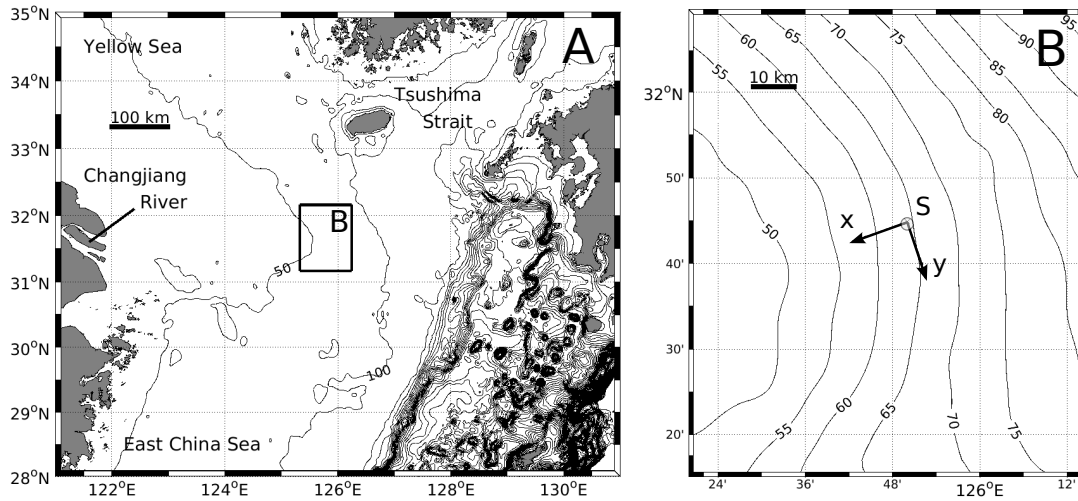


Figure 3.3.: Maps of (a) East China Sea, and (b) study area with deployment location “S”. Local cross-slope and along-slope directions are denoted by x and y (rotated by 20 degrees with respect to the zonal and meridional directions, respectively). Bathymetry is in meters, based on bathymetric data described in Choi et al. [2002].

mally stratified summer period, suggests that the BBL at position S is unlikely to be dynamically influenced by freshwater runoff.

In the area of interest, the main axis of the bottom slope, i.e. the direction of maximum inclination, is orientated approximately 20 degrees relative to the zonal direction (Fig. 3.3b). To be consistent with the model geometry shown in Fig. 3.2, we introduce a local coordinate system with the x - and y -axes pointing in the upslope and along-slope directions, respectively, as indicated in Fig. 3.3b. Using an identical coordinate system, Endoh et al. [2016] showed that the along-slope density gradient is nearly negligible compared to the cross-slope gradient. They also found that the observed periodic density variations in the BBL were largely caused the by up- and downslope advection of isopycnals due to the tides, which forms the most important prerequisite for the occurrence of slope-induced tidal straining (see Fig. 3.1).

Echosounding data from the cruise (not shown) showed that the bathymetry exhibits a nearly perfectly linear slope in the x -direction on horizontal scales of the order of a few tens of kilometers. According to these data, the topographic slope is approximately 3×10^{-4} , which is also taken as the default value for the numerical simulations described below. Several bathymetric data sets for the East China Sea are available, but due to their coarse resolution the slope angle near position S tends to be somewhat

overestimated. Recent topographic data discussed in Choi et al. [2002] suggests, e.g., a slope of nearly 6×10^{-4} near the study site. The sensitivity of our results with respect to these uncertainties in the slope angle will be discussed in Appendix B.

3.3.2. Methods

The dataset we discuss here was collected with a 600-kHz ADCP (Workhorse from Teledyne RD Instruments) and a tethered turbulence microstructure profiler (TurboMAP-5 from JFE Advantech, Japan) during a cruise of the training ship Nagasaki-Maru in July 2011. Echo sounding data were obtained with a KFC-300 quantitative echo sounder from Sonic, Japan.

The ADCP was mounted on a trawl-resistant bottom frame, and deployed on the seabed from 16:40 JST (Japan Standard Time) on 16 July to 15:40 JST on 21 July. The vertical bin size was set to 1 m, and the depth of the first bin was located 3 m above the seabed, i.e. at approximately 65 m depth. The ADCP was operated in standard RDI “mode 1”, sampling the along-beam velocities at a rate of 1.3 Hz during 20-minute bursts starting every half hour. From the along-beam velocities averaged over 20 minutes (1600 pings), the horizontal components of the velocity were calculated at half-hour intervals.

The microstructure profiler was deployed from the ship within about 500 m distance from the ADCP between 17:00 JST on 17 July and 06:00 JST on 19 July. While the profiler was freely descending at a speed of $0.5 - 0.6 \text{ m s}^{-1}$, vertical shear and temperature microstructure were sampled at a rate of 512 Hz, whereas temperature, conductivity, pressure, turbidity, fluorescence, and the acceleration of the instrument were sampled at a rate of 64 Hz. A total of 101 profiles between a depth of 10 m and the bottom were obtained. From the microscale vertical shear, the dissipation rate of turbulent kinetic energy, ε , was estimated, assuming locally isotropic turbulence [Hinze 1987] across 1-m windows as described in more detail in Endoh et al. [2016]. A series of 1-3 profiles taken approximately every hour was averaged to provide hourly means.

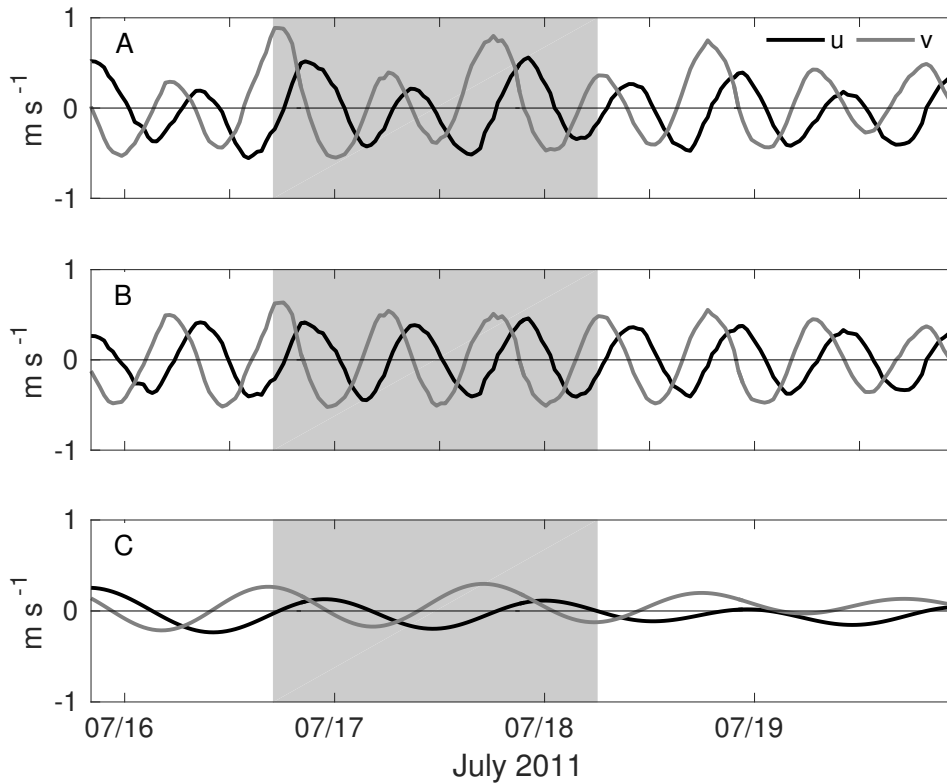


Figure 3.4.: Time-series of cross-slope (u) and along-slope (v) velocity components based on ADCP measurements in 30 m depth at position S: (a) unfiltered data, (b) highpass-filtered M_2 tidal currents, and (c) lowpass-filtered diurnal and subtidal currents. Period with microstructure measurements at position S is indicated in gray.

3.3.3. Analysis of tidal motions

Tidal forcing parameters for the idealized simulations described below were found by extracting the major tidal constituents from the velocities observed at position S. We performed this tidal analysis based on the velocity records at 30 m depth (38 m above the bottom), noting that results were not particularly sensitive with respect to small variations of this parameter. This choice for the ADCP reference level was found to be a reasonable compromise between data quality (deteriorating with increasing distance from the ADCP) and our attempt to reduce the impact of bottom friction (increasing towards the bottom). Prior to the following analysis, the velocities were projected onto the topography-following x - and y -directions shown in Fig. 3.3b.

To decompose the observed signals into semi-diurnal and diurnal components, we used a phase-preserving high-order filter with a cutoff frequency of 15 hours. Comparison of the unfiltered (Fig. 3.4a) and highpass-filtered semi-diurnal velocities (Fig.

3.4b) clearly shows that the currents at our study site were dominated by a regular M_2 tide with an amplitude of approximately 0.5 m s^{-1} , with slightly more energy in the along-slope direction. This tidal constituent explains approximately 83% of the total variance of the signal. The diurnal signal (Fig. 3.4c) is substantially weaker, and shows a clear trend for both decreasing magnitude and increasing frequency during the observational period. Pure tidal motions are unlikely to exhibit such variability on a time scale of only a few days, suggesting that the observed signal is a mixture of near-inertial motions, which may quickly vary in time due to their direct dependence on the wind forcing, and different diurnal tidal constituents.

It is worth noting that a detailed tidal model of the East China Sea by Xianwen et al. [2001] yields a velocity amplitude of approximately 0.5 m s^{-1} for the M_2 component at position S, in good agreement with our data. For the diurnal K_1 tide, velocity amplitudes around 0.1 m s^{-1} were found, approximately twice as large as those of the O_1 constituent. Our observations (see Fig. 3.4c) suggest that the model of Xianwen et al. [2001] slightly overestimates tidal motions in the diurnal frequency band.

3.4. Observations and model parameters

3.4.1. Observations

The observations at position S have been described in detail by Endoh et al. [2016]. Here, we only summarize their main findings to provide the context for the discussion of the models results below.

Fig. 3.5 shows the averaged vertical structure of salinity S , potential temperature θ , potential buoyancy b , and the (square of the) buoyancy frequency N^2 , based on the average of all profiles obtained at position S. Here, we define the buoyancy as $b = -g(\rho_\theta - \rho_0)/\rho_0$, where ρ_θ is potential density and $\rho_0 = 1000 \text{ kg m}^{-3}$ a constant reference density. The figure shows that the lower part of the water column is characterized by a nearly well-mixed BBL of more than 35 m thickness, capped by a strongly stratified “interior” region with approximately linear stratification, slightly larger than $N^2 = 10^{-3} \text{ s}^{-2}$. Inside the BBL, the average stratification is 1-2 orders of magnitude smaller compared to this interior region (Fig. 3.5d).

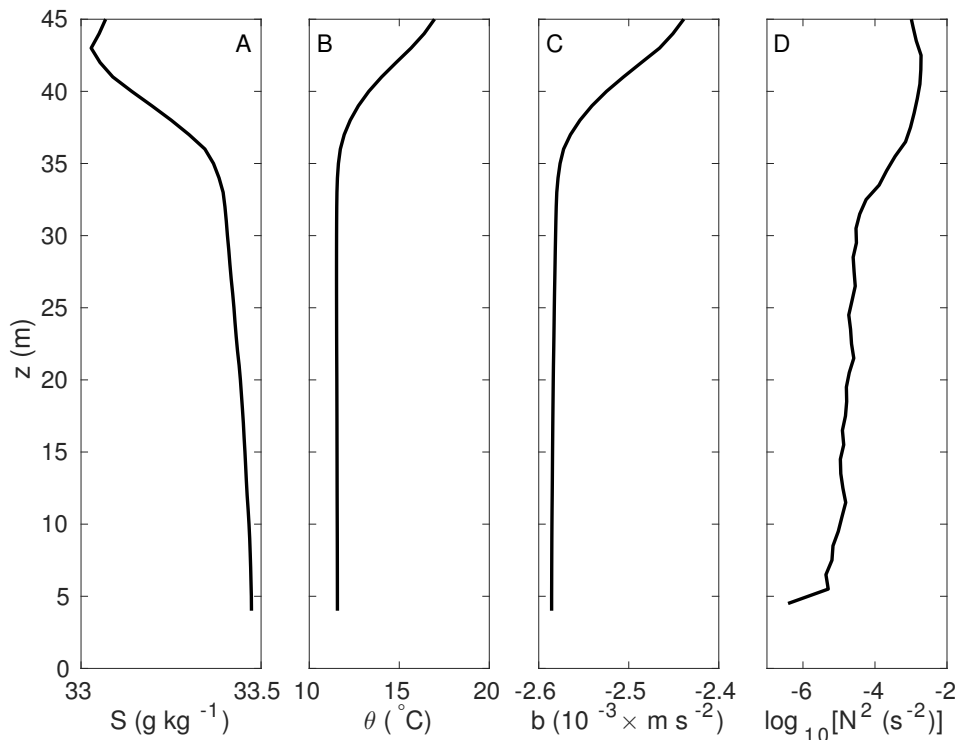


Figure 3.5.: Mean profiles of: (a) salinity, (b) potential temperature, (c) buoyancy, and (d) buoyancy frequency squared. Profiles are based on the average of all available microstructure profiles at station S (gray-shaded period in Fig. 3.4).

As already discussed in the context of Fig. 3.4, BBL velocities are dominated by regular M_2 tidal motions, however, with a significant diurnal modulation and indications for a frictional reduction of the tidal velocities toward the bottom (Fig. 3.6a,b). Also the buoyancy anomaly $\tilde{b} = b - \langle b \rangle$, where $\langle b \rangle$ denotes the tidally-averaged buoyancy shown in Fig. 3.5c, is characterized by a clear M_2 tidal variability with a $\pi/2$ phase lag with respect to the u -component (Fig. 3.6c). This phase shift is expected if buoyancy variations are due to advection of a constant cross-slope buoyancy gradient as mathematically described by (3.5).

In the context of the present study, the most interesting feature in these observations is the periodic destabilization of the lower part of the BBL (Fig. 3.6d) that Endoh et al. [2016] showed to be consistent with slope-induced tidal straining as delineated in Fig. 3.1. These unstable regions appear at the M_2 tidal frequency, exhibit a significant vertical phase shift, and affect a large fraction of the BBL. Beyond the key role played by the M_2 tidal currents in this processes a diurnal suppression of the vertical extent of the unstable regions is visible in Fig. 3.6c), which should be kept in

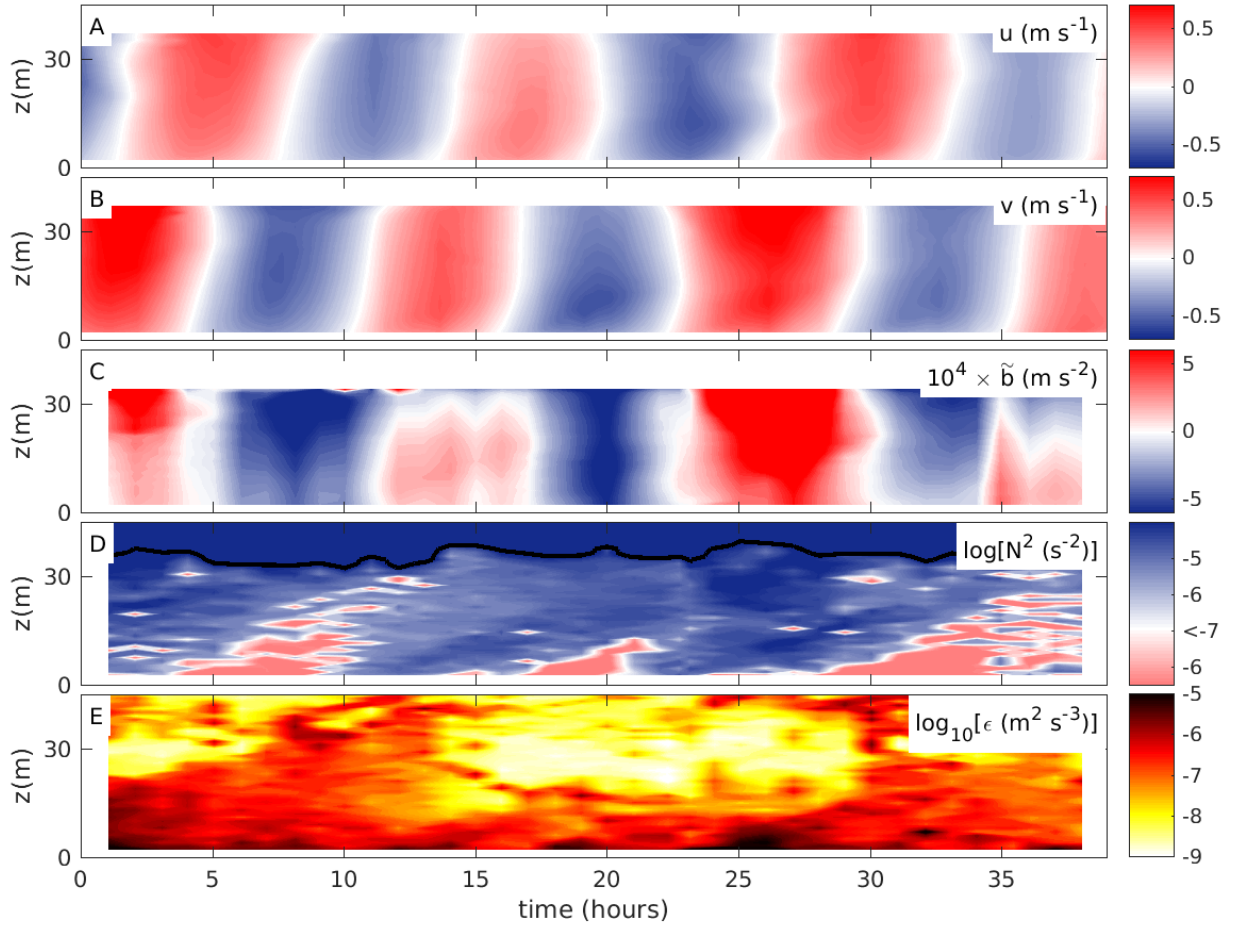


Figure 3.6.: Evolution of observed (a) cross-slope velocity, (b) along-slope velocity, (c) buoyancy fluctuations, (d) buoyancy frequency, and (e) turbulence dissipation rate. Note the special logarithmic color scale in (d): for $N^2 < 0$ (unstable stratification), the value of $|N^2|$ is plotted in red shading, whereas regions with positive N^2 are plotted in blue shading. The black line indicates values of $N^2 = 10^{-3.7} \text{ s}^{-2}$ and marks the vertical extent of the BBL. The time axis starts on 17 July 16:00 JST.

mind when interpreting the model results below (the diurnal signal is neglected in our model forcing).

Despite the dominant M_2 tidal forcing, the turbulence dissipation rates shown in Fig. 3.6d do not exhibit a clear tidal signal. This is easily understood from the fact that the near-bottom velocity vector at position S essentially rotates at the M_2 tidal frequency without large modulations in magnitude (Fig. 3.4c), different from previous field studies in regions with more rectilinear tides [e.g. Simpson et al. 2002; Burchard et al. 2002]. Noticeable is therefore in particular a diurnal modulation of the dissipa-

tion rate that is shown to be related to the vertical shear caused by the interference between diurnal and semidiurnal tidal currents rather than to the lateral advection of stratification in the upper part of the BBL [Wakata et al. 2016].

3.4.2. Model parameters

The solution of the system of equations in (3.3) - (3.7) depends on a number of model parameters that determine: the properties of the rotating fluid (f , N_∞), the slope (α , z_0), and the tidal forcing (P_x , P_y). In addition, if the transport of suspended material is considered, the erosion parameter α_e , the critical shear-stress τ_c , and the sinking speed w_s appearing (3.8) and (3.9) have to be specified.

Most obvious is the choice of the Coriolis parameter ($f = 7.65 \times 10^{-5} \text{ s}^{-1}$) and the bottom slope ($\alpha = 3 \times 10^{-4}$), which can be determined without further assumptions from the local latitude and the echo sounding data obtained during the cruise, respectively (see above). As the bottom roughness is not well constrained, we chose a standard value here ($z_0 = 0.001 \text{ m}$), and discuss the sensitivity of our results with respect to this parameter in Appendix B.

The determination of the time-dependent forcing functions $P_x(t)$ and $P_y(t)$ is based on the following considerations. Firstly, we require a purely monochromatic forcing as in (3.11) in order to allow the model to reach periodic conditions after an appropriate spin-up period to be able to compute well-defined tidal averages. Secondly, in view of the idealized nature of our model, we will focus on forcing functions that are as simple as possible but still sufficient to mirror all key features of the observed BBL dynamics.

With this rationale in mind, and recalling that the M_2 tide largely determines the observed velocity variance at our study site, we computed the forcing functions based on the amplitude and phase of a pure M_2 tide with period $T_{M_2} = 12.42 \text{ h}$. Also, as discussed above in the context of (3.14), the diurnal tidal components are close to the critical period, $T_c = 22.7 \text{ h}$, which is likely to induce unphysical resonance effects in the modeled BBL.

We thus fitted a sinusoidal M_2 signal to the highpass-filtered velocity data shown in Fig. 3.4b, using the standard least-squares fitting procedure described in Emery and Thomson [2001], however, with the following difference: the axes ratio of the tidal ellipse was kept fixed at the value ω/f for consistency with the model solution

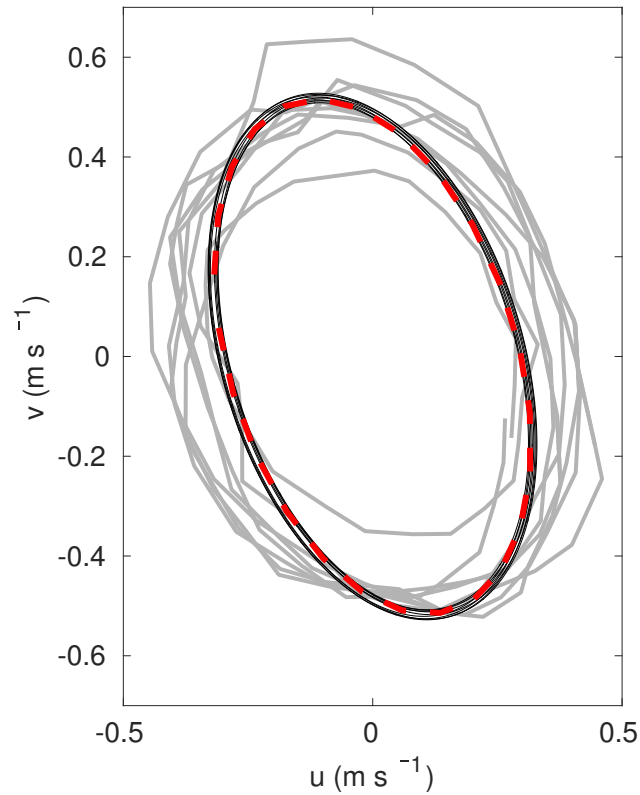


Figure 3.7.: Highpass-filtered M_2 tidal currents at 30 m depth (light gray) and modeled velocities in the region above the BBL (black lines). The dashed red line indicates a fit to the data based on a tidal ellipse with prescribed axes ratio ω/f .

in (3.12). This modified fitting procedure yields a tidal ellipse with a velocity amplitude of 0.53 m s^{-1} along the major axis, which is rotated at an angle of 107 degrees counter-clockwise with respect to the along slope direction (see Fig. 3.7). The analytical solution is seen to slightly overestimate the observed ellipticity but provides otherwise a good representation of the data. It is worth noting that orientation and tidal amplitude are also consistent with the M_2 tidal ellipse found by Xianwen et al. [2001] near this position.

In the next step, we computed amplitude and phase of the pressure function P_n defined in (3.11) by inverting (3.12), using the observed velocity amplitude. Projecting the result onto the x - and y -directions finally yields the required pressure functions $P_x(t)$ and $P_y(t)$. As shown above, fully periodic model solutions for this type of pressure forcing correspond to the tidal ellipse described by (3.12) in the non-turbulent model region above the BBL. However, numerical tests have shown that transients (mainly inertial oscillations) generated during the abrupt start of the simulations do not decay in this region due to the lack of any physical damping mechanism. The

problem can be strongly reduced (but not fully eliminated) by linearly increasing the periodic pressure forcing from zero to full amplitude over a period of 10 days. After a spin-up period of additional 40 days, the solutions become fully periodic inside the BBL (where transients quickly decay as a result of viscous damping) and nearly periodic in the undamped region above the BBL (see Fig. 3.7). As we are only interested in the processes inside the BBL, small deviations from perfect periodicity above the BBL are of no consequence for the following analyses.

Finally, the relevant background stratification N_∞ can be conveniently computed from the cross-slope buoyancy gradient $\partial b/\partial x$, using the projection relation in (3.2). Here, we estimate $\partial b/\partial x$ following Endoh et al. [2016], who noted that buoyancy fluctuations inside the nearly well-mixed BBL are largely determined by up- and down-slope advection. Thus, for this purpose, the buoyancy equation in (3.5) can be approximated as

$$\frac{\partial b}{\partial t} = -u \frac{\partial b}{\partial x}, \quad (3.16)$$

assuming that $\partial b/\partial x$ is constant.

Similar to Endoh et al. [2016], we find that $\partial b/\partial x = 2 \times 10^{-7} \text{ s}^{-2}$ largely explains the observed buoyancy fluctuations due cross-slope tidal motions (see below). According to (3.2), for the observed bottom slope, this value yields $N_\infty^2 \approx 7 \times 10^{-4} \text{ s}^{-2}$, slightly smaller than the measured vertical stratification above the BBL (Fig. 3.5d) but of the correct order of magnitude. As pointed out by Endoh et al. [2016], the relevant interior stratification for slope-induced tidal straining is that *adjacent* to the BBL (i.e., in the interior region located at the same depth level as the BBL at position S) rather than *above* the BBL. It is likely that the real interior stratification adjacent to the BBL, rather than being vertically homogeneous as assumed in our model, slightly decays with depth away from the thermocline region.

3.5. Modeling slope-induced tidal straining

Using the periodic tidal forcing described in section 3.2.3, and the model parameters in Tab.3.1, we investigate in the following to which extent our idealized model is able to reproduce the features of the observed BBLs. For easier comparison between field data (Fig. 3.6) and model results (Fig. 3.8), time axes have been aligned to reproduce

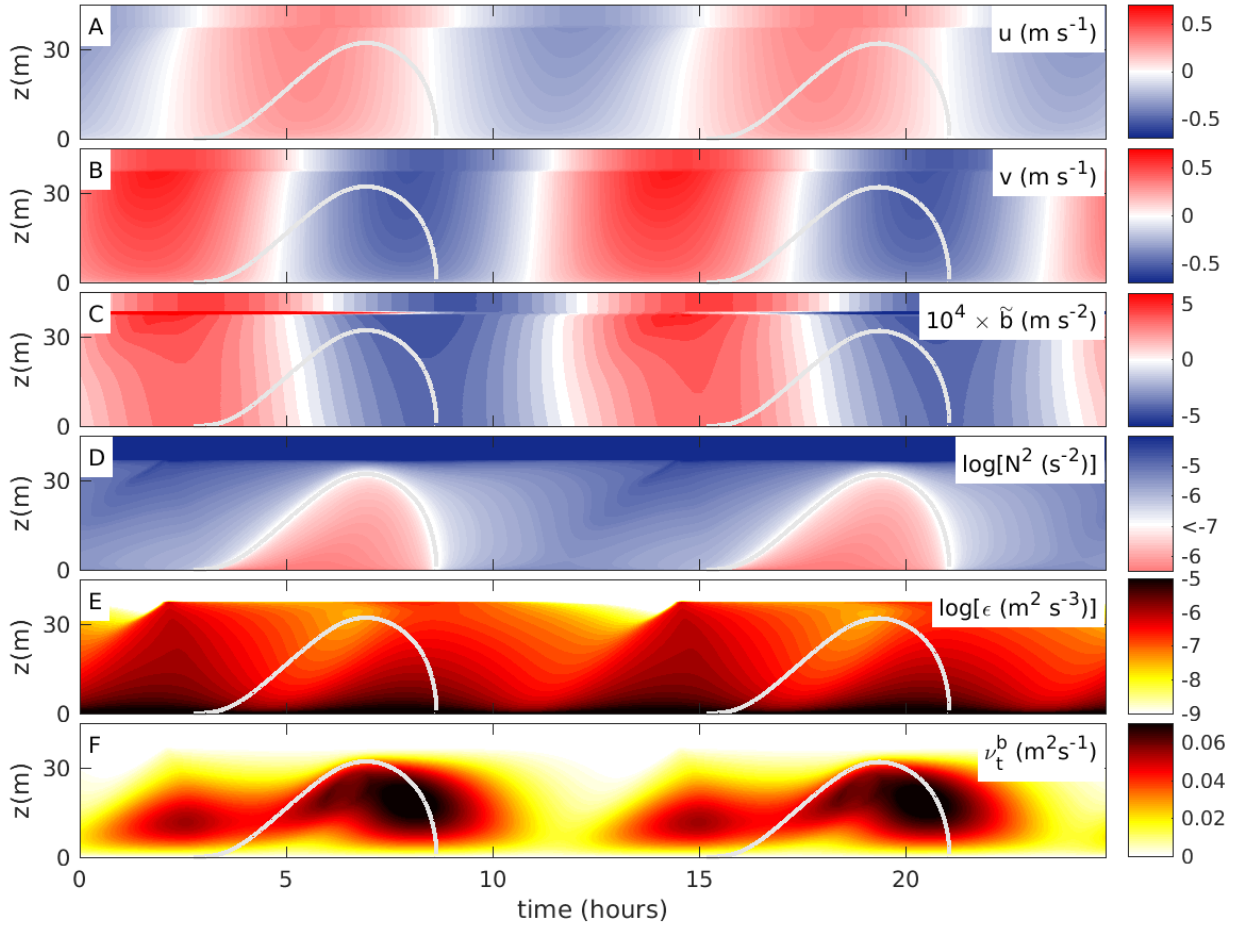


Figure 3.8.: Evolution of modeled (a) cross-slope velocity, (b) along-slope velocity, (c) buoyancy fluctuations, (d) buoyancy frequency, (e) turbulence dissipation rate, and (f) turbulent diffusivity. Gravitationally unstable regions are indicated by gray lines in all panels. Axes ranges, color scales, and time axis are identical to those used in Fig. 3.6.

the correct phase relationships in the M_2 tidal currents after the model has become periodically stationary. Due to their periodic nature, model results are only shown for two tidal periods for clarity.

The modeled velocities (Fig. 3.8a,b) mirror the observed M_2 tidal variability with good accuracy but do not exhibit the observed diurnal modulation, which is obviously a consequence of neglecting the diurnal tidal constituents in our simulations. As explained above, the diurnal signal is significant but not essential for the process studied here. Similar to the observations, also the model results show clear indications for a frictional reduction of the velocities towards the bottom, which is an essential requirement for the development of SIPS.

Also the magnitude and phase of the tidal buoyancy fluctuations shown in Fig. 3.8c are in good agreement with the data, supporting the idea that the variability in buoyancy is largely a result of cross-slope advection as discussed above. The strong diurnal modulation of the buoyancy fluctuations in the upper part of the BBL found in the observations is, however, not represented by the model, as diurnal tides are ignored in our simulations.

While the good agreement between model and data regarding the tidal velocity and buoyancy fluctuations is largely a result of the selected forcing variables and model parameters, the correct prediction of BBL stratification provides a much more stringent test of the model performance. Fig. 3.8d shows that the model provides an excellent representation of the evolution of BBL stratification in at least two important aspects. First, the predicted BBL thickness is approximately 37 m, and therefore well inside the observational range (see Fig. 3.6d). In view of the complex interplay between slope-induced re-stratification and mixing that determines the BBL thickness, this is a remarkable result. Second, the model is also able to reproduce the periodic generation and destruction of stratification (SIPS) inside the BBL, in particular regarding the occurrence of gravitationally unstable layers during periods of upslope flow. The observed and modeled unstable layers have a similar vertical extent and timing but, different from the model, the observations also exhibit a strong diurnal modulation of stratification that leads to a suppression of the convective layer thickness during every second instance of their occurrence (e.g., at $t \approx 20$ h in Fig. 3.6d), which cannot be reproduced in the model, of course, again because diurnal tides are ignored.

As pointed out above, the imprint of this diurnal modulation in stratification is also clearly visible in the observed dissipation rates (Fig. 3.6e) but, for the reasons described above, cannot be reproduced by the model. The model does, however, correctly predict the strong increase of the dissipation rates towards the bottom, and the correct order of magnitude of dissipation at the beginning and end of observation period (Fig. 3.8e). Modeled dissipation rates show a M_4 periodicity with a M_2 modulation that reflects the ellipticity of the tidal currents: largest dissipation rates are found at peaks of the v -component, which dominates the M_2 tidal motions (see above).

While the variability in the modeled dissipation rates is therefore mainly driven by variations in tidal forcing, the eddy diffusivities shown in Fig. 3.8f are also strongly affected by variations in stratification associated with SIPS. Although peaks in dissipation rate and eddy diffusivity approximately coincide, the latter shows a much stronger tidal asymmetry: largest diffusivities are found during periods of upslope flow, when

slope-induced tidal straining reduces vertical stratification, or even causes regions with negative N^2 . We will see in the following that this modulation of the eddy diffusivity is essential for the generation of residual transports.

3.6. Dynamics of suspended material

One of the most important implications of tidal straining is the generation of residual currents and residual transports of dissolved substances and suspended material. Endoh et al. [2016] speculated that this process may also play an essential role for the transport of suspended material at their study site in the East China Sea. Although their turbidity measurements (see their Fig. 2i) clearly show strongly enhanced concentrations of suspended material inside the BBL, their data were too limited to draw any definite conclusions about residual SPM transports. In the following, we therefore discuss a number of idealized simulations to clarify the mechanisms and potential implications of slope-induced tidal straining for the residual transport of suspended material.

3.6.1. Temporal variability

Our simulations are based on the SPM transport equation in (3.8) and the simple erosion model in (3.9). Lacking information about sediment properties at the study site, we vary the sinking speed, identified by Schulz and Umlauf [2016] as the key parameter determining the transport of suspended material, over a broad range of values. For the critical shear stress, τ_c , and the erosion parameter, α_e , shown to be of only secondary importance by Schulz and Umlauf [2016], we adopt the standard values suggested by these authors (see Tab. 3.1).

Fig. 3.9c,d reveals for two different sinking speeds that maxima in the SPM concentrations follow maxima in the turbulence diffusivities with a small phase shift, which mirrors the time required to mix eroded material up into the BBL. Concentration maxima are found when the cross-slope velocity u is close to zero (Fig. 3.9a), or, likewise, when the magnitude of the more energetic along-slope flow component v attains maximum values (Fig. 3.8b). Tidal asymmetries resulting from the modulation of the turbulent diffusivity due to SIPS are clearly evident in both local and vertically integrated SPM concentrations (Fig. 3.9c-e). For large sinking speeds (Fig. 3.9c), highest

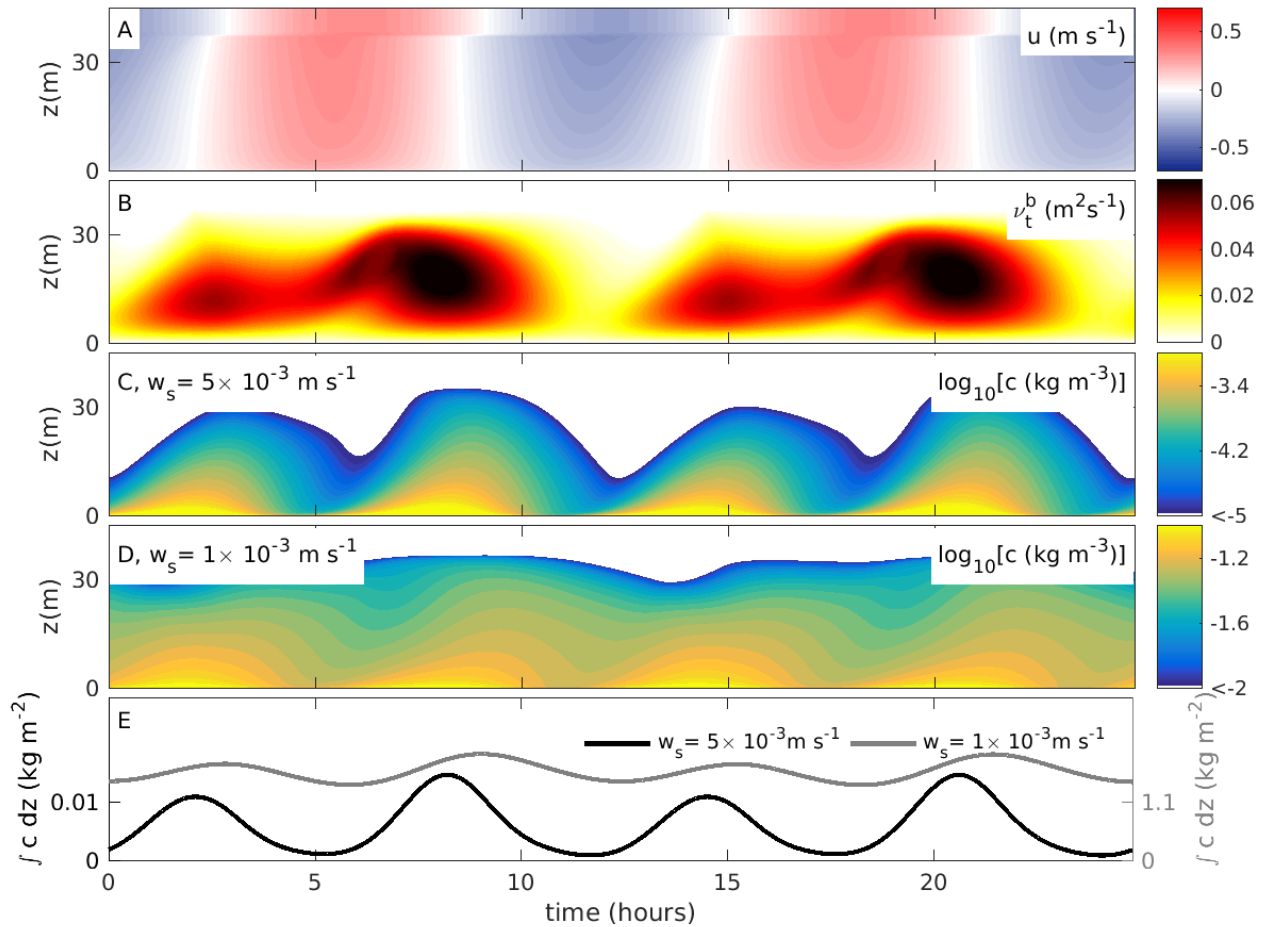


Figure 3.9.: Evolution of (a) cross-slope velocity, (b) turbulent diffusivity, and (c,d) SPM concentrations for two different settling velocities: $w_s = 5 \times 10^{-3}$ m s⁻¹ and $w_s = 1 \times 10^{-3}$ m s⁻¹. Panel (e) shows the corresponding integrated SPM concentrations. Panels (a) and (b) are re-drawn from Fig. 3.8a,f for better orientation.

concentrations are found at the end of the period with upslope flow, when turbulent diffusivities are maximum, along-slope velocities close to their maximum negative values ($v < 0$), and cross-slope velocities close to zero. Similar SPM maxima are also found at the end of downslope flow period, however, with significantly smaller concentrations due to the comparably smaller turbulent diffusivities.

The strong correlation between high SPM concentrations and negative along-slope speeds constitutes a tidal pumping mechanism that, as discussed in more detail below, leads to a vigorous residual transport of suspended material along the slope in the negative y -direction. Tidal pumping is much less effective in the cross-slope x -direction because SPM concentration maxima are associated with minima in the magnitude of the cross-slope velocity ($u \approx 0$). Although tidal asymmetries in SPM concentrations

can also be discerned for the case with low sinking speeds (Fig. 3.9d,e), they are less pronounced, and their potential to trigger tidal pumping is therefore expected to be weaker.

Finally, it is worth noting that the collapse of cross-slope tidal pumping mentioned above is qualitatively different from the non-rotating case investigated by Schulz and Umlauf [2016]. Although their simulations showed similar tidal asymmetries with highest turbulent diffusivities and SPM concentrations observed during periods of upslope flow, these maxima occurred earlier compared to the rotating case. This is easily understood from the fact that in the non-rotating case the v -component, dominating BBL turbulence in our case, is lacking, and highest diffusivities are thus observed significantly before the upslope flow reversal. In the non-rotating case, high SPM concentrations are therefore correlated with significant upslope velocities ($u > 0$), resulting in an effective upslope pumping of suspended material.

3.6.2. Residual transports

The residual transports of suspended material in the cross-slope and along-slope directions are defined as

$$F_x = \langle uc \rangle - \langle c \rangle w_s \sin \alpha, \quad F_y = \langle vc \rangle, \quad (3.17)$$

where the angular brackets denote the tidal average. The second term in the cross-slope flux F_x represents the small downslope motion of vertically sinking material near a sloping bottom. Schulz and Umlauf [2016] showed that this term is generally negligible for small slopes ($\alpha \ll 1$), and therefore will be ignored in the following.

Schulz and Umlauf [2016] also pointed out that the fluxes defined in (3.17) are of limited use for the analysis of the tidal transport mechanisms due to their direct dependency on the SPM concentrations. Instead, they suggested to normalize the SPM fluxes with the concentrations, which removes this dependency:

$$\begin{aligned} u_c &= \frac{\langle uc \rangle}{\langle c \rangle} = \langle u \rangle + \frac{\langle \tilde{u}\tilde{c} \rangle}{\langle c \rangle}, \\ v_c &= \frac{\langle vc \rangle}{\langle c \rangle} = \langle v \rangle + \frac{\langle \tilde{v}\tilde{c} \rangle}{\langle c \rangle}. \end{aligned} \quad (3.18)$$

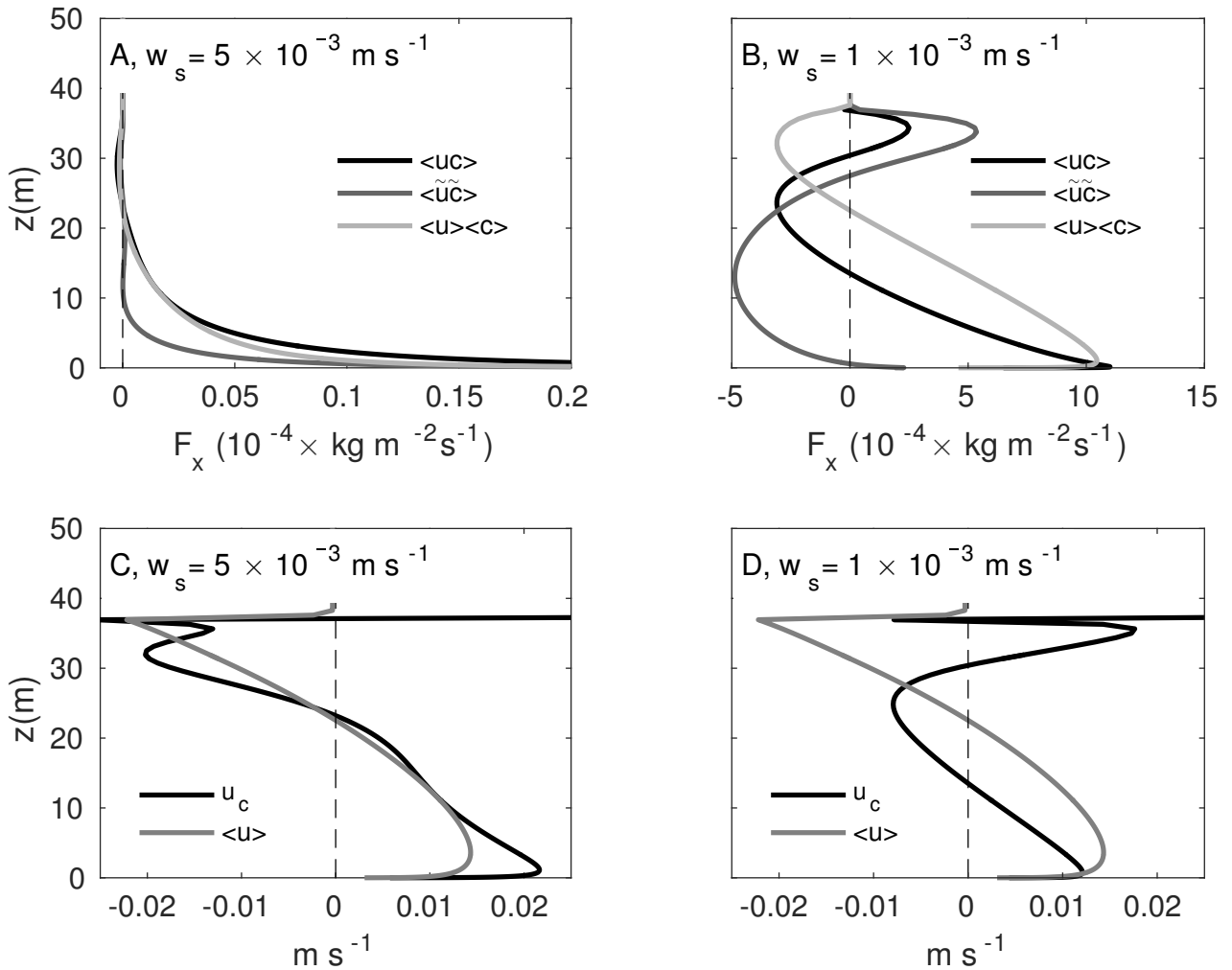


Figure 3.10.: Residual cross-slope fluxes of suspended material for settling velocities (a) $w_s = 5 \times 10^{-3} \text{ m s}^{-1}$ and (b) $w_s = 1 \times 10^{-3} \text{ m s}^{-1}$ with contributions from the residual currents and tidal pumping as indicated. Panels (c) and (d) show the corresponding effective transport velocities defined in (3.18). Note the different axes ranges.

The normalized velocities u_c and v_c are recognized as the effective velocities at which SPM is transported across and along the slope during a tidal cycle. In the second step in (3.18), we have further decomposed all quantities into tidal averages and fluctuations (denoted by the tilde), revealing that the transport velocities are the sum of the residual velocities and correlation terms representing the effect of tidal pumping.

Figs. 3.10 and 3.11 compare cross-slope and along-slope SPM fluxes for the two sinking speeds shown in Fig. 3.9c,d. As already speculated in section 3.6.1, for the larger sinking speed the contribution of tidal pumping to the total cross-slope flux is small due to the fact that high SPM concentrations generally co-occur with negligible

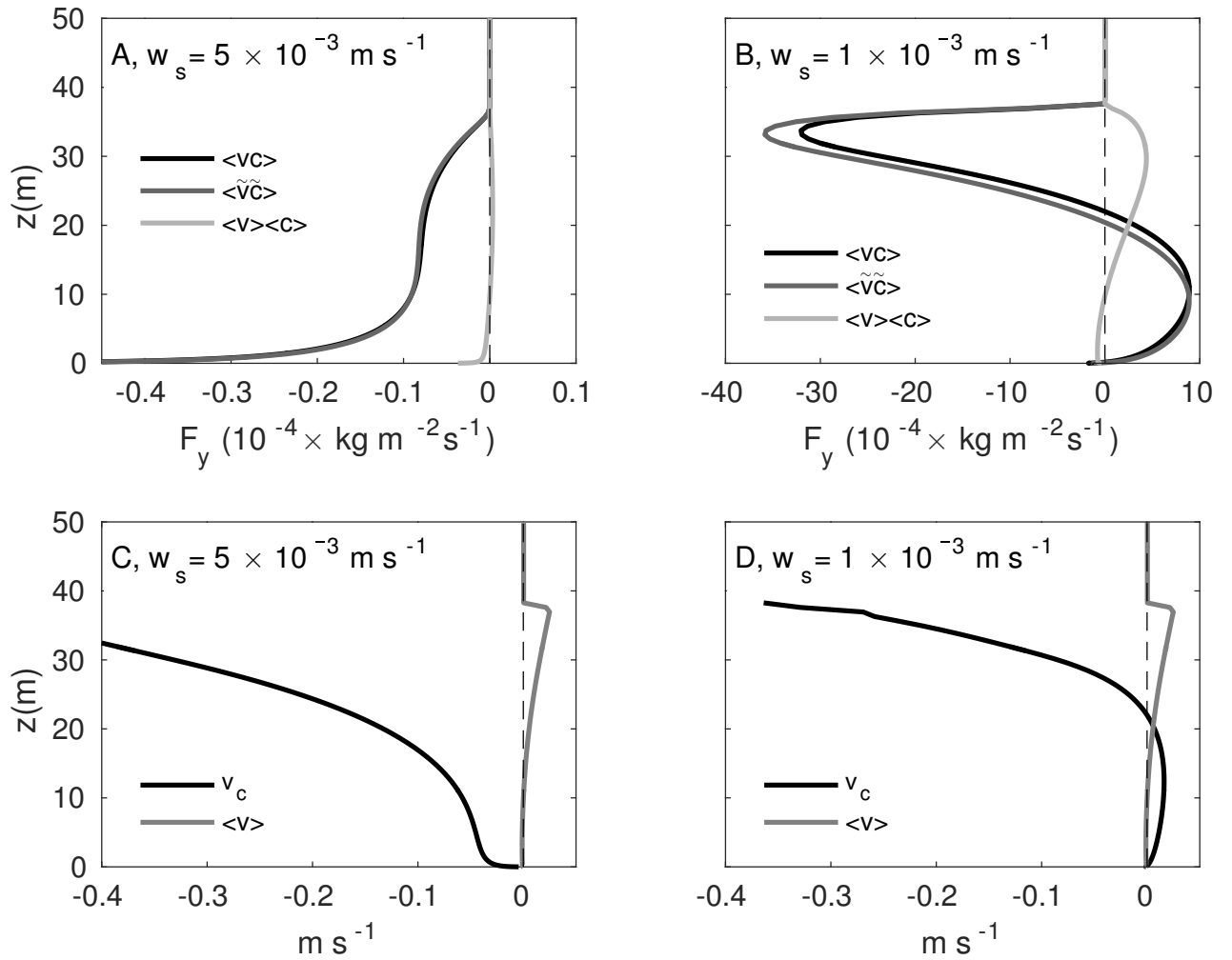


Figure 3.11.: As in Fig. 3.10, but now for the along-slope SPM fluxes and transport velocities. Note that the axes ranges are different from Fig. 3.10.

cross-slope speeds (Fig. 3.10a). This is confirmed by Fig. 3.10c, showing that the transport velocity u_c is of the same order of magnitude as the residual current $\langle u \rangle$. Different from the non-rotating case investigated by Schulz and Umlauf [2016], tidal pumping is therefore not the dominating process in this example. This is also true for the case with a small sinking speed (Fig. 3.10b,d), which is, however, further complicated by the fact that the contributions of the residual current and tidal pumping may point into different directions.

The situation changes completely if the along-slope fluxes are considered. Fig. 3.11a,b shows that for both sinking speeds tidal pumping provides the overwhelming contribution to the net SPM fluxes. The strong correlation between large SPM concentrations and negative along-slope velocities for the case with a large sinking speed (see

section 3.6.1) induces a residual flux of suspended material in the negative y -direction that is almost one order of magnitude larger than the corresponding cross-slope flux (Fig. 3.10a). The effectiveness of tidal pumping in this case is corroborated by Fig. 3.11c, showing that the contribution of the residual current to the effective transport velocity v_c is generally negligible. Typical transport velocities in the lower part of the BBL, where SPM concentrations are high, are of the order of 0.1 m s^{-1} , suggesting that suspended material is transported approximately 5 km along the slope during one tidal cycle.

Particularly notable is the two-layer structure determining the along-slope SPM transport for the case with a low sinking speed (Fig. 3.11b), which may be explained as follows. Comparing the along-slope velocities in Fig. 3.8b and the SPM concentrations in Fig. 3.9d shows that during periods of positive along-slope flow, near-bottom SPM concentrations are highest because stable stratification prevents resuspended material to be diluted by mixing across a larger fraction of the BBL. The opposite is the case for periods with negative along-slope flow. Here, SPM is mixed up high into the BBL, because mixing is not suppressed by stable stratification any more. The net effect of the resulting correlations is a positive along-slope transport near the bottom, and a negative transport in the upper part of the BBL.

3.6.3. Variable sinking speed and stratification

To quantify the variability of SPM transport across a larger parameter space, it is useful to introduce the normalized integrated fluxes,

$$U_c = \frac{\int \langle uc \rangle dz}{\int \langle c \rangle dz}, \quad V_c = \frac{\int \langle vc \rangle dz}{\int \langle c \rangle dz}. \quad (3.19)$$

Analogous to the vertically variable transport velocities u_c and v_c , the vertically integrated expressions in (3.19) define bulk measures for the residual velocities at which SPM is transported across and along the slope, respectively [Schulz and Umlauf 2016].

In Fig. 3.12, the distribution of U_c and V_c for varying settling velocities is displayed. As already discussed in section 3.6.2, the cross-slope sediment flux is largely determined by the contribution of the residual current, $\langle u \rangle \langle c \rangle$, which is directed upslope near the bottom and downslope in the upper part of the BBL. The contribution of tidal pumping is either relatively small (for large sinking speeds, see Fig. 3.10a,c), or

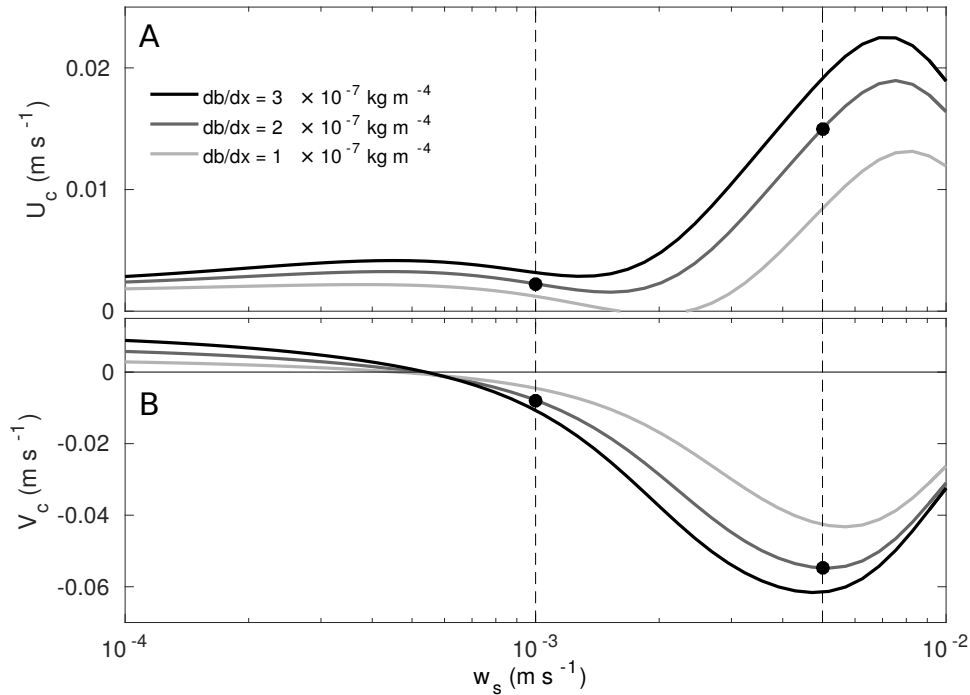


Figure 3.12.: Distribution of (a) cross-slope and (b) along-slope transport velocities, U_c and V_c , for variable settling velocities and cross-slope buoyancy gradients (all other parameters as in Tab. 3.1). Dashed vertical lines indicate the standard cases of small and large settling velocities discussed in the context of Fig. 3.9.

even counteracts the contribution of the residual current (for small sinking speeds, see Fig. 3.10b,d). The local maximum in U_c for $w_s \approx 7 \times 10^{-3} \text{ m s}^{-1}$ (Fig. 3.12a) can thus be explained as follows. For settling velocities higher than this optimal value, suspended matter remains inside a thin near-bottom layer, where flow velocities are strongly reduced due to frictional effects. SPM transport is not efficient in this case. Material that exhibits settling velocities smaller than the optimal value is more homogeneously distributed across the BBL, implying that the near-bottom upslope transport is partly compensated by a downslope transport in the upper part of the BBL. The local minimum, visible Fig. 3.12a for sinking speeds slightly larger than $w_s = 10^{-3} \text{ m s}^{-1}$, originates from the effect of tidal pumping, opposing the contribution of the residual current for material with small settling velocities (see Fig. 3.10b). It is remarkable that for virtually all settling velocities investigated here, the transport is directed upslope, similar to the non-rotating case studied by Schulz and Umlauf [2016].

Different from the cross-slope transport of suspended material, the along-slope transport is mainly determined by tidal pumping (Fig. 3.11). In this case, V_c reaches a local minimum (maximum negative transport rates) near $w_s \approx 5 \times 10^{-3} \text{ m s}^{-1}$. This

optimum value is also marked in Fig. 3.12, and corresponds to the case of large sinking speed discussed in the previous sections. The maximum in the transport rate for this value of the sinking speed is shaped by two competing effects. For settling velocities larger than the optimum value, suspended material is largely located inside the thin frictional near-bottom layer, where tidal pumping is not effective and V_c thus decreases. For material sinking slower than the optimal value, the negative near-bottom transport is partly compensated by an opposing transport in the upper part of the BBL (see example in Fig. 3.12b). If sinking speeds are small enough, this effect may even cause a reversal of the transport direction (Fig. 3.12b). Comparing the magnitudes of U_c and V_c in Fig. 3.12, it is evident that along-slope tidal pumping results in a factor of 2-3 larger transport velocities compared to the cross-slope direction.

Finally, it is worth noting that Fig. 3.12 also reveals that stronger background stratification enhances the SPM transport mechanisms in both the cross-slope and along-slope directions. This is little surprising, however, as stratification is one of the prerequisites for slope-induced tidal straining and pumping. The existence of an optimal settling velocity for up-slope transport, and the observed dependency on background stratification, are in agreement with the findings of Schulz and Umlauf [2016] for the non-rotating case.

3.6.4. Rotational effects

According to (3.12) and (3.13), the shape of the tidal ellipse is determined by the Coriolis parameter, which is therefore likely to have an important impact on tidal straining and SPM transport. In the following, we investigate this effect in a series of simulations with varying latitude (varying Coriolis parameter), leaving all other parameters as in Tab. 3.1. For the sinking speed, we assume $w_s = 5 \times 10^{-4} \text{ m s}^{-1}$, corresponding to the optimal value for along-slope tidal pumping identified in the previous section.

We consider two special cases for the pressure forcing in (3.11). In the first case, we assume that the pressure force is directed exactly in the cross-slope direction ($P_x \neq 0$, $P_y = 0$), whereas in the second case the forcing is purely along-slope ($P_x = 0$, $P_y \neq 0$). Using the analytical solution in (3.12), we adjust the pressure force P for each case exactly such that the velocity amplitude in the direction of the forcing remains constant at a value of 0.5 m s^{-1} . This results in a tidal ellipse with the (constant) major axes

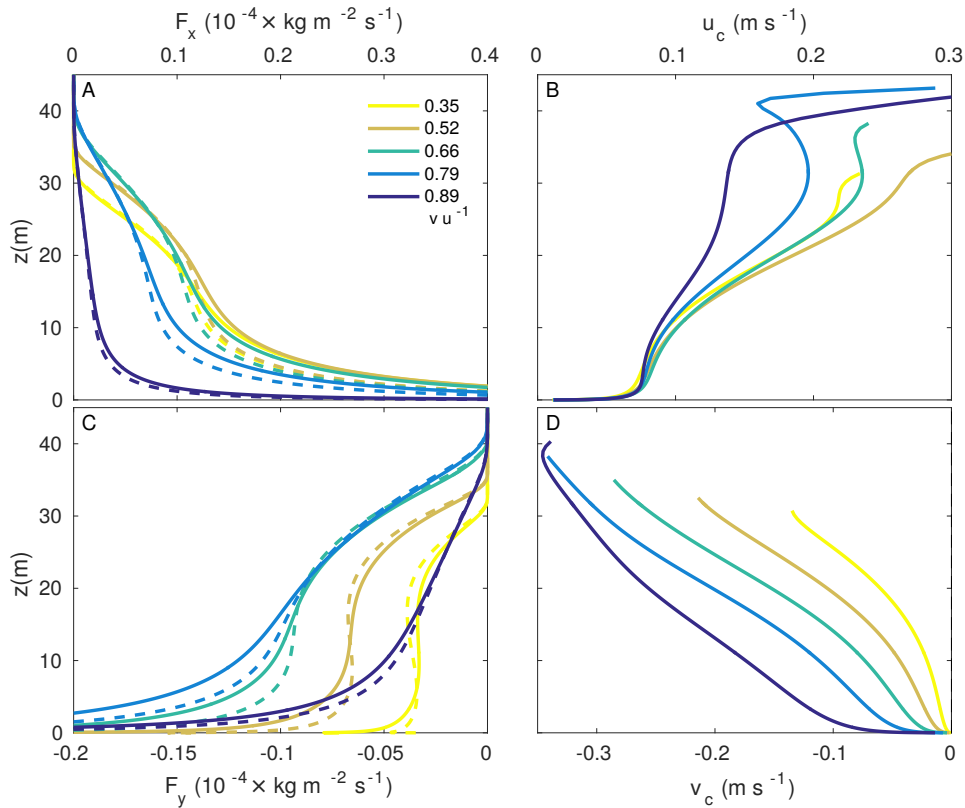


Figure 3.13.: Profiles of (a) cross-slope and (c) along-slope SPM flux, and (b) cross-slope and (d) along-slope transport velocity for a range of latitudes between 20° N and 60° N (at 10° intervals). The pressure forcing is purely cross-slope ($P_y = 0$), and the amplitude of the cross-slope tidal velocity fluctuations in the region above the BBL is $u = 0.5 \text{ m s}^{-1}$ for all cases. The amplitude of the corresponding along-slope component v increases with latitude as indicated. Dashed lines in (a) and (c) show the contribution of tidal pumping to the overall SPM flux.

oriented parallel to the pressure force (i.e., either cross-slope or along-slope), and the minor axes increasing in magnitude with increasing Coriolis parameter. The latter is varied by changing the latitude from 20° N to 60° N at 10° intervals, corresponding to axes ratios between 0.35 and 0.89 for the tidal ellipses. Using (3.14), it is easy to show that for the parameters in Tab. 3.1, BBL resonance and the transition to super-critical slopes [see Schulz and Umlauf 2016] occur at a latitude of approximately 75° N. The range of latitudes used here guarantees that BBL resonance does not affect the results.

The case with pure cross-slope forcing ($P_y = 0$) includes the non-rotational case ($f = 0$, $v = 0$) investigated in detail by Schulz and Umlauf [2016]. As pointed out by these authors, the turbulent diffusivities show in this case a clear M_4 signal that exhibits a M_2 modulation due to SIPS (higher diffusivities are observed during periods with upslope flow). These tidal asymmetries trigger an efficient tidal pumping

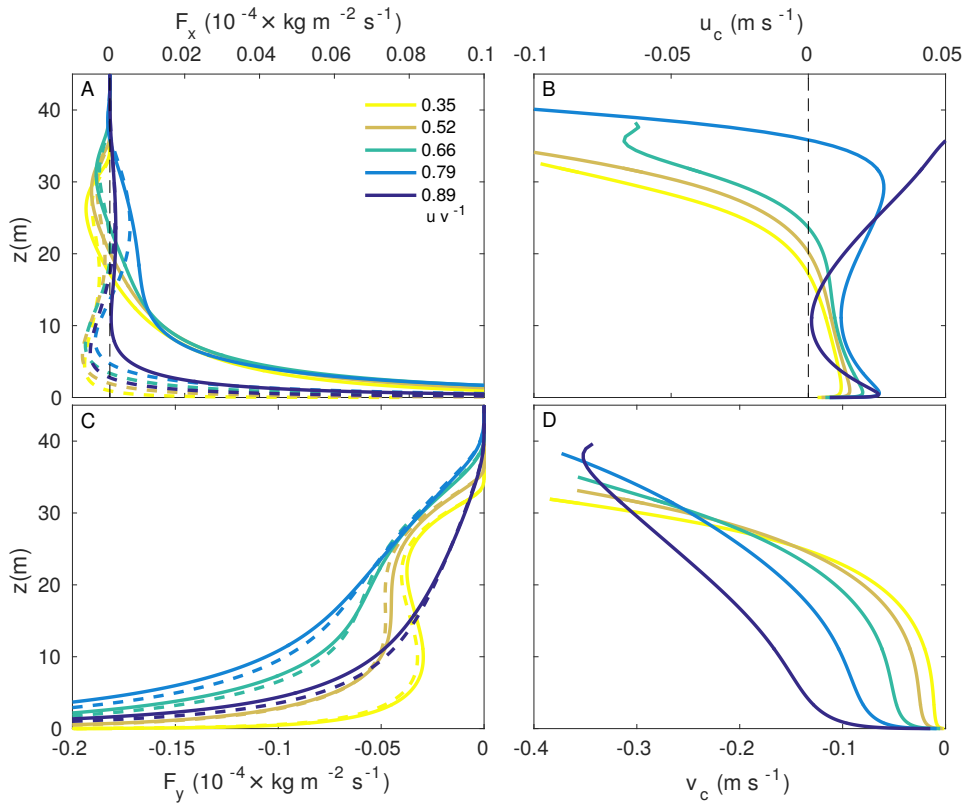


Figure 3.14.: As in Fig. 3.13, but now for along-slope pressure forcing ($P_x = 0$), and constant amplitude of the along-slope tidal velocity fluctuations ($v = 0.5 \text{ m s}^{-1}$).

mechanism that transports suspended material in the upslope direction. Fig. 3.13a,b shows that this mechanism remains essentially unchanged for latitudes up to approximately 40° N , corresponding to a axis ratio of 0.66 for the tidal ellipse. While the BBL thickness significantly increases over this range of latitudes, SPM fluxes and transport velocities exhibit only small changes in the lowest 20 m of the BBL, where most of the suspended material is located and therefore most of the transport occurs. Quite differently, the along-slope SPM transport, vanishing for $f = 0$, quickly increases for $f > 0$ as a result of the same tidal pumping mechanisms described in detail in sections 3.6.1 and 3.6.2 (see Fig. 3.13c,d).

For higher latitudes, the tidal ellipses gradually approach a circular shape, implying that the magnitude of the rotating velocity vector changes only slightly during a tidal cycle. As consequence, the turbulent diffusivity and the bottom stress (both important for SPM erosion) show a transition from a pronounced M_4 variability with two maxima during a tidal cycle towards a weak M_2 modulation with a single maximum during periods with upslope flow. Considerably less material is eroded during this single maximum compared to the cases with smaller rotation rates, and SPM concentrations

strongly decrease. Therefore, although tidal pumping is still active or even increasing in the along-slope direction (see Fig. 3.13d), the total SPM fluxes collapse for high latitudes (Fig. 3.13a,c).

In our second series of simulations, we assume that the tidal pressure force is directed exactly along the slope ($P_x = 0$). Different from the case with cross-slope forcing, both the cross-slope and the along-slope SPM fluxes vanish in the limit $f \rightarrow 0$ for symmetry reasons. For increasing latitudes, a weak upslope transport develops, which, similar to the example in section 3.6.2, is driven by the residual flow rather than by tidal pumping (Fig. 3.14a,b). The weak transport rates in the cross-slope direction are strongly contrasted by the vigorous along-slope tidal pumping mechanism that quickly develops for increasing f (Fig. 3.14c,d). The mechanisms are analogous to the example discussed in the previous sections (see Fig. 3.11a,c), which was also characterized by a dominant along-slope flow component. For the highest latitudes, however, both the cross-slope and along-slope transports collapse again due to decreasing concentrations of suspended material. The reasons are identical to those discussed above.

3.7. Conclusions

Two main conclusions can be drawn from the first part of our study, which showed that an idealized one-dimensional numerical model is able to reproduce the most important features in a dataset describing tidal straining on a sloping shelf in the East China Sea. First, the good agreement between model and data indicates that the model correctly represents the key physical processes determining slope-induced tidal straining; and secondly, our results let it seem unlikely that processes other than those represented in the model (e.g., classical tidal straining due to river runoff) explain the observed BBL variability at our study site. The combination of model results and experimental data therefore provides the first direct and conclusive evidence for the occurrence of slope-induced tidal straining at a real ocean site.

Our simulations also revealed a number of important processes related to the effect of rotation, which was ignored in previous studies of slope-induced tidal straining. For tidal ellipses oriented in the cross-isobath direction, the upslope transport of suspended material by tidal pumping, originally described by Schulz and Umlauf [2016] for the non-rotating case, was only slightly modified by rotational effects. However, the along-slope tidal velocity fluctuations induced by these rotational effects were shown

to trigger a new type of tidal pumping mechanism that efficiently transports suspended material along the slope. A comparable along-slope tidal pumping was also observed for tidal ellipses oriented with their main axes along isobaths. In both cases, tidal pumping was found to be most efficient for an optimal sinking speed that was of the order of $5 \times 10^{-4} \text{ m s}^{-1}$ in our example. For material sinking significantly slower or quicker than this value, the tidal pumping of suspended material was strongly reduced. Typical transport velocities deduced from our simulations suggest that suspended material may be transported over several kilometers along the slope during one tidal cycle.

Additional parameter studies have shown that the processes identified in this study are robust, and therefore likely to occur across a wide range of naturally occurring conditions. In contrast to classical tidal straining that relies on the existence of a freshwater source or differential heating, slope-induced tidal straining only requires: a slope, an oscillating tidal current, and a stratified water column. These pre-requisites are nearly ubiquitous in the ocean.

Chapter 4.

The Baltic Sea

In addition to the model investigations of tidal straining and sediment transport in the previous chapters, also several field campaigns were performed, focusing on the mechanisms of sediment transport in a non-tidal basin. These measurements were carried out in coastal areas of the Western Baltic Sea. Prior to the discussion of the data in the next chapter, an overview of the present hydrological conditions and the wave climate of the Baltic Sea is provided in the following. Additionally, the sedimentology of the Western Baltic Sea are briefly discussed, as the following chapter focuses on near-bottom dynamics and sediment transport.

4.1. Present hydrography and dynamics

The Baltic Sea has an extent of $4.2 \times 10^5 \text{ km}^2$ [Feistel et al. 2008] and is connected to the North Sea via the Danish Straits: the Øresund and the Great and Little Belt together with the Fehmarn Belt. The climate is humid: Annual precipitation adds around 224 km^3 of water to the Baltic Sea, evaporation amounts to only 184 km^3 . Rivers discharge a total of 436 km^3 water per year [Reissmann et al. 2009]. An exchange flow takes place, where brackish water leaves the Baltic Sea near the surface (annually around 947 km^3) and saline North Sea water enters at the bottom (nearly 500 km^3 per year on average, but frequency and strength of inflow events differ dramatically over time, highly dependent on short-term weather conditions). The saline and oxic waters intruding from the North Sea are the only source of oxygen for the deeper parts of the Baltic Sea. Inflows occur in two different ways. Baroclinic inflows are triggered by the horizontal salinity gradient between North and Baltic Sea and occur at calm wind

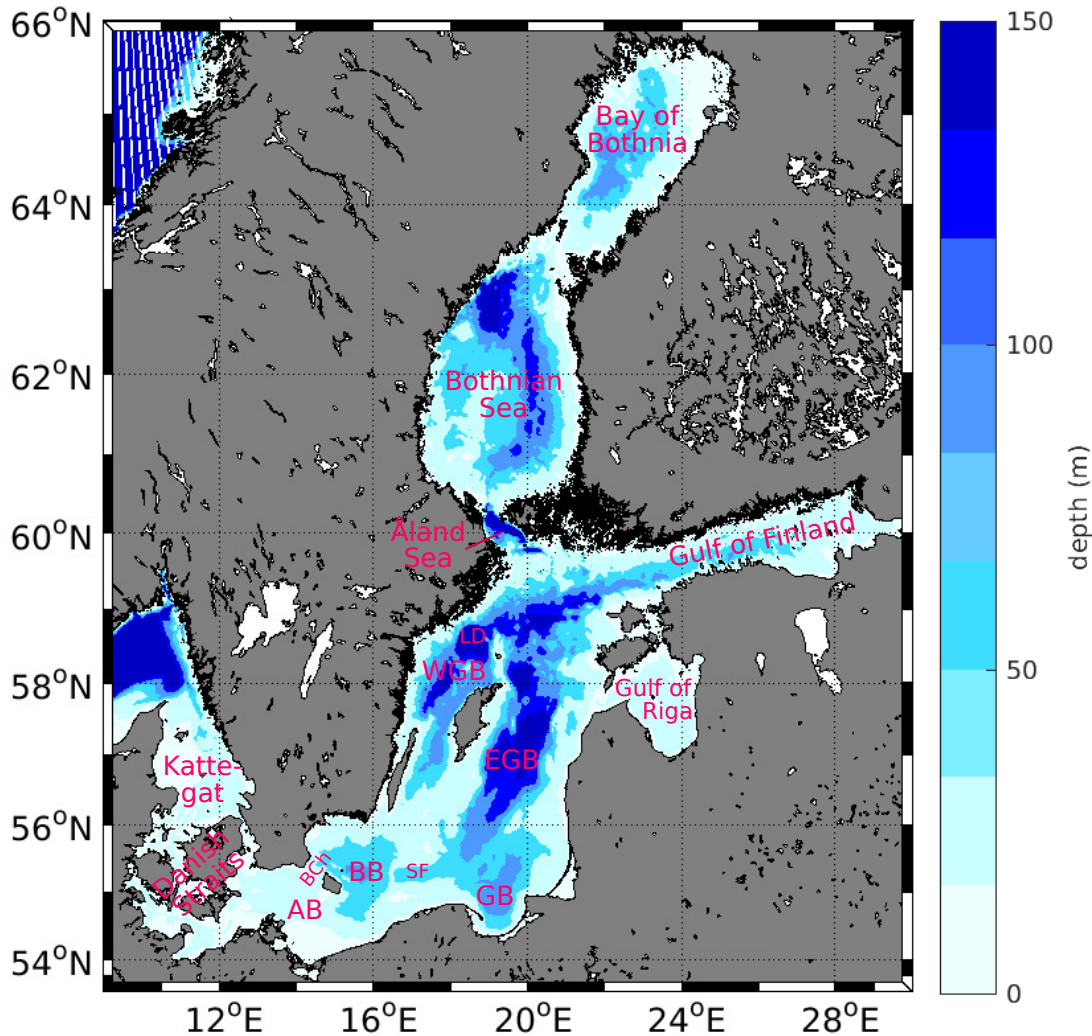


Figure 4.1.: Topographic map of the Baltic Sea. Abbreviations stand for Arkona Basin (AB), Bornholm Channel (BCh), Bornholm Basin (BB), Słupsk Furrow (SF), Gdańsk Basin (GB), Eastern Gotland Basin (EGB), Landsort Deep (LD) and Western Gotland Basin (WGB).

conditions, mostly in summer [Reissmann et al. 2009]. The main contribution to the ventilation of the deep basins is, however, provided by the barotropic inflow events, called Major Baltic Inflows (MBIs). Those MBIs occur irregularly and are caused by special meteorological conditions: Firstly, high air pressure over the Baltic Sea region and strong winds in westerly directions cause the mean sea level in the Baltic Sea to drop by up to 50 cm, imposing a gradient in sea level elevation between the Kattegat

and the Arkona Basin. Secondly, several weeks of wind in easterly directions with strong gales [Feistel et al. 2008; Reissmann et al. 2009; Mohrholz et al. 2015] push saline and oxygen rich water into the Baltic Sea. These conditions occur primarily between October and February.

Two shallow sills, the Drøgden Sill (7 m deep, values in brackets refer to the local depth in the following) and the Darss Sill (18 m) form the passage to the first of several basins, the Arkona Basin (45 m), through which the North Sea water propagates as a deep gravity current (see Fig. 4.1). Through the Bornholm Channel, the Arkona Basin is connected to the Bornholm Basin (80 m), from where the bottom current flows over the Słupsk Sill (60 m) and through the approximately 80 km long Słupsk Furrow (90 m) southeast into the Gdańsk Basin (110 m) and northeast into the Eastern Gotland Basin (250 m). From there, the deep current can enter the easterly Gulf of Riga or the Western Gotland Basin, wherein the Landsort Deep (with 490 m the deepest point in the Baltic Sea) is located. The Gulf of Finland forms the eastern boundary of the Baltic Sea and north of the Gotland Basin, the Åland Sea separates the Baltic Proper in the south from the Bothnian Sea and the Bay of Bothnia in the north [Reissmann et al. 2009]. Salt water entering at the Darss Sill needs approximately 2–6 months to exchange the bottom water in the Gotland Basin [Feistel et al. 2008].

The bathymetry of the Baltic Basin and the narrow connection to the open ocean via the Danish Straits lead to several notable features in the hydrographic conditions: Dense bottom water from the North Sea creates a permanent strong halocline that separates bottom from surface waters, preventing the ventilation of the water masses in the deep basins. Oxygen that enters through exchange with the atmosphere is not mixed below the halocline, leaving inflowing North Sea water as the only significant supply of oxygen. Large parts of the Baltic Sea become anoxic after long periods without large salt water inflows, with severe implications for the geochemical processes and the ecosystem of both the lower part of the water column and the sediment-water interface.

Furthermore, a salinity gradient is present across the Baltic Sea: The bottom current entrains with overlying brackish water along its pathway (for example, volume of the gravity current increases by 53 % when passing through the Arkona Basin, [see Reissmann et al. 2009]), and the slow entrainment of salty water into the overlying water mass forms a NE–SW surface salinity gradient. Surface salinity drops from around 18 g kg⁻¹ in the Danish Straits to 8 g kg⁻¹ in the Arkona Basin, down to 6–

7 g kg^{-1} in the Eastern Gotland Basin and even below 3 g kg^{-1} in the Bay of Bothnia and the Gulf of Finland [Feistel et al. 2008].

Besides the dense bottom currents originating from inflowing North Sea water, local wind forcing combined with the topographic structure and the permanent salinity stratification in the Baltic Sea triggers other flow features on smaller scales. Although tides do not play a significant role, other oscillatory currents are found in the Baltic Sea: near-inertial waves, internal seiching motions and topographic or coastal-trapped waves. In the absence of tides and due to the permanent deep-water stratification, inertial oscillations and low-mode near-inertial wave motions have been found to dominate the energetics on the basin-scale [Van der Lee and Umlauf 2011]. Near-inertial internal waves have periods close to the inertial period, which is $T_f = 14.8 \text{ h}$ in the southern part of the Baltic Sea (at a latitude of 54°N) down to $T_f = 13.1 \text{ h}$ in the northern part (66°N). Tide gauge records along the coast indicate that eigenoscillations play a major role in the Baltic Sea [Wubber and Krauss 1979]. Large-scale meteorological forcing initiates the development of seiches on several frequencies, depending on which parts of the Baltic act as oscillatory system. Another main energy source on basin-scale are topographic waves with periods of a few days, that are a direct response to enhanced wind forcing [Holtermann and Umlauf 2012], and low-frequency, quasigeostrophic, coastal-trapped motions forced by local wind [Pizarro and Shaffer 1998].

4.2. Wave climate

Another important factor for the dynamics in the Baltic Sea, especially in the context of sediment resuspension, are wind-generated waves. The impact of the wave-induced stress on the sediment generally dominates over the stress induced by the mean currents [Grant and Madsen 1986], if the water is shallow enough to allow wave energy to reach the sea floor. To map the wave activity spatially resolved in the whole Baltic Sea, a wave model was set up, verified and model results were analyzed. This is described in the following.

4.2.1. Wave model setup and verification

The SWAN wave model version 41.01 was set up for the Baltic Sea including a nesting in the south-western part that was a focal point for the sediment transport investigations described in the following chapter. For the whole Baltic Sea, a grid resolution of $0.5^\circ \times 0.1^\circ$ in Latitude and Longitude was chosen in a domain reaching from $53.5^\circ\text{N } 9^\circ\text{E}$ to $66^\circ\text{N } 31^\circ\text{E}$. This includes the Kattegat, the passage from the Baltic to the North Sea, where boundary conditions were prescribed in the east: A constant JONSWAP spectrum with a wave height of 1 m, a period of 5 s and peak wave direction of 90° with a high directional spreading. The passage from the North to the Baltic sea is very shallow, so the boundary conditions have negligible influence on the model outcome. Wave frequency range was set to 0.1 to 1.8 Hz, which mirrors the actual wave frequencies occurring in the Baltic Sea [Feistel et al. 2008], with a resolution of 42 frequency bins. Computations included a spin-up time of 10 days, sufficient for wave modeling, and were carried out for the years 2013 and 2014. The model was forced by wind data from the German Weather Service (DWD), the computational time step was 1 hour (note that the propagation scheme implemented in SWAN is implicit, so the time step is not restricted by numerical issues).

The nesting area reached from $53.5^\circ\text{N } 10^\circ\text{E}$ to $55.5^\circ\text{N } 15^\circ\text{E}$, including the Western German coastal seas. Spatial resolution was $0.01^\circ \times 0.025^\circ$ in Latitude and Longitude and the computational time step was set to 15 minutes. Boundary conditions came from the Baltic Sea model and all parameters were left unchanged.

In Fig. 4.2 the significant wave height calculated with the wave model was compared to data obtained with a wave rider buoy. The significant wave height is defined as the average wave height of the highest one-third of the waves. This value matches the visually observed wave height best and can be calculated from the zeroth-order moment of the variance density spectrum m_0 via $H_s = 4\sqrt{m_0}$ (see Appendix D for details).

In the context of a Master Thesis [Ebner 2015], the model setup for 2013 (still using the previous version SWAN 40.91AB) was extensively tested for numerical convergence and compared to measured data on several locations in the Baltic Sea. Wave parameters like significant wave height were in good agreement with available data, even in areas with complex topography. A brief description of wind wave properties and processes and a discussion the wave model SWAN can be found in Appendix D.

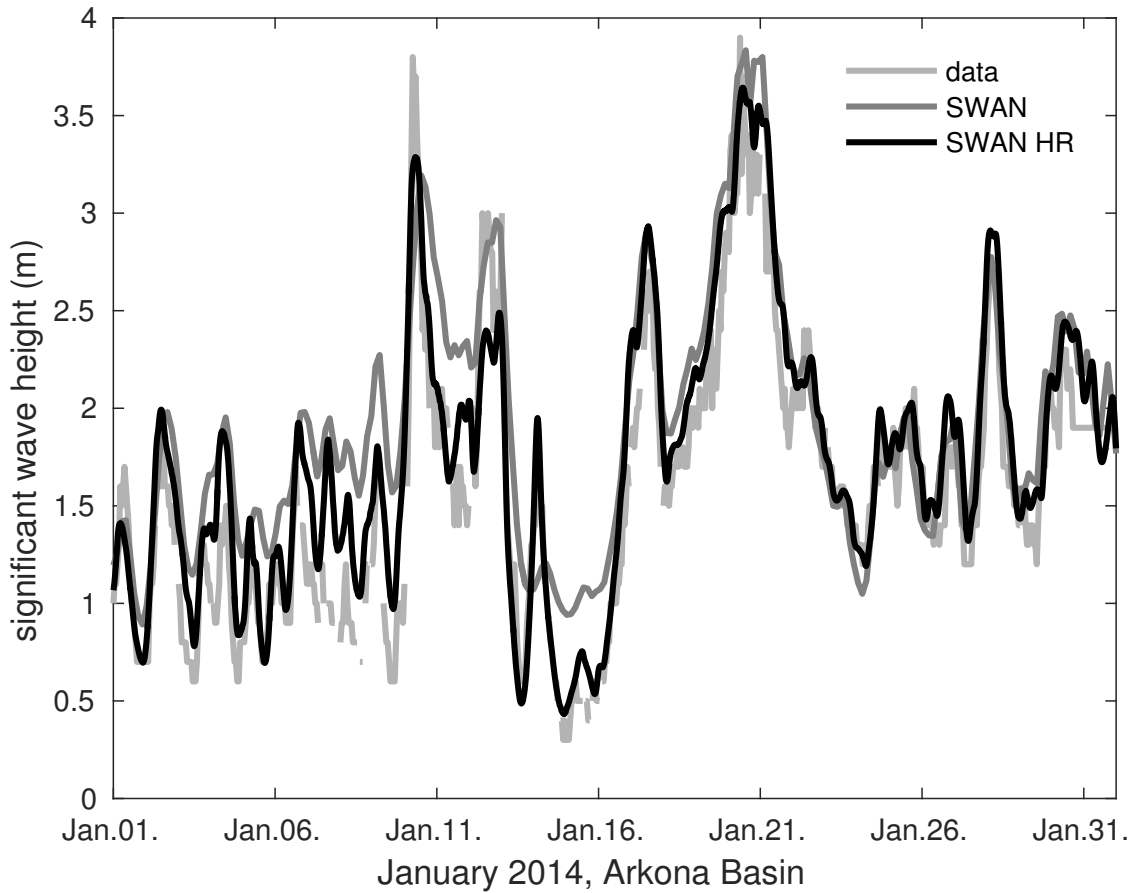


Figure 4.2.: Significant wave height calculated with the SWAN wave model (HR refers to the high resolved nested run) and measured wave height from the Arkona wave rider buoy.

4.2.2. Wave-Induced Bottom Friction Velocity Distribution

Bottom friction velocity u_* is a common quantity to express the influence of waves or currents on the sea bed. It is related to the bottom shear stress τ_b via $u_* = \sqrt{\tau_b/\rho}$, which can be estimated from a drag law of the form $\tau_b = 0.5\rho f_w U^2$. Here, ρ is the fluid density, f_w the wave friction factor and U the wave-induced maximal near bottom orbital velocity [Schwartz 2006]. Hence the relation

$$u_* = U\sqrt{0.5f_w} \quad (4.1)$$

follows. U depends on significant wave height H_s , wave length L , water depth D and wave period and is calculated in the numerical model using linear wave theory [Holthuijsen 2007; Schwartz 2006]. The wave friction factor can either be estimated using the median grain size [Swart 1974; Nielsen 1992] or from the Reynolds number

Re [Nielsen 1992; Jönsson et al. 2005, definition below] via

$$f_w = \begin{cases} \frac{2}{\sqrt{Re}}, & Re \leq 3 \times 10^5 \\ 3.34 \times 10^{-3} + 1.05 \times 10^{-9} Re, & 3 \times 10^5 < Re < 1 \times 10^6 \\ 0.024 Re^{-0.123}, & 1 \times 10^6 \leq Re. \end{cases} \quad (4.2)$$

The Reynolds number is a quantity to distinguish between laminar and turbulent flows, and in this case defined as

$$Re = \frac{UH_s}{2\nu \sinh(2\pi D/L)}, \quad (4.3)$$

with $\nu = 1.3 \times 10^{-6} \text{ m}^2 \text{ s}^{-1}$ being the kinematic viscosity.

With this, a map of the maximum wave-induced bottom friction velocity over the year 2014 can be calculated, displayed in Fig. 4.3. Although the wind conditions in 2014 might not cover all possible storm scenarios, the resulting map exhibits the same areas with high bottom friction velocities as found under two idealized wind forcing scenarios, that simulate the prevailing storm events in the Baltic Sea (wind from the northwest and the northeast, respectively, with constant wind speed of 20 m s^{-1} , simulation was run until stationarity was reached.).

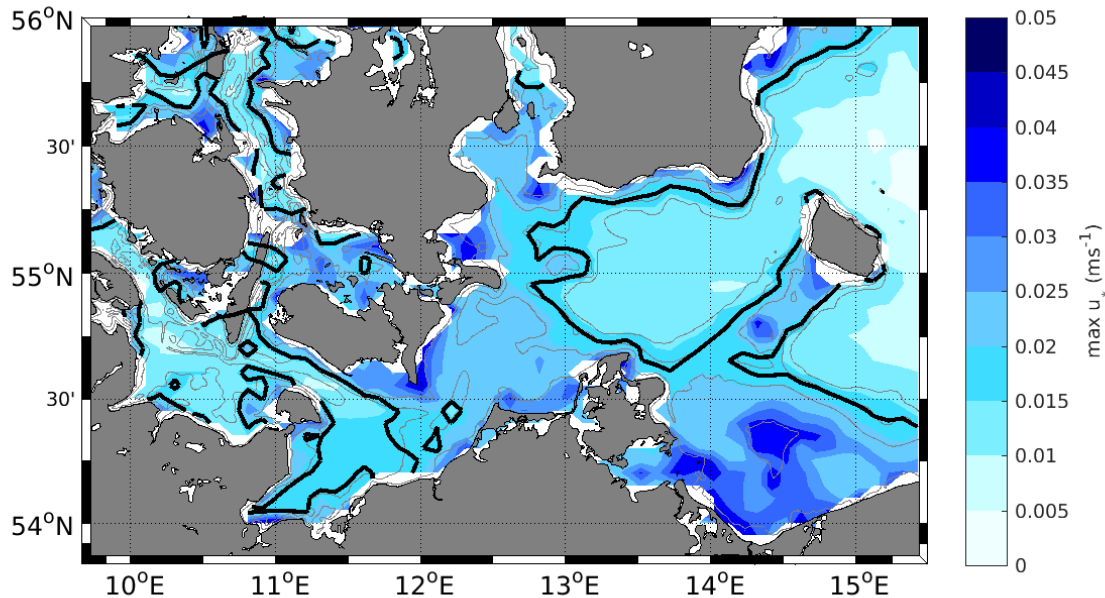


Figure 4.3.: Calculated maximum u_* using model outcome with realistic forcing from the year 2014. Gray lines show the isobaths at intervals of 10 m and the black line indicates $u_* = 0.02 \text{ m s}^{-1}$.

As visible in Fig. 4.3, high bottom friction velocities generally coincide with shallow water depth, but also topographic features, like sheltered bights or peninsulas, impact the effect of waves on the sea floor. The threshold of u_* for resuspension of sediment depends on the present sediment type, sorting and biological factors (abundant species increase or decrease resuspension thresholds) and can therefore not be definitely determined from known parameters such as grain size distribution, although extrapolations exist. Most critical values for resuspension found in the literature range from 0.01 to 0.03 m s^{-1} [Jönsson et al. 2005]. In Fig. 4.3, the black line indicates values of u_* of 0.02 m s^{-1} to give an orientation where waves play an important role for sediment dynamics.

4.3. German Coastal Seas and Sediment

General sedimentology and grain size distribution of parts of the Western Baltic Sea have been mapped in detail in a collaboration between the German maritime and hydrographic agency (BSH) and the Leibniz Institute for Baltic Sea Research (Fig. 4.4). Prevailing sediments in this area reach from fine sand to silt. Although the sediment distribution is rather inhomogeneous, some features related to the bathymetry are clearly visible. In the very shallow regions with water depth less than 20 m, predominately sandy sediments are found, while in the deeper basins finer silt is present. As fine grained material is easily eroded, it is not likely to remain in highly energetic, shallow regions and is therefore transported into the deeper basins, where it accumulates [Christiansen et al. 2002]. This process is best visible at the transition from the Oder Bight to the Arkona basin (see Fig. 4.4b). It was found that the 20 m isobath separates erosional from depositional areas, and the muddy sediments accumulate below a regional halocline here [Emeis et al. 2002]. The Arkona basin and surrounding area will be studied in more detail in the next section.

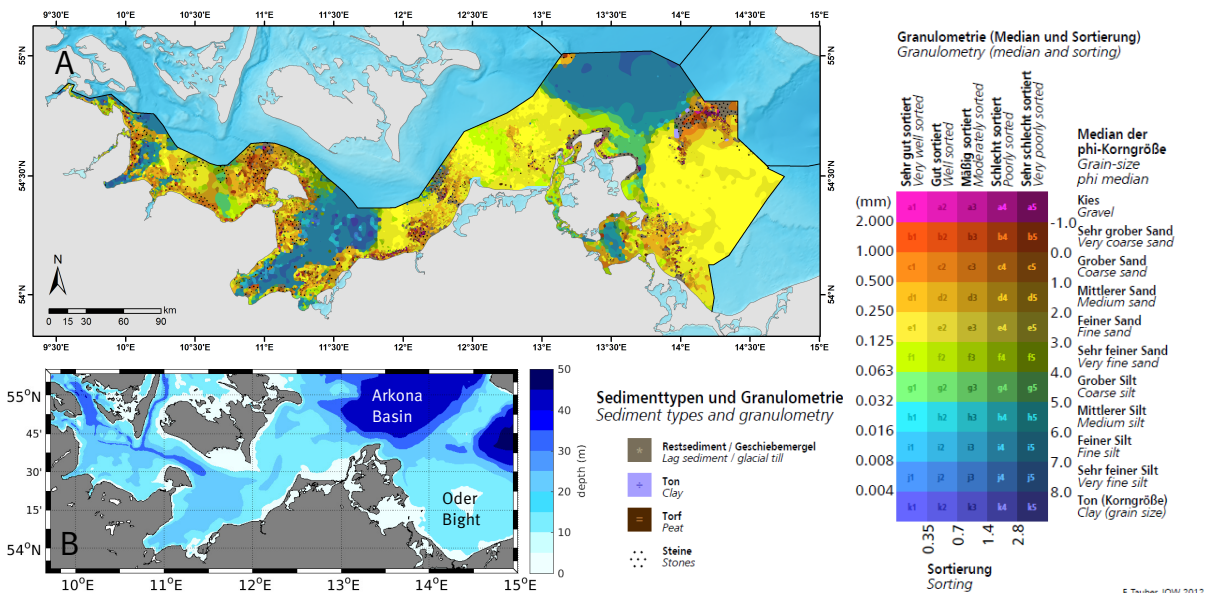


Figure 4.4.: (a) Sediment and (b) topographic map of the Western Baltic Sea. Sediment data taken from [Tauber 2012].

Chapter 5.

Near-bottom turbulence and sediment transport in the Western Baltic Sea

This study addresses the question whether the deep basins in the Baltic Sea are purely depositional or if sediment once settled there can be transported back to shallower areas. Field data, including long-term moorings and microstructure measurements, from three cruises in three different years have therefore been analyzed to investigate mean currents, turbulence, and suspended sediment concentrations. Measurements have been carried out in the transition zone from the shallow coastal regions towards the deeper parts of the Arkona Basin. It was found that onshore transport of suspended matter originating from the Arkona Basin is likely to take place in this area. Sediment dispersion by the upwelling of the regional halocline and the turbulent layer below on the one hand, and stratification asymmetries in the flow phases of an oscillatory up- and down-slope flow on the other hand have been identified as a possible mechanism for this sediment transport.

5.1. Introduction

The investigation of sediment transport patterns and the physical processes involved are essential for the understanding and mapping of many near bottom biogeochemical processes. Nutrients as well as pollutants are distributed or accumulated together with the sediment, which affects benthic communities and the exchange of dissolved substances between pore water and the overlying water column. Especially in coastal areas, a broad variety of hydrodynamical processes affect resuspension, transport, and

accumulation of sediments. In shallow areas, wind waves govern the sediment dynamics, whilst mean flow, near bottom turbulence and interior stratification become increasingly important during the transition towards the deeper areas further away from the coast.

Due to negligible tidal motions, coastal areas of the Baltic Sea provide a good opportunity to study the interplay between waves and currents and their effects on sediment transport patterns. A number of previous studies have focused on these issues. In the *Baltic Sea System Study* (BASYS), the pathways of fine-grained sediment from the near-shore regions to the deep basins were investigated with the help of numerical models and field measurements [Christiansen et al. 2002; Emeis et al. 2002; Leipe et al. 2000]. The research project *Dynamic of Natural and Anthropogenic Sedimentation* (DYNAS) investigated spatially resolved resuspension and transport patterns in the whole near-coastal area of the south-western Baltic Sea, using a numerical model [Kuhrts et al. 2004; Seifert et al. 2009]. These studies, among many others, focused mainly on large-scale sediment transport and the identification of erosional and depositional areas of the sea floor.

Naturally occurring small-scale turbulent motions, which are an important factor for sediment transport processes, have not been included in the projects mentioned above. In Christiansen et al. [2002], critical sediment resuspension thresholds have been investigated by creating artificial turbulence above collected sediment cores in the laboratory. Direct in-situ measurements of natural near-bottom turbulence and its relation to sediment parameters have, to my knowledge, not been carried out yet in the region investigated in this study.

Turbulent motions affect the bottom shear stress that causes resuspension, and determine how suspended matter is mixed up in the water column. In the interdisciplinary project *The Service of sediments in German Coastal Seas* (SECOS), in which the present study was carried out, these small-scale processes were examined with an extensive field program. This included ship-based turbulence microstructure measurements and long-term mooring deployments. Observations of suspended matter concentration from optical backscatter sensors, mean currents, waves, and turbulent motions were combined to study the relative effect of these processes on sediment transport at a number of key locations. One of the regions where measurements were carried out was the transition zone from the near-coastal region to deeper parts of the Arkona Basin north of the island Rügen. This region is considered to be a prototyp-

ical transition area for the investigation of the different processes responsible for the sediment transport processes in the Western Baltic Sea.

In addition, this area provides the prerequisites for the occurrence of the slope-induced tidal straining process discussed in the previous chapters [Umlauf and Burchard 2011; Schulz and Umlauf 2016]. Both the slope of the sea floor and interior vertical stratification are sufficient to trigger residual sediment transport under an oscillatory current. Although tides are negligible in the Baltic Sea, a distinct signal of inertial oscillations with a period of approximately 15 h was visible over five day continuous of current measurements. This setting certainly exceeds the capability of the one-dimensional numerical model used in Schulz and Umlauf [2016], as the slope angle is changing and the vertical stratification is greatly enhanced in the region of the present halocline, making the problem at least two-dimensional. Nevertheless, sediment transport from the basin up the slope could be induced by slope-induced tidal straining under the conditions given in this region.

The deep basins in the Baltic Sea, like the Arkona Basin, are depositional areas. Net sedimentation can be measured, and sediment is transported from the coast to the basins [Christiansen et al. 2002; Emeis et al. 2002]. The main question addressed in this study is whether this transport is directed purely one way, or if processes exist which can transport parts of the sediment from the deep basins back to shallower areas.

5.2. Study Area

The general properties of the Baltic Sea have already been discussed in the last chapter. Here, a brief introduction to the general hydrodynamic processes which govern the current system near the measurement site on the one hand, and the sediment distribution on the other is given.

5.2.1. Hydrography and dynamics

In Fig. 5.1, the bathymetry of the study area and its position in the Western Baltic Sea is displayed. The Arkona Basin has a maximum depth of around 45 m and an

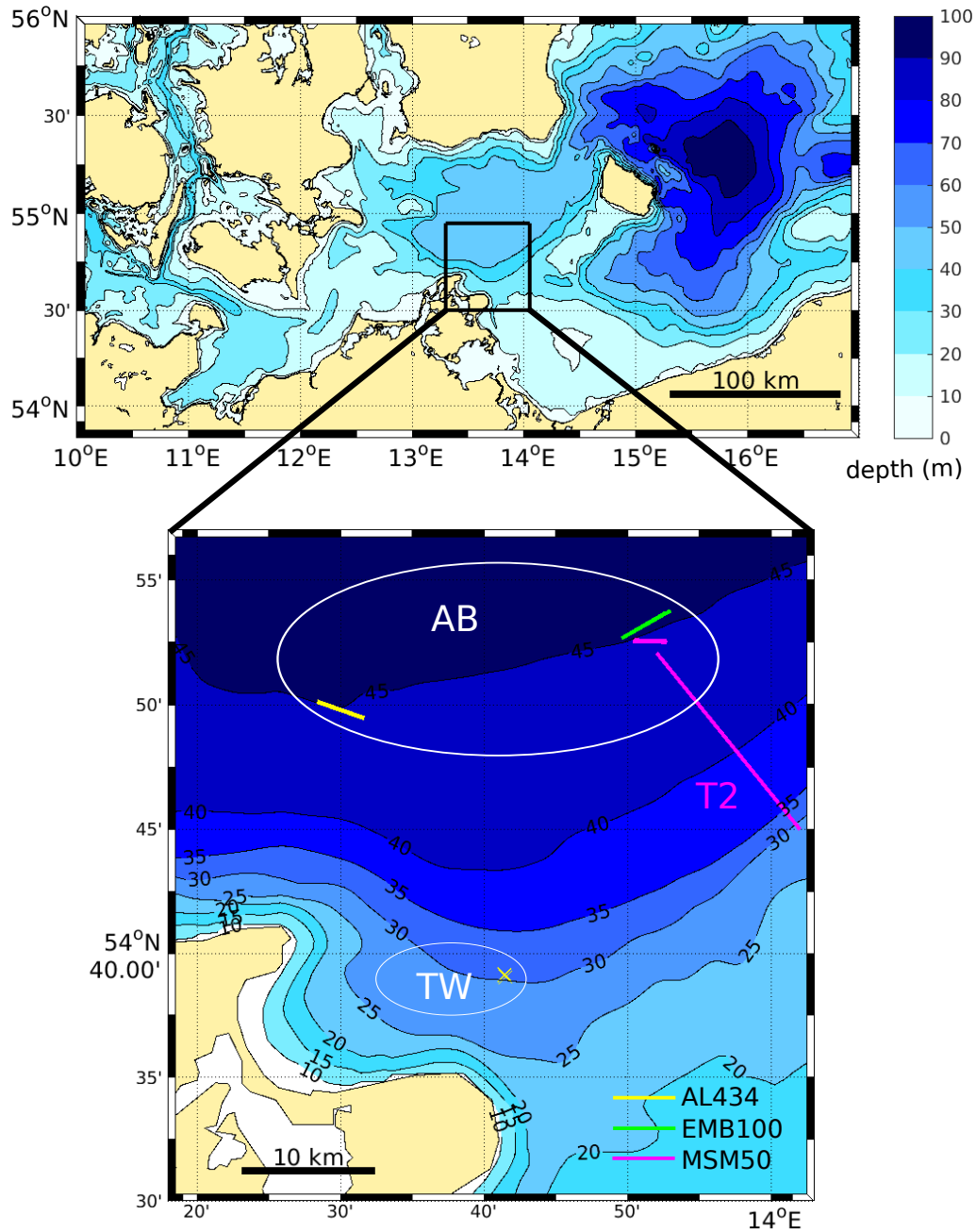


Figure 5.1.: Bathymetric map of the Western Baltic Sea and an enlargement of the study area. Deployments during cruise AL434 are indicated in yellow, from EMB100 in green and from cruise MSM50 in magenta. Crosses mark the position of deployed moorings, lines refer to microstructure profiler transects. White ellipses indicate the positions referred to as TW (Tromper Wiek) and AB (Arkona Basin), respectively.

extension of nearly 75 km in meridional and 110 km in longitudinal direction [Lass et al. 2005]. The inertial period is around 14.6 h in this region. The flow patterns in this area have already been investigated with extensive field measurement, e.g. in Lass and Talpsepp [1993]. In a study on the Pomeranian Bight (i.e. the shallow area connecting the Arkona Basin in the west, the Bornholm Basin in the east, and the mouth of the Oder river), Lass et al. [2001] also investigated the study site described here both observationally and with a high-resolution circulation model. In addition, the same authors carried out measurements in two consecutive winters in the Arkona Basin and analyzed the flow dynamics there [Lass and Mohrholz 2003; Lass et al. 2005]. General information about the deep water of the Baltic Sea, and especially the Arkona Basin, are summarized in Meier et al. [2006]. The dynamics of near-inertial waves in the deep basins of the Baltic Sea have been investigated in Van der Lee and Umlauf [2011], with help of a field campaign in the Bornholm Basin. These studies give a good overview of the flow patterns and dynamics of the area investigated in this study.

From the exchange with the North Sea, dense bottom currents of saline waters enter the Arkona Basin via the Darss Sill and the Drögden Sill (see previous chapter). Coriolis effects and bottom friction determine the propagation of the saltwater plumes, forming a topographically trapped rim current which cyclonically encircles the basin and slowly deepens with increasing distance from the sills [Lass et al. 2005]. The saline water is diluted and feeds the central pool of dense water in the basin, which discharges through the Bornholm Channel (north of the island Bornholm, see last chapter). Residence time of the salt water in the Arkona Basin is around 1-3 months [Lass et al. 2005; Meier et al. 2006].

As inflow events are driven by larger scale wind forcing, this process is not steady, and the dense bottom current is modulated by pulses of inflowing water and can disappear completely. During an inflow event, baroclinic Kelvin waves travel around the perimeter of the basin within 4 days, while the halocline is lifted up and the saline bottom pool is filled with inflowing water. In summer, warm inflow waters sandwich into the halocline. Bottom water spills over the Bornholm Channel whenever the height of the bottom pool exceeds the depth of the Channel. All this causes the position of the halocline to be highly variable in time, and also depending on the position in the basin. For example, after an inflow event in December 1998, the upper layer of the dense bottom water pool was found to be located at 40 m depth in the central basin

and at about 30 m depth at the southern rim. Three month later, the halocline was found to be at around 35 m depth throughout the basin [Lass et al. 2005].

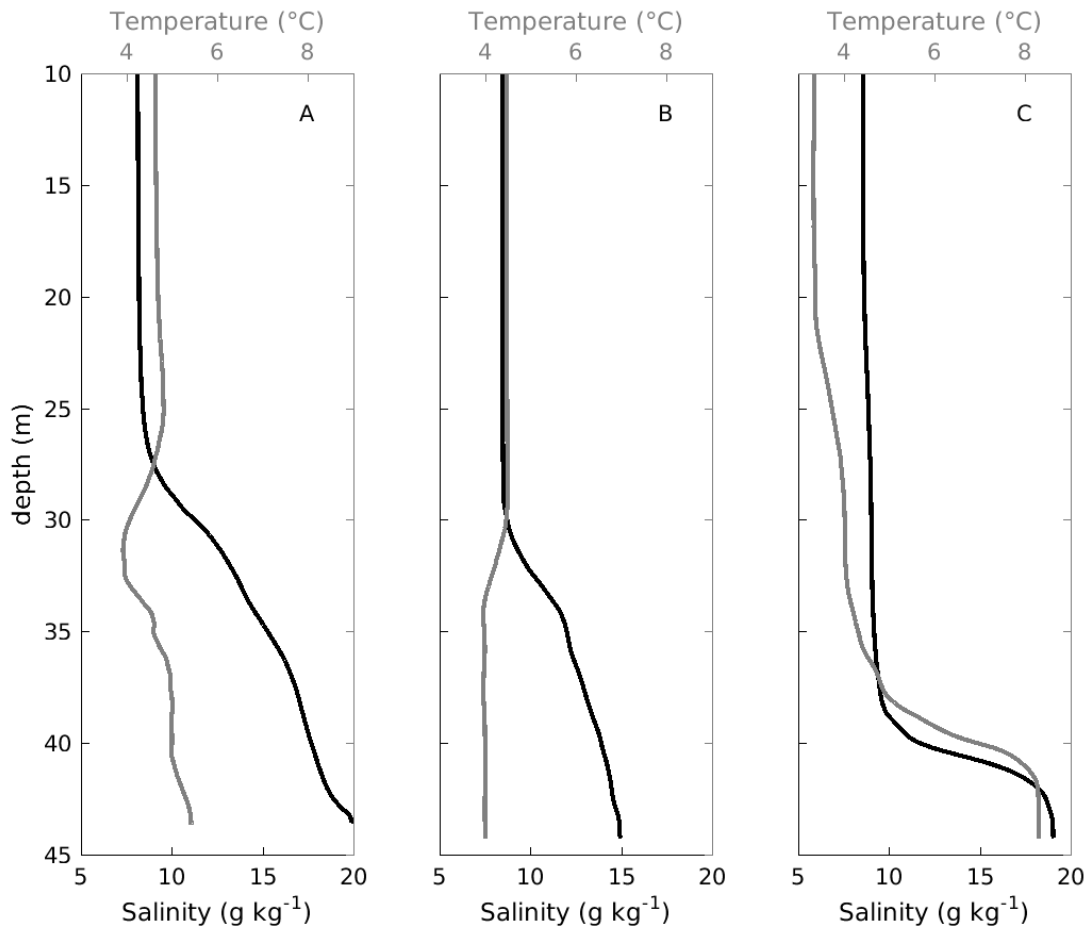


Figure 5.2.: Vertical structure of salinity (black lines) and temperature (gray lines) in the Arkona Basin in (a) April 2014, (b) April 2015 and (c) January 2016. Data are averaged over several microstructure profiles, details on the instrument and time and location of the deployments will be given in the following sections.

This variability is also visible in the data obtained during this study. On each of the three cruises, microstructure measurements were performed in the Arkona Basin (see Fig. 5.1). In Fig. 5.2, vertical profiles of temperature and salinity are displayed. The upper layer of the dense bottom pool is commonly characterized by a salinity of 11 g kg^{-1} [Lass et al. 2005]. In April 2014 and 2015 (Fig. 5.2a,b), the halocline was located relatively high in the water column, at around 27 m and 31 m depth, respectively. In January 2016, the interface between dense bottom and overlying water is very sharp and positioned deeper in the water column, at around 40 m depth. The relatively high near-bottom salinity and the sharp interface originated from a

preceding weak inflow on 05–07 December (approximately 50 days before the data displayed in Fig. 5.2c were obtained), during which around 33 km³ North Sea water with a temperature of 8°C entered the Baltic Sea (*personal communication* Michael Naumann, Working Group Environmental Monitoring, Leibniz Institute for Baltic Sea Research Warnemünde). The extent of the dense water pool has important effects on the near-bottom dynamics. The halocline separates the turbulent BBL from the overlying water body. The halocline height therefore determines, for example, how far suspended matter is mixed up into the water column, and influences near-bottom turbulence and resuspension.

Besides the dense bottom currents, other flow patterns and hydrodynamic processes have been observed in the Arkona Basin, including different oscillatory motions that are important for the generation of near-bottom turbulence. Lass and Mohrholz [2003] found that the barotropic cyclonic motions of the bottom current perform basin-wide zonal oscillations on timescales of one week. This is in agreement with the findings of Lass et al. [2001] that near-shore currents reveal an elliptical motion, with the main axis being aligned along the isobaths. North of the island Rügen, the currents are slightly more pronounced towards the east. The cross-shore component is generally weaker, but still on the order of 0.1 m s⁻¹ [Lass and Talpsepp 1993; Lass et al. 2001].

Another factor determining the flow conditions is local wind forcing that causes upwelling and downwelling near the shore. Wind from the east drives a long-shore current to the west. In cross-shore direction, Ekman transport causes the surface flow to be directed seaward. This induces a near-bottom return current towards the land [Lass and Talpsepp 1993]. The salt water pool in the Arkona Basin is consequently tilted upwards on the southern rim of the basin [Lass and Mohrholz 2003; Lass and Talpsepp 1993, their Fig. 11]. During wind from the west, the situation is reversed.

Energetic inertial oscillations and waves in the Arkona Basin have been observed, but not further investigated, in Lass and Talpsepp [1993]. Van der Lee and Umlauf [2011] carried out a study on internal-wave mixing in the Bornholm Basin and found that inertial oscillations and near-inertial wave motions govern the energetics near the slopes of the basin. Density stratification and topographic structure are comparable in the Bornholm and Arkona Basin, suggesting that inertial oscillations also play an important role there.

During cruise AL434, velocity profiles on the southern rim of the Arkona Basin were obtained with a moored current meter for more than 5 days (see Fig. 5.1, yellow marks). In Fig. 5.3, the cross-slope component of the near-bottom current (1.7 m above sea floor) is displayed. The time series clearly exhibits an oscillatory signal with near-inertial period and an amplitude in the order of 0.1 m s^{-1} . Furthermore, from microstructure data obtained during cruises MSM50 (displayed and discussed in the next sections), it can be seen that the halocline is rather aligned with the slope than straight horizontal, and that the extent of the dense bottom pool is in agreement with the extent found in the microstructure data from the deeper parts of the basin at that time, displayed above in Fig. 5.2c. As the observed stratification strength and the slope angle are within the range for the occurrence of slope-induced tidal straining found in Schulz and Umlauf [2016], it can be speculated whether this process might play a role here.

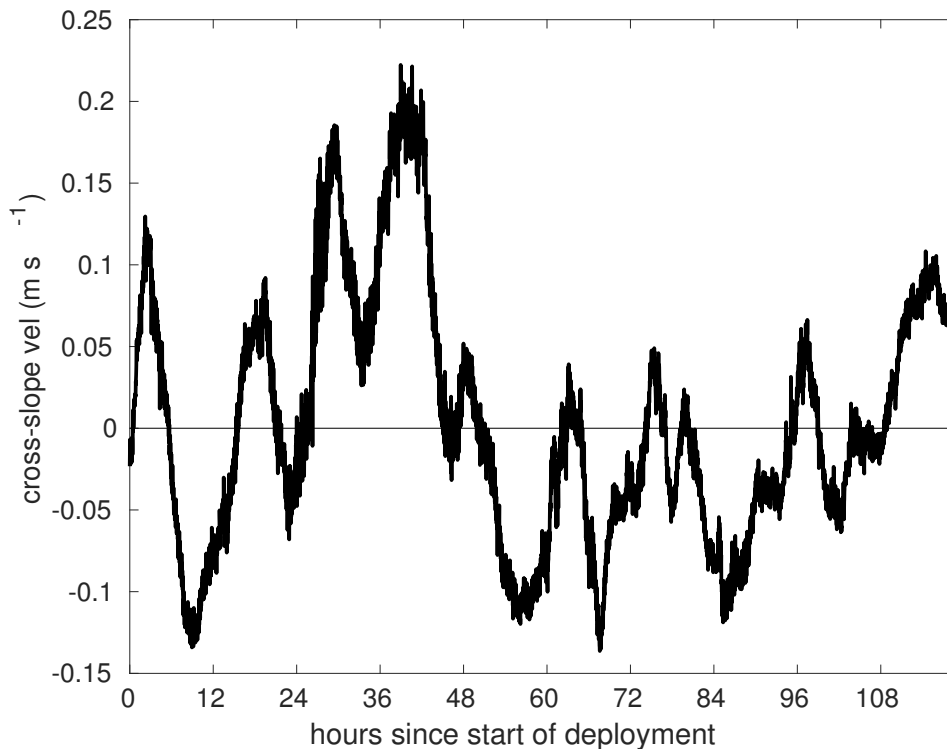


Figure 5.3.: Approximately five days of cross-slope (i.e. cross-isobath) near-bottom currents are displayed, obtained at TW with a 1200 kHz ADCP in April 2014 (see Tab. 5.1, first column). Positive means up-slope. The exact descriptions of instrument and deployment follow below.

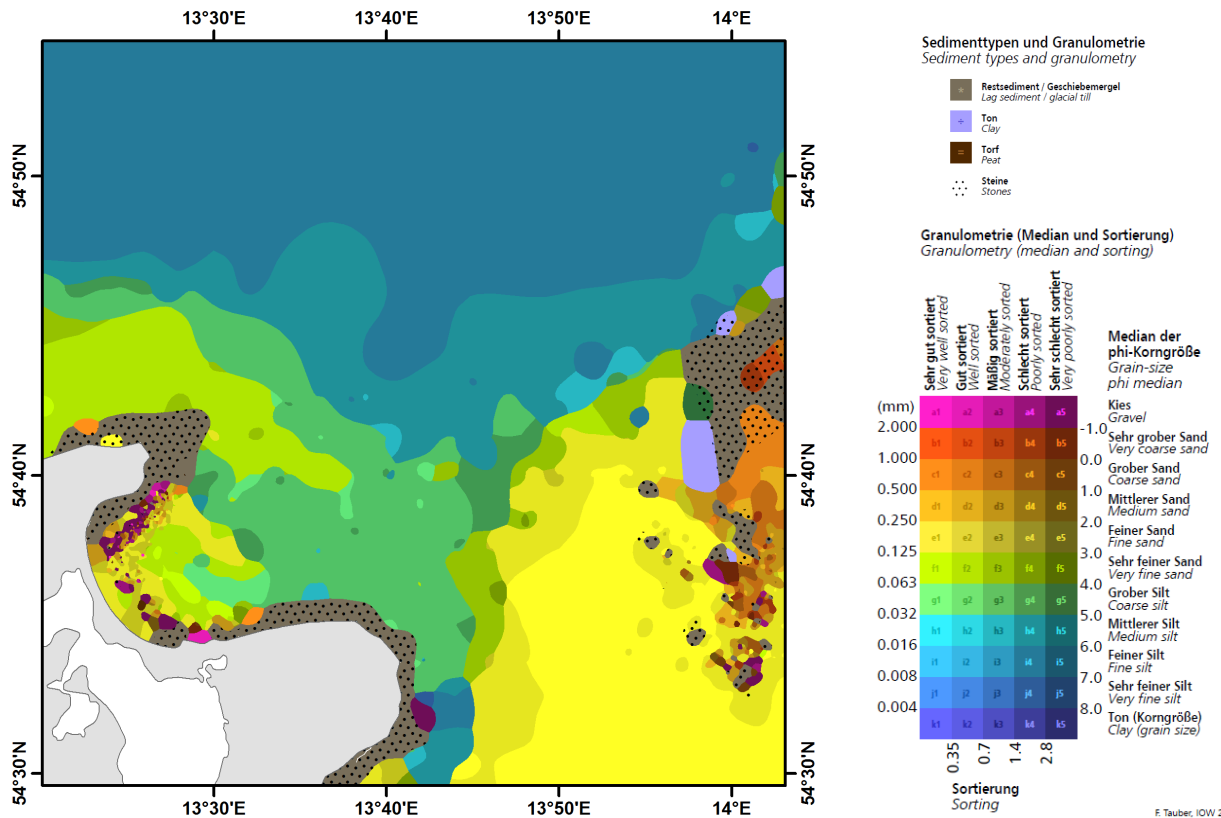


Figure 5.4.: Sediment distribution in the study area. Data were taken from Tauber [2012].

5.2.2. Sedimentology

Sediment distribution in this area is heterogeneous in the shallow regions with predominately medium to fine sand. At water depths below 25 - 30 m in the Arkona Basin, sediment is relatively fine-grained and consists homogeneously of silt (Fig. 5.4). In the vicinity of TW (see map in Fig. 5.1), a special type of fine-grained and organically poor sediment is found.

Previous studies [Leipe et al. 2000; Christiansen et al. 2002] found the Arkona Basin to be a deposition center for material originating from the shallower areas, with accumulation rates of around 2.2 mm/yr. Sediment characteristics in the Arkona Basin resemble those of a fluffy layer, implying that sediment is easily resuspended with resuspension thresholds of approximately 0.02 N m^{-2} [Christiansen et al. 2002, determined with a LABEREX chamber from sediment core samples]. Due to its low settling velocity of less than 10^{-3} m s^{-1} , sediment remains suspended for a relatively long pe-

riod of time. Closer to the coast, a fluff layer was found to be present most of the time. Values for critical resuspension thresholds and settling velocities were therefore only slightly higher than the ones observed in the deep parts of the basin, even though the prevailing sediments are coarser in the shallower parts [Christiansen et al. 2002].

A consecutive study [Emeis et al. 2002] found the 20 m isobath to be the border between erosional and depositional sites in this area, suggesting that the Tromper Wiek region (see map in Fig. 5.1) is depositional as well. These authors also pointed out that muddy sediments accumulated below the halocline in this region.

5.3. Instrumentation

Hydrographic and turbulence data were obtained at several locations throughout the German coastal area during three cruises with R/V *Alkor* in spring 2014 (AL434, 28.03.-08.04.2014), R/V *Elisabeth Mann Borgese* in spring 2015 (EMB100, 09.04.-16.04.2015) and R/V *Maria S. Merian* in winter 2016 (MSM50, 05.01.-29.01.2016). Here, exclusively data obtained in the transition zone from the coast off the island Rügen (called Tromper Wiek (TW), around 30 m water depth) to the approximately 45 m deep Arkona Basin (AB) are discussed. The exact positions of deployed moorings and ship-based microstructure profiler transects are indicated in Fig. 5.1, where colors mark the cruise during which the measurements were performed.

Three different types of moorings were deployed near position TW during cruise AL434. A CTD-Chain consistent of 8 CTD-loggers (MicroCat type SBE37-SM from Seabird, USA), tied to a mooring line at intervals of 1 m, starting at 1 m above the seabed, with additional optical backscatter (OBS) sensors (NTU from Wetlabs, USA). CTD data were sampled every 10 s, and the backscatter sensor obtained 8 consecutive samples in 1 s intervals every minute. Data from the OBS sensor were calibrated and expressed in Nephelometric Turbidity Units (NTU). Lander 1 was a bottom-mounted instrument frame, equipped with an upward looking 1200 kHz acoustic Doppler current profiler (ADCP, Teledyne RDI, USA) and a 6 MHz single-point acoustic Doppler velocimeter (ADV, Vector from Nortek AS, Norway). Lander 2 was a similar bottom frame and, amongst other instruments, equipped with an upward looking 600 kHz ADCP (Teledyne RDI, USA).

Table 5.1.: Deployment duration (UTC), position and instrumentation of the moorings deployed during cruise AL434 in April 2014 at position TW (see Fig. 5.1).

	CTD-Chain	Lander 1	Lander 2
deployment	03.04.2014, 06:54	03.04.2014, 06:27	03.04.2014, 06:40
recovery	08.04.2014, 06:19	08.04.2014, 06:47	08.04.2014, 07:05
position	54°39.05'N 13°41.48'E	54°39.17'N 13°41.45'E	54°39.12'N 13°41.45'E
instruments	8 MicroCat 1-8 m AG 2 NTU 2.5, 4.5 m AG	ADV 1200 kHz ADCP MicroCat NTU	2 MHz Aquadop 600 kHz ADCP

The 1200 kHz ADCP sampled approximately the lowest 15 m of the water column in intervals of 0.5 m, with the lowest bin located at 1.6 m above the ground. And the instrument was operated in RDI “mode 12”, averaging measured velocity profiles over one set of 4 sub-pings at 300 ms intervals every 2 s. Velocity profiles over the whole water column were obtained with the 600 kHz ADCP, again in 0.5 m intervals with the lowest bin located 1.7 m above the ground. Velocity profiles were measured every 2 seconds, averaged from 4 sub-pings in 220 ms intervals. To reduce measurement uncertainties, velocity estimates from both ADCPs were averaged over 60 s in time. The ADV was operated in continuous mode at a sampling rate of 32 Hz. The sampling volume was located 1.14 m above the ground.

Deployment times of the moorings, exact deployment position and instrumentation are listed in Tab. 5.1.

Additionally, ship-based microstructure profiler measurements were performed near position AB with a MSS90-L microstructure profiler (ISW, Germany). The instrument contained a set of precision CTD sensors (SST, Germany), a fast FP07 thermistor, a turbidity sensor, and two airfoil shear-probes (PNS06 from ISW, Germany). The sensors were protected with a cage, so profiles were obtained nearly full-depth until less than 0.1 m above the ground. During a transect (duration of 1 to 5 hours) the profiler was continuously operated from the stern of the ship, free-falling through the water column with an approximate sinking speed of 0.5 m s^{-1} , while the ship moved at 1-2 kn. Depending on water depth, one profile was measured every 3 to 5 minutes. When multiple transects were performed consecutively, the ship turned after the end of each

Table 5.2.: Duration (UTC), start and end coordinate and number of microstructure transects performed near AB, total number of profiles in brackets.

cruise	AL434 (2014)	EMB100 (2015)	MSM50 (2016)
start position	54°50.100'N 13°28.428'E	54°53.689'N 13°52.694'E	54°52.554'N 13°52.698'E
end position	54°49.464'N 13°31.620'E	54°52.695'N 13°49.694'E	54°52.548'N 13°50.508'E
duration	05.04. 16:18 - 06.04. 01:06	14.04. 16:41 - 15.04. 05:20	23.01. 13:21 - 24.01. 16:41
transects	5 (119 profiles)	5 (184 profiles)	7 (431 profiles)

on MSM50	T1 (86 profiles)	T2 (120 profiles)
start position	54°52.079'N 13°52.036'E	54°36.143'N 13°43.012'E
end position	54°44.992'N 14°02.022'E	54°50.711'N 13°43.009'E
duration	24.01. 19:28 - 24.01. 23:42	28.01. 09:45 - 28.01. 17:05

transect and was repositioned to the starting position. Data processing routines were the same as described in Van der Lee and Umlauf [2011], their section 2.2. Data were despiked and averaged to 256 Hz resolution. CTD data were binned to 0.1 m intervals in the vertical. Dissipation rates were calculated under the assumption of local isotropy in the dissipative subrange from the vertical shear spectra and averaged into vertical intervals of 0.5 m.

Position and time of the transects for each cruise are summarized in Tab. 5.2.

5.4. Observations

The data obtained as described above are discussed in the following, starting with measurements from the deep parts of the Arkona Basin to understand the structure of the water column there. After that, a 13 km turbulence microstructure profiler transect onshore towards shallower areas is discussed to highlight the connectivity between deep and shallow areas. Finally, data from moored instruments deployed near TW for several days are displayed and analyzed.

5.4.1. Arkona Basin

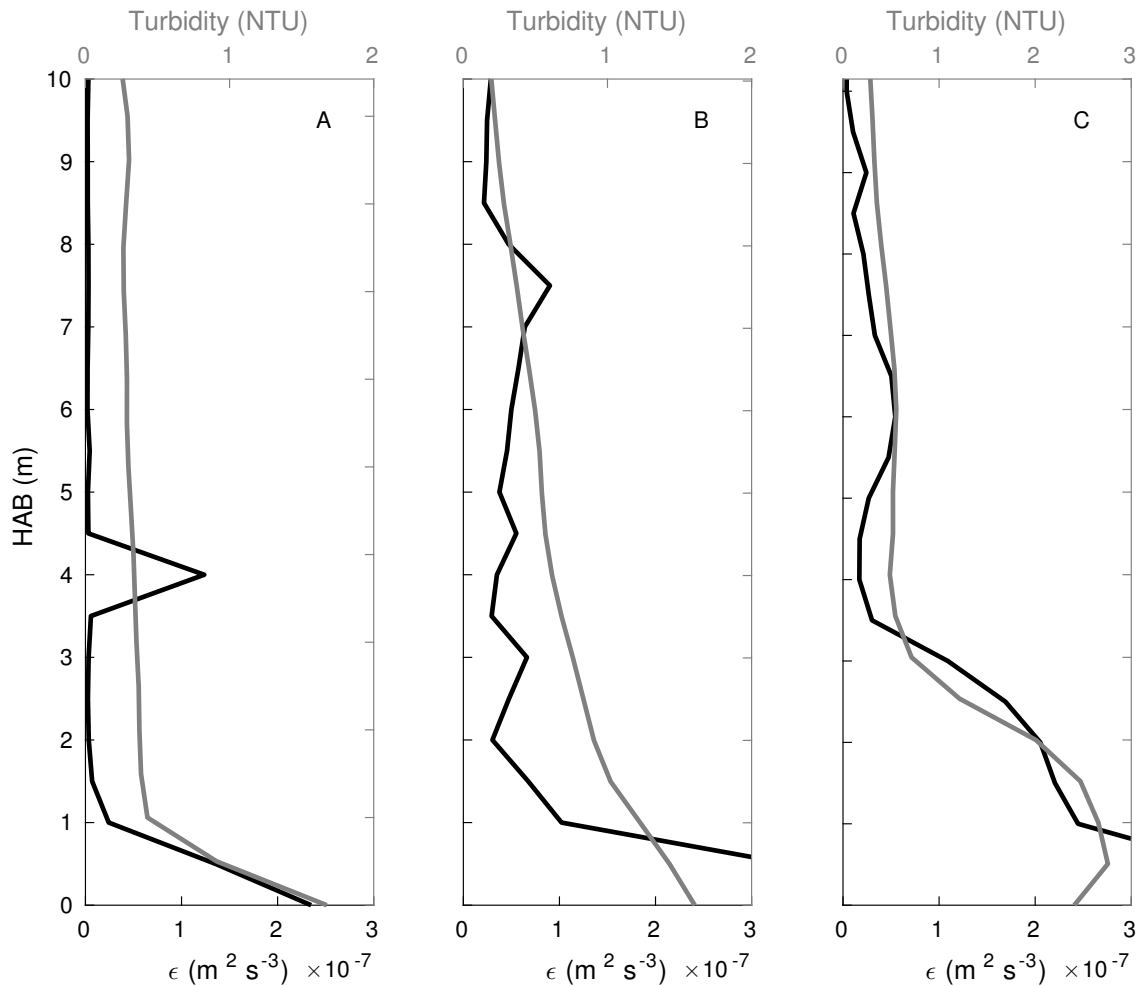


Figure 5.5.: Turbidity (gray lines) and dissipation rate (black lines) from all microstructure transect performed in the Arkona Basin. Displayed data are the average over (a) a total of 119 microstructure profiles obtained during 5 transects on 05 April 2014 on cruise AL434 were averaged, (b) 184 profiles from 5 transects on 14-15 April 2015 on cruise EMB100 and (c) 431 profiles from 7 transects on 23-24 January 2016 on cruise MSM50. Only the lowermost part of the water column is displayed here.

During each of the three cruises AL434, EMB100 and MSM50, microstructure measurements were performed in the Arkona Basin, indicated with AB in Fig. 5.1. Fig. 5.5 shows the profiles of dissipation rate and turbidity, averaged over all profiles obtained at this station, for each cruise. A turbulent bottom boundary layer (BBL) is visible in all three profiles, ranging from 1 to 5 m thickness. Turbidity is enhanced in the BBL, suggesting that the suspended sediment causing this turbidity originates from the sea floor. As these measurements were performed over three years and in different sea-

sons, it is most likely that this turbid, very sharply defined BBL is constantly present in the Arkona Basin.

The above results indicate that suspended sediment transported to the Arkona Basin is not necessarily deposited there forever, but is either held in suspension or occasionally resuspended and mixed into the turbulent BBL. This is in agreement with previous studies that found the sediment in the basin to be fluff-like, easily resuspended and slowly settling, see section 5.2.2. On the other hand, this reservoir of fine grained suspended sediment has the potential to be advectively transported across the rim of the Arkona Basin into the shallower areas by onshore currents. Under the conditions of present oscillatory currents, interior vertical stratification and a bottom slope discussed in the previous sections, the Arkona Basin could be a source of sediment to be transported up-slope in the process of slope-induced tidal straining.

5.4.2. Transect from basin to the coast

Fig. 5.6 shows how the water body is structured along the slope from the deep basin towards the coast. A sharp halocline separates a turbulent BBL of approximately 5 m thickness from the interior. At the southern end of the transect, where the slope angle steepens, the halocline is widened where it approaches the sea floor. These data were obtained in January 2016.

The boundary layer is generally turbid. Turbidity is more patchy towards the shallow areas, but high values are confined to the bottom boundary layer, so no suspended matter is mixed across the halocline. This indicates again that turbidity is caused by material originating from the sea floor and held in suspension by turbulent motions in the BBL.

The isohalines (please note that salinity mainly determines the density in this region) in Fig. 5.6 show a clear cross-slope density gradient below the halocline. In the presence of an oscillatory current, periodic stratification and consequently residual (upslope) sediment transport as described in Schulz and Umlauf [2016] is within the realms of possibility here.

Although this transect is just a snapshot of the situation in January 2016, there are several indicators that these conditions are usually present here: Turbulent and turbid boundary layers have been visible on all microstructure transects in the Arkona Basin

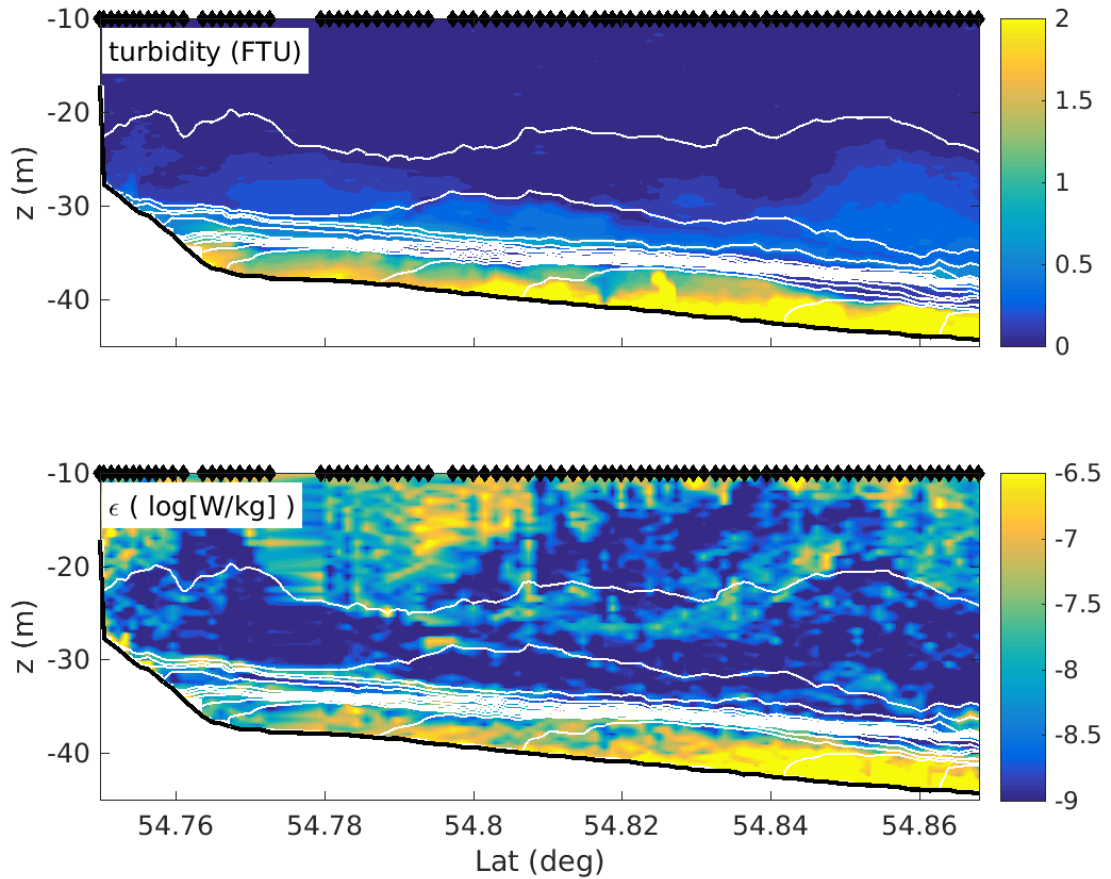


Figure 5.6.: Turbidity and dissipation rate from the microstructure transect T2 in January 2016. White lines indicate levels of equal salinity.

in three years (see above section), and the regional halocline is constantly present, although the extension of the dense bottom water pool might differ. Consequently, this transect gives an idea of the water body structure along a cross-section from the basin to the coast.

5.4.3. Tromper Wiek

In the data from the onshore transect in the last section, it was visible that high turbidity values, present throughout the BBL, reach out to water depths well below 35 m. In this section, data from instruments deployed at 29 m, resembling the shallow end of the transect, are displayed. These data were obtained in April 2014, nearly two years before measurements for transect T2 were performed. However, as the structure of

the water body was similar during all three cruises, the general situation during the two measurements is presumably comparable.

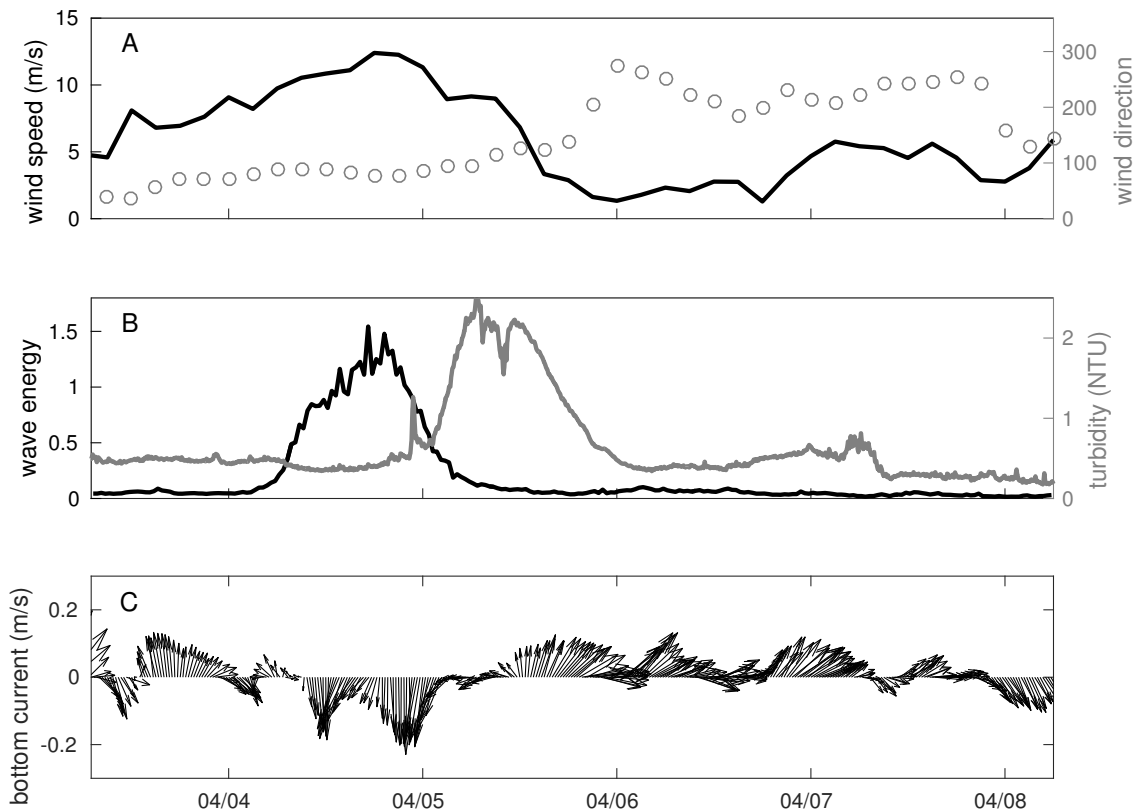


Figure 5.7.: Displayed are (a) wind speed and direction from the hindcast of the German Weather Service, (b) wave energy calculated from ADV data, and turbidity from the OBS sensor, and (c) direction of near bottom current, obtained with the 1200 kHz ADCP at 1.6 m above the seabed, all mounted on Lander 1 during the deployment at TW on cruise AL434 (April 2014).

During the 5 day instrument deployment a wind event with wind speeds up to force 7 and up to 4 m wave height was captured, followed by a calm period (Fig. 5.7a). In Fig. 5.7b the variance of the horizontal velocity components, which is proportional to the kinetic energy contained in the waves, is displayed. This quantity was based on data from the ADV (obtained at circa 1.2 m above the sea floor), that were despiked [Goring and Nikora 2002] and filtered for wave periods between 2 and 20 seconds with a second-order Butterworth bandpass filter. Although wave energy was maximum in the afternoon of 04 April 2016, the peak in turbidity was not reached until late morning of 05 April. This suggests that local resuspension during the wind event did not occur, but that a turbid water mass was advected to the measurement site. Near-

bottom currents (Fig. 5.7c) were directed south during the relevant period, i.e. water from deeper parts was advected up the slope.

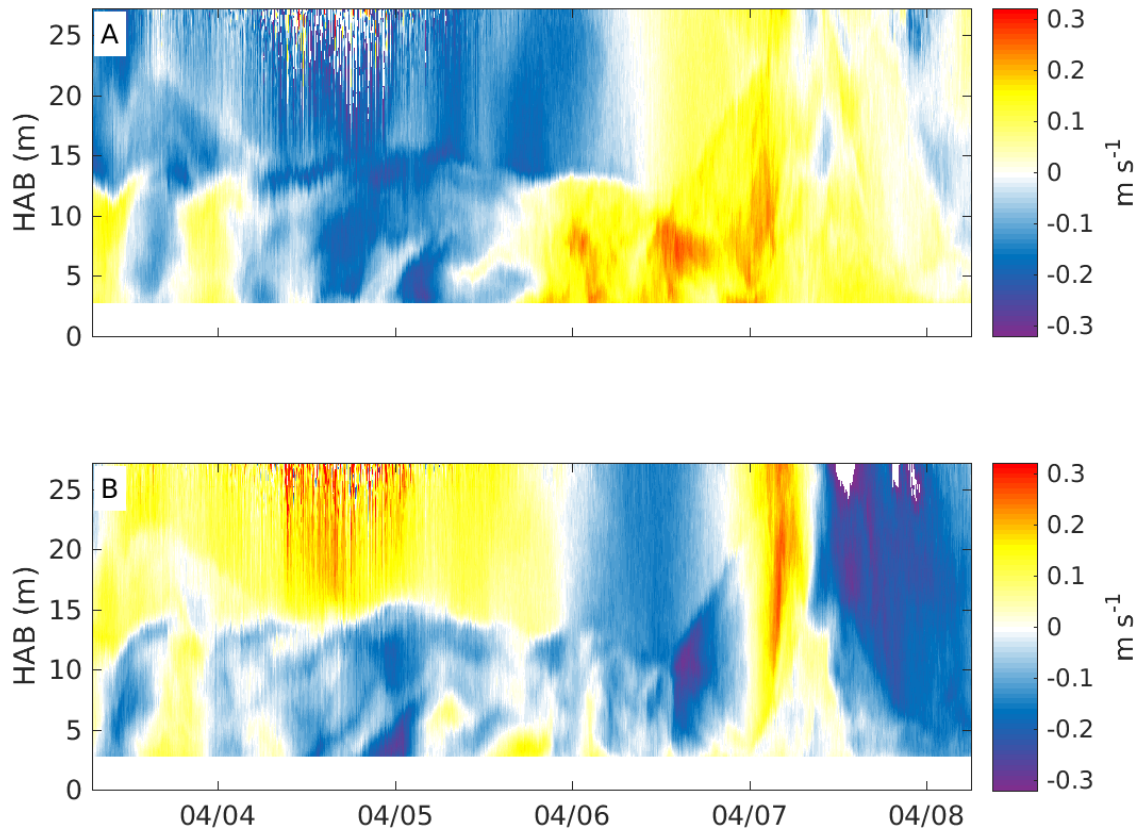


Figure 5.8.: Contour plots of the (a) east and (b) north components of the current velocity, obtained with the 600 kHz ADCP on Lander 2 during the deployment at TW on cruise AL434 (April 2014).

This advection of saline waters near the bottom was likely triggered by local wind forcing. Strong easterly wind caused Ekman transport to the north (i.e. offshore) in the surface layer [Lass et al. 2001], which is visible in the velocity data from the 600 kHz ADCP mounted on Lander 2, displayed in Fig. 5.8¹. The near-bottom return current below 17 m depth exhibits a clear near-inertial signal, super-imposed on a southerly (i.e. onshore) mean current during the storm. Maximum onshore bottom currents were reached by the beginning of 05 April. After the winds collapsed

¹Corrupted velocity measurements in the uppermost part of the water column during 04 April coincide with the periods when strong surface waves were recorded with the ADV. These problems most likely originate from air bubbles entrained by breaking waves.

and changed direction at the end of 05 April, the surface currents first decayed and then reversed to southerly directions. Near-bottom currents remained unsteady with a mean easterly component (Fig. 5.7c).

In the CTD Chain data in Fig. 5.9 an increase of the near-bottom salinity is visible, accompanied by increasing turbidity, starting in the afternoon of 04 April. The increase in turbidity is clearly linked to the increase of salinity, supporting the idea that turbid water is advected to position TW from deeper regions. Furthermore, salinity data in the record reaches a level that resembles the saline bottom waters in the Arkona Basin below the halocline (see Fig. 5.2). This indicates that upwelling tilted the halocline, lifted it up in the south and saline bottom water reached far upslope onto the shore.

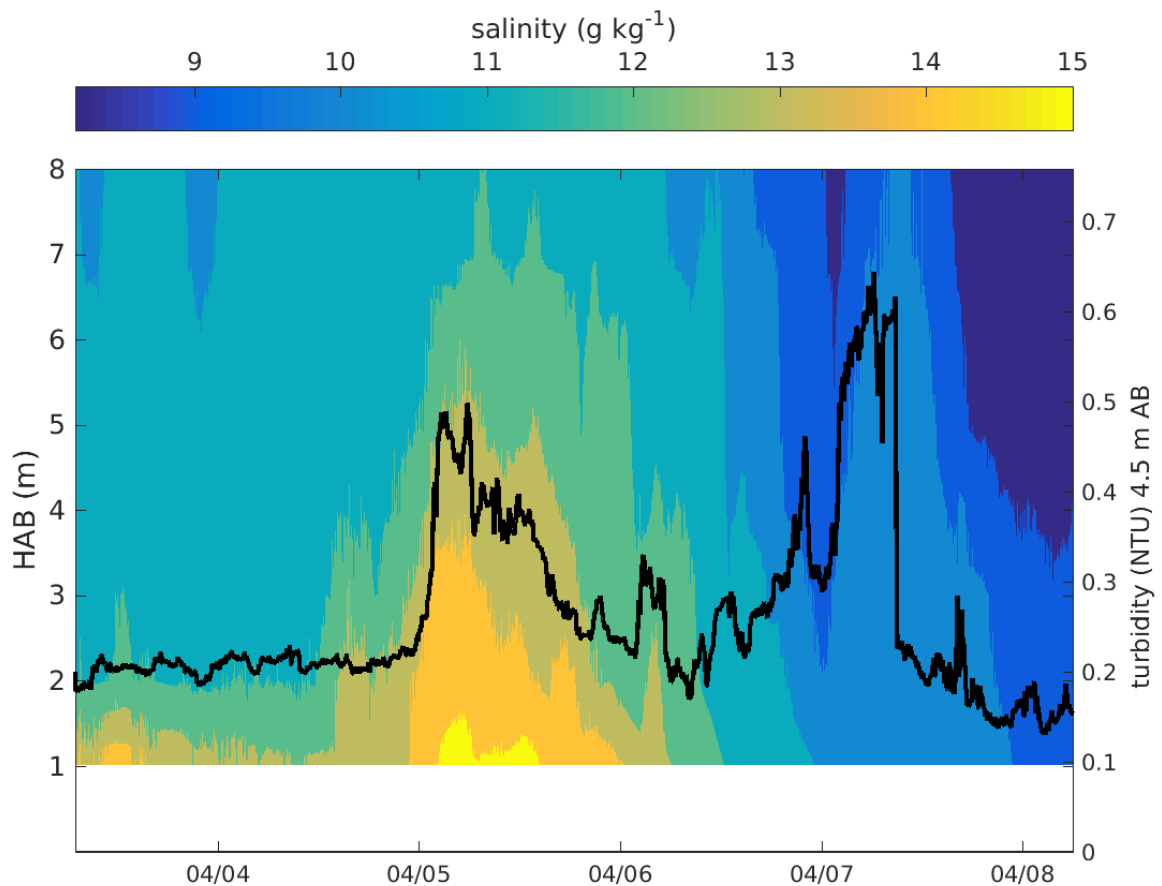


Figure 5.9.: Salinity data obtained from the CTD Chain deployed at TW during cruise AL434 (see Tab. 5.1).

5.5. Discussion

This study focuses on processes transporting sediment upslope from the deep basins back to shallower areas. It was found from microstructure measurements in the Arkona Basin, that in spite of the depth and therefore the unlikely occurrence of wave-induced resuspension, a layer of suspended fine-grained sediment is nearly permanently present near the bottom. This indicates that sediment transported into the basin is held in suspension or can be easily resuspended once deposited.

It was furthermore found that this turbid and turbulent BBL is present everywhere along the slope, confined by a regional halocline. This near bottom pool of saline water with high concentrations of suspended matter is not at rest, but may be advected up- and down the slope by upwelling events and inertial oscillations. Sediment originating from the deep parts of the basin can therefore be transported on-shore, at least temporarily, by a special kind of pumping mechanism. In the upwelling situation discussed above, the integrated near-bottom velocity yielded an up slope transport over a distance of more than 8 kilometers in less than 24 hours. Even though it cannot be proven from the data that suspended sediment advected together with the saline bottom water will be deposited in shallower areas, sediment dispersion across the rim of the basin is likely to happen. A fraction of the suspended sediment transported onshore from the deep part of the basin is sinking to the ground, whilst sediment in the shallower parts is resuspended and transported down the slope.

An indicator for sediment transport out of the basin and sediment dispersion across the slope is the distribution of mercury in this region. In the Arkona Basin, ammunition was dumped during World War II. This resulted in a heavy contamination of the sediment with mercury. As visible in Fig. 5.10, the dumping site in the eastern part of the Arkona Basin can be identified from mercury concentrations of over $400 \mu\text{g kg}^{-12}$. Near-bottom currents directed to the east are more pronounced in the Arkona Basin [Lass and Talpsepp 1993], which explains the spreading of mercury to the east. The cyclonic rim current can distribute contaminated sediment along the rim of the basin. But mercury concentrations are also enhanced in shallower parts of the basin, yielding that some fraction of the deposited sediment is also transported from deeper to shallower parts, across the isobaths. The observed upwelling event of the turbid BBL is a possible explanation for the dispersion of the sediment. The spreading of mercury

²High mercury concentrations in the fine fraction (Fig. 5.10b) southeast of the Arkona Basin originate from discharged water of the Oder river.

is even more pronounced in the fine fraction of sediment, which is easily resuspended and stays in suspension for a relatively long time.

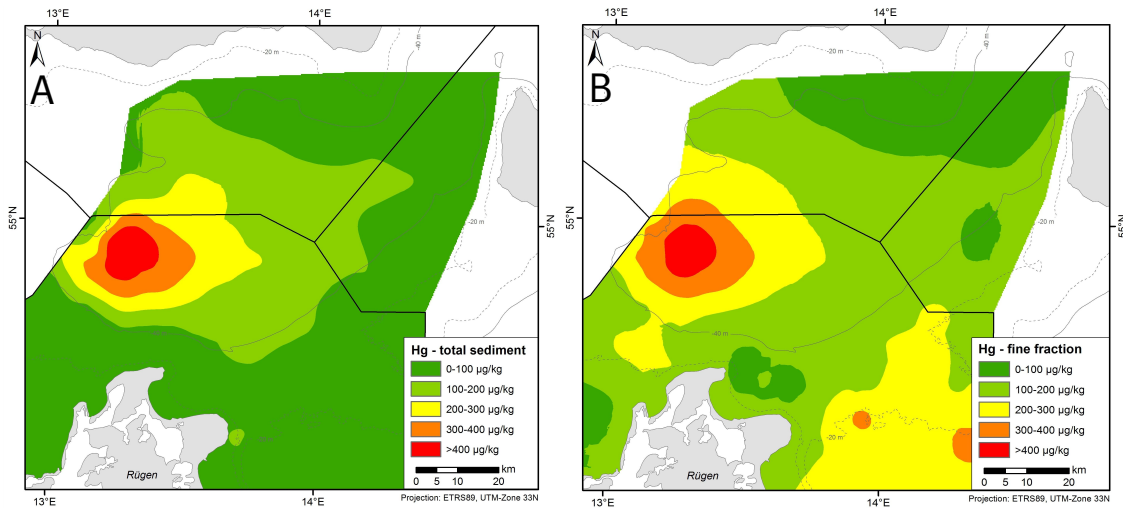


Figure 5.10.: Mercury concentration in (a) the total and (b) the fine fraction of the sediment [Leipe et al. 2016]. Figure courtesy of Michael Naumann, reprinted with permission.

The occurrence of residual sediment transport by slope-induced tidal straining here can not be determined from the data. Some evidence for the presence of this process come from the sediment distribution in the study area. The prerequisites, namely vertical stratification, sloping topography and an oscillatory current, are all present in the study area. From the non-dimensional description of the process in Schulz and Umlauf [2016], it can be inferred which settling velocity, and consequently which kind of sediment, is favored for up-slope transport. Sediment transport was found to be enhanced for non-dimensional settling velocities of $P = w_s/U = 10^{-2}$. Here, w_s is the settling velocity of suspended sediment and U the magnitude of the oscillatory flow. Cross-slope flow velocities are in the order of 0.1 m s^{-1} in this region [Lass and Talpsepp 1993, data from this study], suggesting that sediment with a settling velocity of $w_s = 10^{-3} \text{ m s}^{-1}$ is favored for up-slope transport under the conditions investigated in this study. After Stokes law, this settling velocity corresponds to medium to coarse silt. As visible in Fig. 5.4, this is exactly the sediment present in this area. On the cross-section from the deep parts of the basin southward to the coast, sediment distribution ranges from fine silt in the basin to coarse silt near the shore. Additionally, sorting of the sediment is slightly better near-shore than in the basin (Fig. 5.4). Nevertheless, it can only be speculated whether slope-induced tidal straining plays a role here.

5.6. Conclusions

One of the most important findings of this study is that sediment once deposited in the Arkona Basin can be transported back onshore. This suggests that fine-grained sediment from all the deep basins in the Baltic Sea, which are considered to be depositional, can be exported back to shallower areas. This has great implications for the distribution of pollutants, like the mercury originating from the ammunition dumping site in the Arkona Basin. Pollutants accumulated in the deep basins are not confined to remain there, but can spread towards shallower areas where they can endanger the local biosystem.

Several different mechanisms in the Arkona Basin cause sediment transport. Firstly, the mean flow of the cyclonic rim current transports suspended sediment across the basin along the rim and to the deeper parts. Secondly, upwelling tilts the bottom water pool towards the shore and saline water from the deep is advected up the basin slope, accompanied by suspended sediment originating from the deep parts of the basin. From the data, it can not be determine whether this advected sediment is deposited in the shallower parts, or if it disappears to the deeper areas again along with the saline water mass. But it is evident from the sediment and mercury distribution, that fine sediment from the deep parts of the basin is dispersed across the rim. Sediment pumping during upwelling events is one likely explanation for that.

Furthermore, near-inertial oscillations in cross-slope direction, which have been identified not only in our observations, can cause a residual sediment transport induces by asymmetries in stratification and consequently vertical turbulent mixing as described in Schulz and Umlauf [2016]. Observed slope angle and vertical density stratification are well within the range promoting up-slope sediment transport. Sediment distribution on the transect from basin to the coast is in agreement with the type of sediment (characterized by sediment settling velocity) favorable for up-slope transport under the observed conditions. Furthermore, the results found in section 3 suggest that a dominant along-slope velocity component, which is present here, does not hinder the residual up-slope sediment transport. However, the occurrence of residual sediment transport by slope-induced tidal straining can only be suspected and not be proven from the data.

Appendix A.

Numerical boundary conditions for SPM concentrations

In view of the strong near-bottom gradients of suspended material, the implementation of the boundary conditions for the SPM transport equation (2.12) requires special attention. While (2.14) provides an exact expression for the upward turbulent flux F_z at the bottom, the numerical implementation of the sinking flux,

$$F_s(z = 0) = w_s c_0 , \tag{A.1}$$

is not straightforward because the bottom concentration, c_0 , is unknown. In vertically staggered numerical grids typically used in ocean modeling, the bottom concentration c_0 has to be estimated from the known concentration c_1 in the center of the lowermost grid cell, which requires some assumptions about the vertical distribution of the suspended material in the near-bottom region. While it is reasonable to assume that the bottom cell is well mixed (i.e., $c_0 = c_1$) if the bed stress $|\tau_b|$ is smaller than the critical stress for erosion, τ_c , it is likely that the bottom concentration c_0 is significantly larger than c_1 if active erosion takes place ($|\tau_b| > \tau_c$). In this case, the popular assumption $c_0 = c_1$ may lead to large numerical errors, and to a grid dependence of the numerical solution. In the following, we show how a more consistent lower boundary condition can be derived.

We start from the observation that close to the bottom, the transport equation in (2.12) reduces to a balance between upward mixing and downward sinking of

suspended material,

$$0 = \nu_t^b \frac{\partial c}{\partial z} + w_s c, \quad (\text{A.2})$$

assuming small slopes ($\alpha \ll 1$) for simplicity. The turbulent viscosity in the near-bottom region is known to follow the law-of-the-wall relation $\nu_t = \kappa u_* (z + z_0)$, where $\kappa \approx 0.4$ is the von Kármán constant, and $u_* = |\tau_b|^{1/2}$ the bottom friction velocity [e.g., Pope 2000]. The turbulent diffusivity ν_t^b in this region is proportional to ν_t , and therefore adopts the form $\nu_t^b = Pr_t^{-1} \kappa u_* (z + z_0)$, where the turbulent Prandtl number, Pr_t , plays the role of a constant proportionality factor of order 1. The turbulence model used in our study has been shown to exactly reproduce this near-wall behavior for ν_t and ν_t^b [e.g., Umlauf and Burchard 2003, 2005].

Inserting the above law-of-the-wall relation for ν_t^b into (A.2), we find a solution of the form

$$\frac{c}{c_0} = \left(\frac{z}{z_0} + 1 \right)^{-p}, \quad (\text{A.3})$$

which is recognized as the classical Rouse profile [van Rijn 1984b], slightly modified here by the appearance of the turbulent Prandtl number in the definition of the Rouse number $p = w_s Pr_t / (\kappa u_*)$.

Recalling that in any conservative numerical scheme, c_1 represents the average concentration inside the lowermost grid cell, a relation between c_0 and c_1 may be found from integrating (A.3) across the cell. If we denote h as the cell thickness, this yields

$$c_0 = \frac{c_1}{r} \quad \text{for} \quad |\tau_b| > \tau_c, \quad (\text{A.4})$$

where

$$r = \frac{1}{(1-p)h/z_0} \left[\left(\frac{h}{z_0} + 1 \right)^{1-p} - 1 \right], \quad (\text{A.5})$$

Fig. A1 shows the ratio $r = c_1/c_0$ as a function of the normalized cell thickness h/z_0 for different Rouse numbers. The most important conclusion from this figure is that the naive approach of assuming $c_0 = c_1$ to compute the sinking flux in (A.1) during erosion periods introduces large numerical errors except for small Rouse numbers and/or extremely fine grids with $h \ll z_0$. Below, we nevertheless discuss some

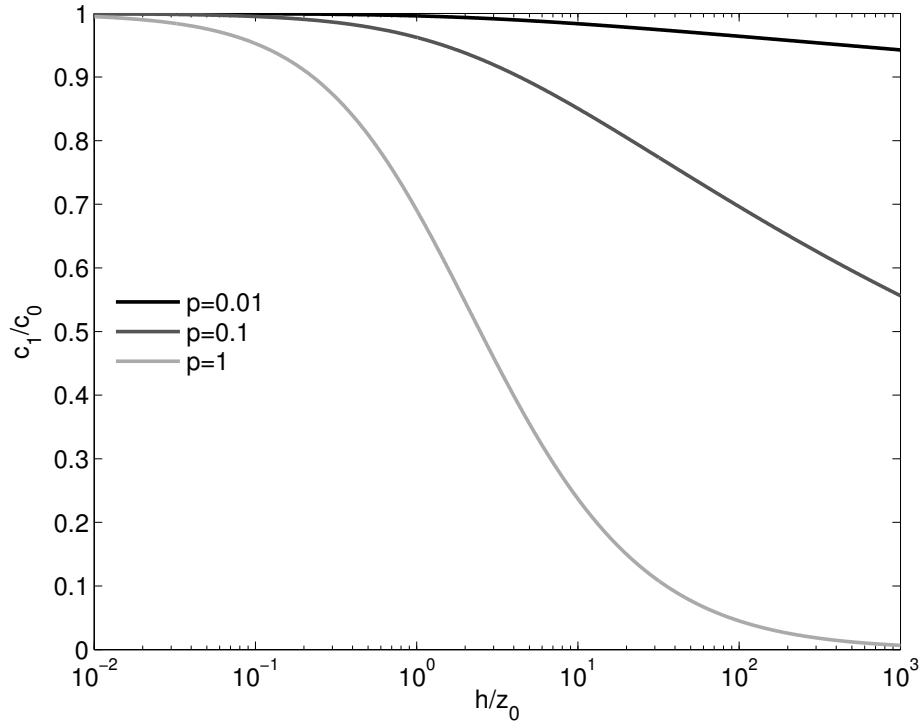


Figure A.1.: A1

Concentration ratio c_1/c_0 as a function of non-dimensional cell thickness, h/z_0 , for different Rouse numbers according to (A.4).

reference solutions that satisfy this condition. We note, however, that the constraint $h \ll z_0$ implies $\Delta t \ll z_0/w_s$ for the numerical time step according to the well-known CFL stability criterion for explicit advection schemes. It is easy to show that, even for idealized one-dimensional simulations, the numerical effort may become prohibitively large for small z_0 .

Using the example from Section 2.3 above, Fig. A2 illustrates that assuming $c_0 = c_1$ during both erosive and non-erosive periods leads to significant numerical errors, and to a grid-dependence of the results. Estimating c_0 based on (A.4) during periods with active erosion, however, removes this dependency on the numerical grid, and leads to stable results already for moderate vertical resolution. All results discussed in this manuscript are therefore based on this new expression. Convergence studies were carried out to insure that all our results are independent of the numerical grid size and time step.

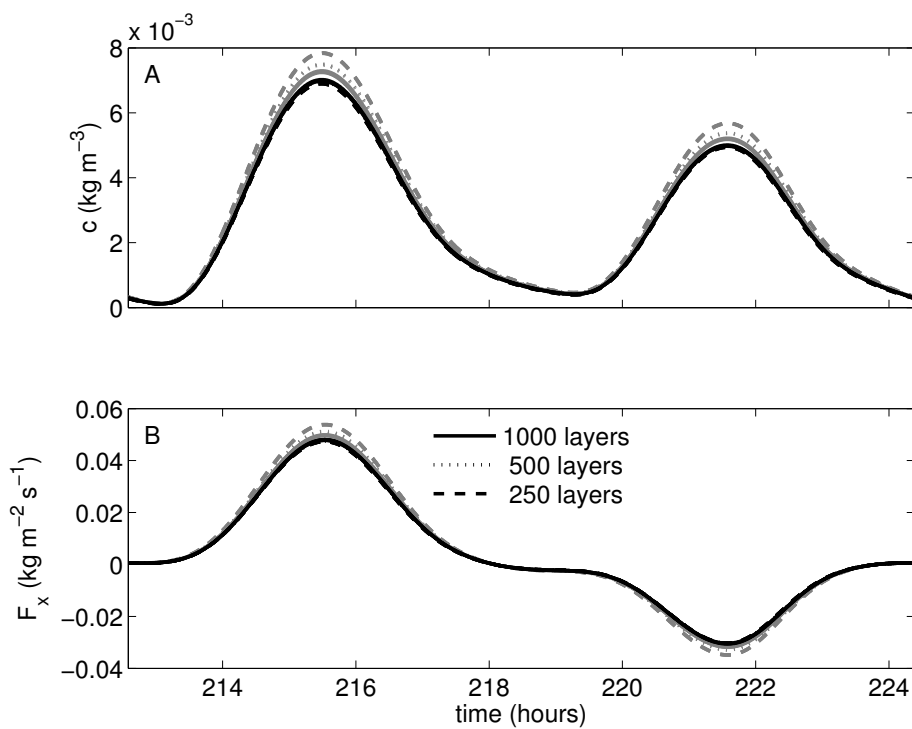


Figure A.2.: A2

Numerical results for (a) SPM concentration 5 m above the bottom, and (b) upslope flux F_x for three vertical resolutions. Gray lines are based on the assumption $c_0 = c_1$ to compute the sinking flux in (A.1), whereas black lines are based on (A.4) during erosive periods. Parameters correspond to Case 1 in Tab. 2.1.

Appendix B.

Sensitivity with respect to other model parameters (study in chapter 3)

Here, we briefly discuss the sensitivity of our model results with respect to variations in model parameters that have not been investigated in detail above. To this end, we individually vary selected parameters, leaving all other parameters at their reference values compiled in Tab. 3.1. The target parameter for this sensitivity study will be the BBL thickness that is the product of the complex interplay between mixing and re-stratification processes, and therefore provides a simple but useful proxy for overall model performance.

Fig. B.1a shows that a factor-2 increase or decrease of the slope angle only results in a small (around 10%) change in the computed BBL thickness. Possible uncertainties in the slope angle are therefore of minor importance for the predicted BBL thickness. A factor-2 increase or decrease in background stratification (Fig. B.1b), however, induces significant changes in the BBL thickness, with deviations of up to 30% from the reference value. As our estimate of N_∞^2 is based on the cross-slope buoyancy gradient $\partial b/\partial x$ (see section 3.4.2), which can be determined with good accuracy from our high-resolution density observations at position S, we believe that the actual uncertainty in this parameter is significantly smaller. The least known parameter in our computations is the bottom roughness z_0 that is varied in Fig. B.1c about the reference value $z_0 = 10^{-3}$ m. Doubling or halving z_0 modifies the BBL thickness by less than 10% with respect to the reference simulations, with a tendency for increasing BBL thicknesses if the bottom becomes rougher. We conclude that the uncertainties in our model parameters are unlikely to have a large effect on the modeled BBL thickness that, as shown above, is in good agreement with our data.

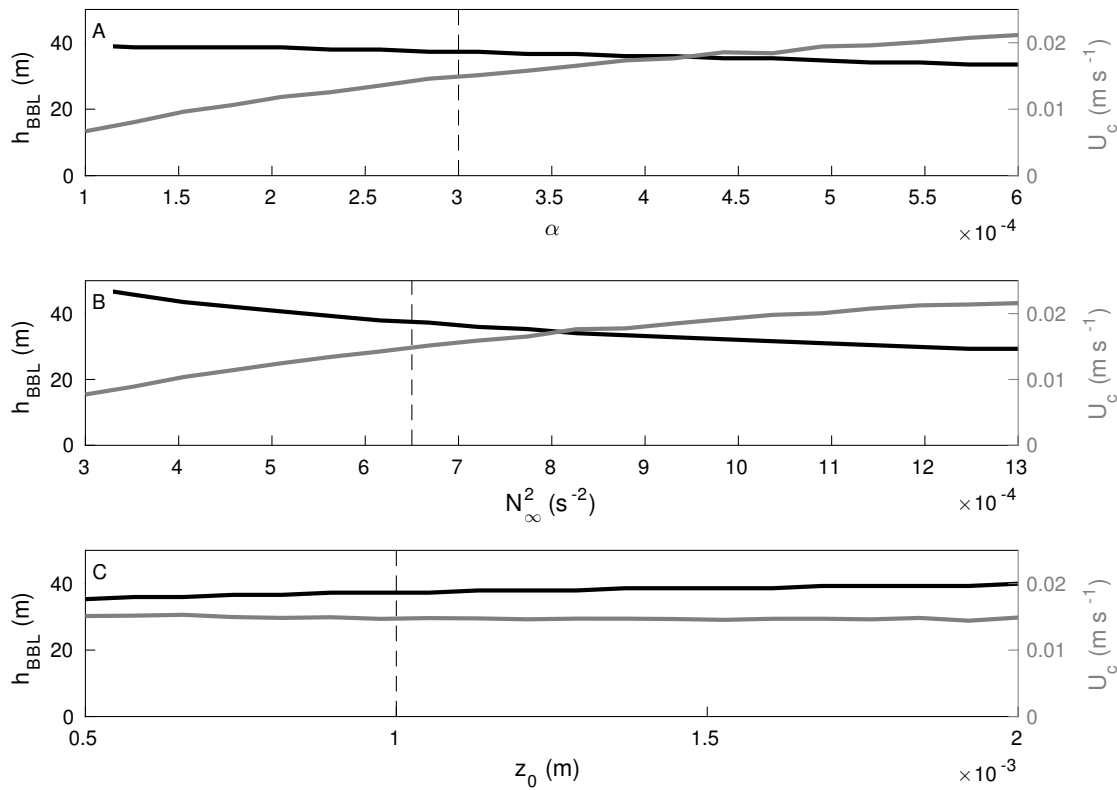


Figure B.1.: BBL thickness and bulk transport velocity as functions of (a) slope angle, (b) background stratification, and (c) bottom roughness. Standard parameters from Tab. 3.1 are indicated by vertical dashed lines.

While the above parameter variations only have a small to moderate impact on the BBL thicknesses, they do have a large influence on the SPM fluxes, here quantified with the help of the cross-slope transport velocity U_c . E.g., a 50% decrease in the standard value for α results in approximately the same reduction in the transport velocity (Fig. B.1a). A strong sensitivity is also found with respect to the background stratification (Fig. B.1b), and only variations in the bottom roughness show no significant effect on SPM transport (Fig. B.1c). Data to evaluate the significance of these variations with respect to U_c are not available.

Appendix C.

Second-order Turbulence Closure Models

In section 2 and 3, the General Ocean Turbulence Model (GOTM) was extensively used to investigate turbulence and vertical mixing over sloping topography. GOTM is a one-dimensional water-column model that solves the Reynolds-averaged Navier-Stokes equations using the Boussinesq approximation (density is treated as constant unless multiplied with the gravitational acceleration) and assumes pressure to be hydrostatic. The most important aspect of GOTM is, however, the choice of turbulence closure models.

In this appendix, a brief introduction into the basic principles and assumptions of turbulence modeling in oceanographic context is given. I will not explain the mathematical derivation of equations here, as this can be found in a broad variety of books and is beyond the scope of this thesis. This chapter rather aims at providing the reader with a general idea of the principles and the nomenclature of today's turbulence models and will therefore only contain mathematical equations when they support the readability.

At the end of this chapter, the turbulence model and the set of parameters used in sections 2 and 3 is outlined.

C.1. Introduction

Turbulence is a main contributor to mixing processes in the ocean and affects mean flow as well as particle movement and the spreading of tracers. Therefore, turbulence needs to be included in numerical ocean circulation models to some extent. Turbulent processes can be calculated with Direct Numerical Simulations (DNS), which solve the full Navier-Stokes equations, but the necessary resources and the computational costs exceed by far what is applicable in the simulation of realistic scenarios. For faster calculations, in Large Eddy Simulations (LES) only large-scale turbulence is resolved directly whilst the smaller scales are parameterized. With the progress in data processing and computers, LES has become more and more convenient to use, but is up to now still too expensive in terms of computational time for most applications. Therefore, turbulent fluxes have to be derived from quantities that can be calculated more efficiently. An important class of models for this problem are (second moments) one-point statistical closure models, which solve transport equations for the turbulent fluxes. As these transport equations introduce additional unknowns, physically reasonable closure assumptions must be made to ensure the existence of an accurate solution to the set of equations [Umlauf and Burchard 2005]. A second order model solves transport equations for the second moments of the turbulent fluctuations and assumes physically reasonable approximations for the higher-order statistical moments appearing in these equations. In a third order model, transport equations for these third-moment fluxes are derived and closures are assumed on the next level [e.g. in Sander 1998]. State of the art in ocean circulation models today are second order turbulence closures.

In all second order models that consider stratification and rotation effects, transport equations for the turbulent fluxes of momentum $\langle u'_i u'_j \rangle$ and buoyancy $\langle u'_i b' \rangle$ and a transport equation of the buoyancy variance $k_b = \langle b'^2 \rangle / 2$ are derived. Here, u_i are the velocity components, b denotes the buoyancy and $\langle \cdot \rangle$ the Reynolds average. The prime $'$ indicates the deviation from the Reynolds average, similar to the notation in section 2 and 3. As the obtained equations are directly derived from the Navier-Stokes equations, all terms appearing have a clear interpretation and can be compared to data (e.g. microstructure turbulence, high resolution acoustic velocity measurements) or the results of other models.

C.2. Pressure Redistribution Models

One new term in the flux of momentum $\langle u'_i u'_j \rangle$ transport equation is the pressure–strain correlation Φ_{ij} , which determines how energy is distributed among the components $\langle u_i u_j \rangle$. The closure for this quantity is the most crucial assumption that has to be made in turbulence models. General and commonly used models for the explicit calculation of Φ_{ij} are pressure redistribution models. These models are based on the tendency of unforced turbulence to be isotropic, whereas straining effects and buoyancy tend to induce anisotropy. Most of the pressure-redistribution models only differ in the choice of parameters in this equation. For the corresponding term that appears in the transport equation for buoyancy fluxes, $\langle u'_i b' \rangle$, the pressure–buoyancy–gradient correlation Φ_i^b , other explicit models exist that relate the tendency for isotropic turbulence and the effects of shear and stratification with the use of several empirical coefficients. TALK TO LARS ABOUT: Although these pressure redistribution models are relatively simple, they still require too much computational time for the application in ocean circulation models.

C.3. Explicit Algebraic Models

For a operational turbulence parametrization, the model assumptions described above have to be further simplified to obtain fully explicit expressions for the turbulent fluxes that can easily be solved. An explicit equation in this context means that only quantities calculated in the last computational time step are used for calculations. These are the explicit algebraic models. Under the assumption that the production of turbulence by buoyancy and shear is in equilibrium with dissipation of turbulence by viscous effects, the transport equations for the turbulent fluxes greatly simplify and can be solved analytically. Assuming further that timescales of horizontal advection and diffusion are much larger than the vertical timescales, the so-called boundary layer assumption, the (vertical) fluxes of momentum and buoyancy turn out to be

$$\langle u'w' \rangle = -\nu_t \partial_z u \quad (\text{C.1})$$

$$\langle v'w' \rangle = -\nu_t \partial_z v \quad (\text{C.2})$$

$$\langle w'b' \rangle = -\nu'_t \partial_z b \quad (\text{C.3})$$

with u, v, w being the three velocity components and z the vertical coordinate. ν_t and ν'_t are called the turbulent or eddy viscosity and diffusivity, respectively. They depend on the turbulent kinetic energy k and the turbulent length scale l according to

$$\nu_t = c_\mu \sqrt{k} l, \quad \nu'_t = c'_\mu \sqrt{k} l. \quad (\text{C.4})$$

Here, c_μ and c'_μ are non-dimensional stability functions [Burchard et al. 1999]. These stability function contains the essence of the closure model (and therefore the model parameters introduced with these models).

Consequently, calculation of turbulent fluxes only depends on the gradient of the transported quantity itself and ν_t and ν'_t . The the unknowns left for the calculation of turbulent viscosity and diffusivity are the turbulent kinetic energy k , the length scale l and the stability functions. They can all be derived independently, as outlined in the following sections.

C.4. Closure for k

The turbulent kinetic energy is defined as

$$k = \frac{\langle u'_i u'_i \rangle}{2} \quad (\text{C.5})$$

and the following transport equation for k can be derived from the Navier-Stokes equations [Rodi 1993], under the assumptions of negligible horizontal diffusion and negligible advection, horizontal as well as vertical

$$\partial_t k - \partial_z (\nu_k \partial_z k) = P + B - \varepsilon. \quad (\text{C.6})$$

Terms on the right hand site are the shear and buoyancy production

$$P = \nu_t M^2, \quad B = -\nu'_t N^2, \quad (\text{C.7})$$

depending on the shear and buoyancy frequency

$$M^2 = (\partial_z u)^2 + (\partial_z v)^2, \quad N^2 = \partial_z b, \quad (\text{C.8})$$

respectively. ε denotes the turbulent dissipation (see next sections). The calculation of the turbulent diffusivity ν_k depends on the choice of the turbulence closure model. Different boundary conditions for (C.6) at the bottom and surface can be derived from the logarithmic law of the wall and under the assumptions that $P = \varepsilon$ [Burchard et al. 1999].

Most coastal ocean models either solve a simplified form of this transport equation or assume local equilibrium between shear and buoyancy production and dissipation of turbulent fluxes ($P + B = \varepsilon$). Under this assumption, an explicit formula for k can be derived that includes shear and buoyancy frequencies and stability functions values only from the last time step [Umlauf and Burchard 2005]:

$$k = (c_\mu^0)^{-3}(c_\mu M^2 - c'_\mu N^2)l^2, \quad (\text{C.9})$$

with c_μ^0 being a constant. To avoid unreasonable negative values for k , a lower limit k_{\min} is prescribed.

C.5. Closure for l or ε

Whilst the closure for k is rather straight forward, the closure for the length scale l is highly under discussion. The problem of determining l is equivalent to determining the turbulent dissipation rate ε , via the cascading relation [Umlauf and Burchard 2005]

$$\varepsilon \sim k^{3/2}l^{-1}. \quad (\text{C.10})$$

A simple and very famous model is the Blackadar [1962] formula:

$$\frac{1}{l} = \left(\frac{1}{(\kappa(d_s + z_0^s))} + \frac{1}{\kappa(d_b + z_0^b)} + \frac{1}{l_a} \right). \quad (\text{C.11})$$

d_s , d_b , z_0^s , z_0^b are the distances from surface and bottom and the corresponding roughness lengths, respectively. l_a depends on vertically integrated values of $k^{1/2}$ or is set to a fraction of the water depth. This model has some disadvantages: Firstly, it depends on dimensional constants and coordinates and hence the reference system, what should be avoided in turbulence modeling. Secondly, it fails for example in cases of stably stratified flows and is inapplicable if the problem considered includes no bound-

aries at surface or bottom. The problems in stably stratified flows can be reduced by clipping the length scale at a certain maximum. Unfortunately, model results in some cases are very sensitive to a constant included in this clipping [Umlauf and Burchard 2005].

Another way to obtain a closure is to derive another transport equation for l (or ε). Several different approaches have been established that showed good performance in many applications: Mellor and Yamada [1982] suggested a transport equation for the product of k and l , Burchard and Baumert [1995] one for the dissipation rate. Wilcox et al. [1998] formulated a transport equation for $\omega = \varepsilon/k$, which turned out to be a great amendment especially in the modeling of turbulence under breaking waves. To generalize all these different models, Umlauf and Burchard [2003] suggested a generic transport equation for arbitrary fractions of k and l :

$$\partial_t(k^m l^n) - \partial_z \left(\frac{\nu_t}{\sigma_{mn}} \partial_z(k^m l^n) \right) = k^{m-1} l^n (c_{mn1} P + c_{mn3} B - c_{mn2} \varepsilon). \quad (\text{C.12})$$

The choice of m and n determines the model, e.g. with $m = 3/2$ and $n = -1$, (C.12) becomes the ε -equation in Burchard and Baumert [1995] (note that $\varepsilon \sim k^{3/2} l^{-1}$, see (C.10)). σ_{mn} is constant, but depends on the chosen model. The formulation of this generic transport equation allows more direct comparison of different established turbulence models and can furthermore be used to derive new turbulence models, provided that the determination of the necessary parameters is constrained, such that the model behavior is controlled.

A clipping for ε can be applied to improve the performance in stably stratified flows, derived from the findings of [Galperin et al. 1988]:

$$\varepsilon_{\text{lim}} = (c_\mu^0)^{3/4} \frac{kN}{\sqrt{2}c_{\text{lim}}}. \quad (\text{C.13})$$

C.5.1. Calculation of c_{mn3}

Under stable stratification, the model parameter c_{mn3} mentioned in the last section was found to depend on the steady-state Richardson number Ri_{st} . The turbulent Richardson number is defined as $Ri = N^2/M^2$, and the steady-state Richardson number indicates equilibrium $P + B = \varepsilon$ in homogeneous turbulence and was experimentally determined to be around 0.25 [Umlauf and Burchard 2005]. c_{mn3} is then calculated

via

$$c_{mn3} = c_{mn2} - (c_{mn1} - c_{mn2}) \frac{c_\mu(Ri_{st})}{c'_\mu(Ri_{st})} \frac{1}{Ri_{st}}. \quad (\text{C.14})$$

For unstable stratification, $c_{mn3} = 1.0$ is used [Rodi 1987]. Umlauf and Burchard [2005] showed that Ri_{st} , and thus c_{mn3} determines the entrainment velocity in stratified boundary layers, which is essential for the process investigated in chapters 2 and 3.

C.6. Stability functions

The stability functions follow directly from the (closed) second-moment equations. Depending on the assumptions in the turbulence closure, the stability functions c_μ and c'_μ include constant formulations or simple dependences on the Richardson number for highly simplified turbulence closures. More general assumptions in the turbulence closure lead to rational stability functions depending on the non-dimensional shear and buoyancy number, $\alpha_M = \tau^2 M^2$ and $\alpha_N = \tau^2 N^2$, where $\tau = k/\varepsilon$ is the turbulent time scale. Coefficients are calculated from the prescribed set of parameters that determine the pressure–redistribution model.

Please note that the Richardson number in the last section is $Ri = N^2/M^2$, and the stability functions therefore can be evaluated for Ri_{st} .

C.7. Parameters for the Turbulence Model

For the calculations carried out in section 2 and 3, we chose a $k - \varepsilon$ style dynamic equation.

The lower boundary condition for the transport equation (C.6) is a no-flux condition derived from the assumption $P = \varepsilon$:

$$\nu_k \partial_z k = 0, \quad z = 0. \quad (\text{C.15})$$

The turbulent diffusivity ν_k involved in (C.6) is set to $\nu_k = \nu_t$ and values for the other parameters are found in Tab. C.1

The ε -equation is obtained from the generic equation in (C.12) with $m = 3/2$ and $n = -1$

$$\partial_t \varepsilon - \partial_z (\nu_\varepsilon \partial_z \varepsilon) = \frac{\varepsilon}{k} (c_{\varepsilon 1} P + c_{\varepsilon 3} B - c_{\varepsilon 2} \varepsilon), \quad (\text{C.16})$$

and with $\nu_\varepsilon = \nu_t / \sigma_\varepsilon$. Values of the parameters are summarized in Tab. C.1. At the bottom, again a flux boundary condition is imposed:

$$\frac{\nu_t}{\sigma_\varepsilon} \partial_{\tilde{z}} \varepsilon = -(c_\mu^0)^3 \frac{\nu_t}{\sigma_\varepsilon} \frac{k^{3/2}}{\kappa(\tilde{z} + z_0)}, \quad (\text{C.17})$$

with \tilde{z} denoting the distance from the bottom, z_0 the bottom roughness and κ the van Karman constant.

For the calculation of the coefficients for the stability functions and c_μ^0 , the parameter set found in Canuto et al. [2001], version A, was used.

k_{\min}	σ_ε	$c_{\varepsilon 1}$	$c_{\varepsilon 2}$	Ri_{st}	c_{\lim}
10^{-12}	1.3	1.44	1.92	0.25	0.27

Figure C.1.: Parameters for the turbulence model used in section 2 and 3.

Appendix D.

State of the art wind wave modeling

In this appendix, supplementary information about wind wave generation and evolution is given, followed by a discussion of the third generation wave model SWAN, including the latest findings to improve the theory.

D.1. Evolution of Waves

The spectrum of vertical motions of the ocean surface consists of several types of waves, covering a broad frequency range. Wind generated waves have periods around 0.25 – 30 s. Locally generated waves, called wind sea, are irregular and short crested. While propagating away from the generation area, they become long crested and more regular, their periods increase. These waves are called swell [Holthuijsen 2007].

D.1.1. Wave Generation by Wind

Energy is transferred from wind to the waves by wind-induced surface pressure fluctuations. Under the assumption of a harmonic wave propagating in the same direction as the (faster) wind blows, the wind field near the water surface is disturbed as indicated in Fig. D.1. Higher air pressure is induced at the windward site of the wave crest, where the water surface moves downwards while the wave is propagating, and vice versa low air pressure at the leeward site of the wave crest, where the sea surface is moving upwards.

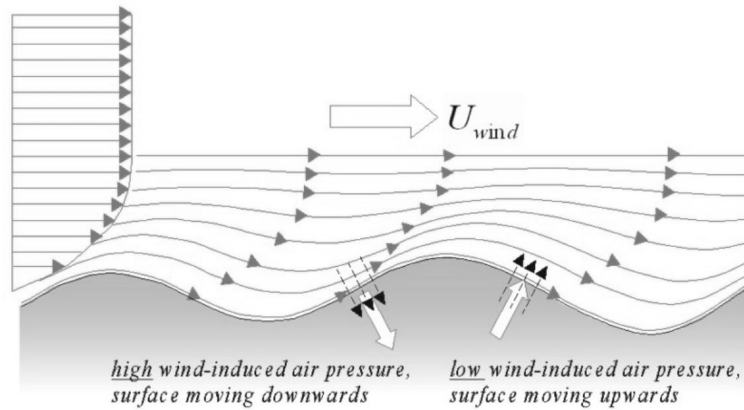


Figure D.1.: Wind-pressure distortions over a propagating harmonic wave. Figure taken from Holthuijsen [2007].

This way, the (wave-induced) air pressure distortions amplify the vertical movement of the water surface, transferring energy from wind to the wave field. This process enforces itself as it is more effective for higher waves. Wave growth ends when the wave propagation speed approaches wind speed. It is not well understood how initial distortions of the sea surface are generated, but fortunately wave growth is not sensitive to the initial wave field.

Wave Growth Limitation

Wave growth (in deep water) is not only limited by the wind speed U_{10} , as mentioned above, but also by the time that wind has been blowing and the distance to the coast where the wind comes from. This distance is called fetch, and wave height increases the longer the fetch is. Wind duration and fetch can be combined to the equivalent fetch, assuming that from the moment on that the wind started, a wave component with group velocity c_g has travelled a certain distance in wind direction. Wind transfers the same energy to the wave component either over a time t or (for an infinitely long time period) over a distance

$$F_{eq} = c_g t \cos \theta, \quad (D.1)$$

where θ is the wave propagation direction relative to the wind direction. This distance is called the equivalent fetch. Sea states where real fetch is shorter (longer) than the equivalent one are called fetch-limited (duration-limited). At fully developed sea

states, the wave phase speed (at some peak frequency) has approached U_{10} and wave growth decays.

D.1.2. Wave-wave Interaction

Energy can be transferred between wave components by resonance. This happens, if two pairs of waves have the same frequency, wave number vector and direction. A pair of waves is a superposition of two waves of different frequencies and wave number vectors, which visually form a diamond pattern (Fig. D.2).

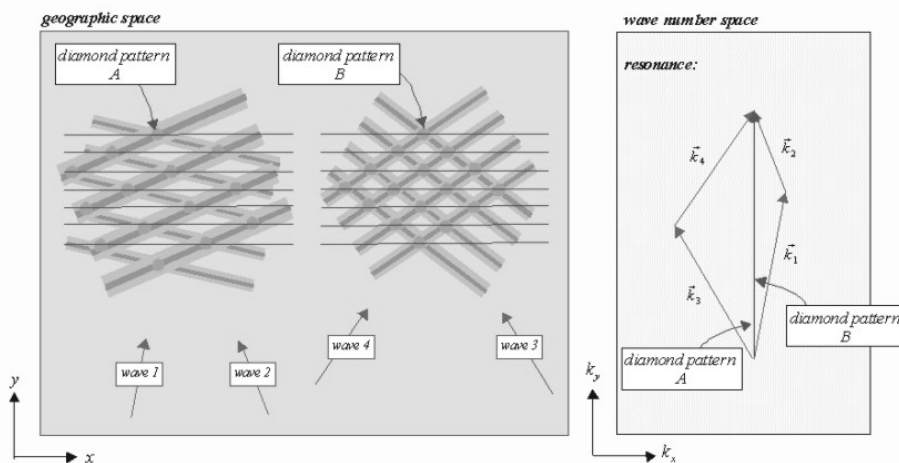


Figure D.2.: Two pairs of waves, each creating a diamond pattern, fulfill the resonance conditions for quadruplet wave-wave interaction. Figure taken from Holthuijsen [2007].

If two of those diamond patterns fulfill the resonance conditions, energy can be distributed among the four waves involved. This mechanism is called quadruplet wave-wave interaction. It draws energy from the mid-range frequencies and provides it to waves with rather high or low frequencies.

In shallow water (non-dispersive waves), triad wave-wave interaction is possible, where a pair of waves fulfills the above resonance conditions with a third wave. In deep water, the required resonance conditions cannot be fulfilled because of the dispersion relationship.

D.1.3. Dissipation of Energy

Wave energy can be dissipated either by white-capping in deep water, or by bottom friction and depth-induced breaking in the surf zone.

White-capping describes the breaking of waves in deep water. This is a highly non-linear process which is not understood in detail. Presumably, wave steepness and local wind affect the occurrence of white-caps, which draw energy from waves at frequencies by hindering the upward movement of the sea surface. The dissipative effect of white-capping is rather weak.

D.2. Sea State Description

The most important method to describe a sea state is to treat ocean waves as a stochastic process to calculate a wave spectrum, from which parameters like wave height are derived. One possibility therefore is the random-phase/amplitude model, described in detail in Holthuijsen [2007]: The time series of surface elevation $\eta(t)$ is assumed to be a superposition of N sinusoidal waves, each with a distinct frequency f_i , amplitude a_i and phase α_i , written as

$$\eta(t) = \sum_{i=1}^N a_i \cos(2\pi f_i t + \alpha_i). \quad (\text{D.2})$$

Considering a_i and α_i to be independent random variables, probability density functions for both can be derived from observations. For waves in sufficiently deep water which are not too steep, it was found that the phase is uniformly distributed (and can therefore be omitted in the wave spectrum), while the amplitude is Rayleigh distributed with expected value $E\{a_i\} = \mu_i$ for each frequency f_i . The function $f_i \rightarrow E\{a_i\}$ is called the amplitude spectrum and already contains all (non-directional) information of the sea state. A more meaningful characterization is, however, the variance spectrum $f_i \rightarrow E\{a_i^2/2\}$, as the variance is proportional to the wave energy contained in each frequency, with the proportionality constant ρg . Here, ρ denotes density of the water and g the gravitational acceleration. By scaling the variance of each discrete frequency with the frequency bin Δf (i.e. the size of the frequency resolution) and formally assuming infinitely small frequency bins, the variance density spectrum

is obtained. Multiplied by the factor ρg , this is the energy density spectrum:

$$E(f) = \rho g \lim_{\Delta f \rightarrow 0} \frac{1}{\Delta f} E\left\{\frac{1}{2}a_i^2\right\}. \quad (\text{D.3})$$

For a harmonic wave, i.e. all wave energy is contained in one distinct frequency, $E(f)$ reduces to a delta distribution. For more irregular waves, the energy density spectrum broadens.

The shape of this spectrum is not at all arbitrary, but was found to have rather uniform characteristics under similar conditions. For a fully developed sea state, the Pierson-Moskowitz (PM) spectrum was derived:

$$E_{PM}(f) = \underbrace{\alpha_{PM} g^2 (2\pi)^{-4} f^{-5}}_{f^{-5}\text{-tail}} \underbrace{\exp\left[-\frac{5}{4} \left(\frac{f}{f_{PM}}\right)^{-4}\right]}_{\text{low-freq. cut-off}}. \quad (\text{D.4})$$

The f^{-5} - tail comes from a dimensional argument under the assumption, that wave breaking limits the spectra on the high frequency side, and that this process is determined only by the gravitational acceleration and the wave frequency itself. Therefore, $E(f) \sim g^2 f^{-5}$ at high frequencies. At a peak frequency f_{PM} , depending on the wind speed, a smooth low-frequency cut-off is imposed. From observations, an energy scale of $\alpha_{PM} = 0.0081$ was derived.

The PM spectrum describes a fully developed sea state, i.e. constant wind conditions being present until sea state becomes stationary and no fetch limitation is assumed. Observed sea states rarely fulfill these assumptions, and during an extensive study, the JONSWAP (Joint North Sea wave Project, Hasselmann [1974]) spectrum for young sea states was designed:

$$E_{JONSWAP}(f) = \underbrace{\alpha g^2 (2\pi)^{-4} f^{-5}}_{\text{PM shape}} \underbrace{\exp\left[-\frac{5}{4} \left(\frac{f}{f_{\text{peak}}}\right)^{-4}\right]}_{G(f)} \underbrace{\exp\left[-\frac{1}{2} \left(\frac{f}{\sigma f_{\text{peak}}}\right)^2\right]}_{\gamma}. \quad (\text{D.5})$$

Here, the PM spectrum was down-scaled with a higher peak frequency f_{peak} and a smaller energy scale α (which depends on the f_{peak} now) to maintain the shape of the PM spectrum. $G(f)$ is a peak enhancement function, which amplifies and narrows the spectrum around the peak frequency. Hereby, γ and σ control height and width of the peak, respectively.

The JONSWAP spectrum was found to be a good generalization of observed wave energy spectra, not only for idealized fetch-limited conditions but also for arbitrary wind conditions. Reason for that is that wave-wave interaction (see above) distributes energy among wave frequencies in a way that stabilizes the shape of the JONSWAP spectrum.

The energy spectra discussed above are one dimensional, only depending on wave frequency. No information about the propagation direction of waves are included. To completely describe a sea state, the energy spectrum $E(f, \theta)$ has to be extended by informations about how energy is distributed among waves traveling in propagation direction θ .

D.3. Third Generation Wave Model SWAN

The open source wave model SWAN, an acronym for **S**imulating **W**AVes **N**earshore, is a wave model optimized for applications in coastal waters. As the spatial resolution of model domains in coastal regions is often very fine to capture smaller features in topography, SWAN has an implicit propagation scheme implemented, assuring numerical stability even for timesteps, that violate the CFL criterion.

The central equation that is solved for every timestep at every grid point is the action balance equation, that accounts not only for the energy distributions in the wave frequency space but also for frequency shifts by wave-current interaction. The action density $N = N(\sigma, \theta; x, y, t)$ is therefore dependent on the relative radian frequency σ , which is the shifted frequency in a system moving with the current:

$$\frac{\partial N}{\partial t} + \frac{\partial c_{g,x}N}{\partial x} + \frac{\partial c_{g,y}N}{\partial y} + \frac{\partial c_{\theta}N}{\partial \theta} + \frac{\partial c_{\sigma}N}{\partial \sigma} = \frac{S_{in} + S_{nl} + S_{wc}}{\sigma}, \quad (\text{D.6})$$

where the source terms on the right hand side refers to energy input by wind, nonlinear wave – wave interaction and energy dissipation by white capping. t, x, y are time and spatial directions, θ is the direction of wave energy propagation and $c_{g,x}, c_{g,y}$ are the group speed in each spatial direction. The fifth term on the left had side represents the frequency shift by ambient currents.

In the absence of currents, this action balance equation reduces to the energy balance equation.

$$\frac{\partial E}{\partial t} + \frac{\partial c_{g,x} E}{\partial x} + \frac{\partial c_{g,y} E}{\partial y} + \frac{\partial c_{\theta} E}{\partial \theta} = S_{in} + S_{nl} + S_{wc}. \quad (\text{D.7})$$

All equations in the following will be noted, consistent with the action balance equation, in terms of the relative radian frequency σ . Although various formulations for the different mechanisms below are implemented in SWAN, only the ones used in the setup for the Baltic Sea in chapter 4.2 are described.

D.3.1. Wave generation by wind

Wind data is provided to the model as the wind speed and direction at 10 m elevation, U_{10} . This value is converted to a friction velocity via

$$u_*^2 = C_D U_{10}^2. \quad (\text{D.8})$$

Before version 41.01 of SWAN, the wind drag coefficient was linearly dependent on the wind speed with an imposed lower limit. This formulation was found to overestimate C_D for strong winds. Therefore, Zijlema et al. [2012] fitted a second-order polynomial to nearly 5000 observed wind drag coefficients in dependence of the wind speed and came up with

$$C_D = \left(0.55 + 2.97 \frac{U_{10}}{U_{ref}} - 1.49 \left(\frac{U_{10}}{U_{ref}} \right)^2 \right) \times 10^{-3}, \quad (\text{D.9})$$

where $U_{ref} = 31.5 \text{ m s}^{-1}$ is the wind speed at which C_D is maximal.

The source term for energy input by wind includes two mechanisms:

$$S_{in}(f, \theta) = \alpha + \beta E(f, \theta), \quad (\text{D.10})$$

where α is the initial wave growth, parameterized with the following empirical expression by Cavaleri and Malanotte–Rizzoli

$$\alpha = \begin{cases} \frac{1.5 \cdot 10^{-3}}{g^2 2\pi} (u_* \cos(\theta - \theta_{wind}))^4 G & \text{for } |\theta - \theta_{wind}| \leq 90^\circ \\ 0 & \text{for } |\theta - \theta_{wind}| > 90^\circ \end{cases} \quad (\text{D.11})$$

where G is a cut-off function to avoid wave growth at frequencies below the Pierson–Moskowitz frequency, g the gravitational acceleration and θ_{wind} is the wind direction.

Another implemented approach to quantify the initial wave growth is to impose the JONSWAP spectrum for young sea states. The non-dimensional peak wave frequency $\tilde{f}_{peak} = f_{peak} U_{10}/g$ is thereby derived using the spatial step size at each point as fetch F with an empirical equation by Kahma and Calkoen [1992] for short fetch lengths:

$$\tilde{f}_{peak} = 2.18 \tilde{F}^{-0.27}, \quad (\text{D.12})$$

where $\tilde{F} = gF/U_{10}^2$. All other coefficients in the JONSWAP energy spectrum equation are derived from this peak frequency [Holthuijsen 2007], and wave directions are assumed to be \cos^2 distributed.

For the exponential wave growth term β in (D.10) the classical expression of [Komen et al. 1984] is used:

$$\beta = \max\left\{0, 0.25 \frac{\rho_{air}}{\rho_{water}} \left[28 \frac{u_*}{c} \cos(\theta - \theta_{wind}) - 1\right]\right\} \sigma, \quad (\text{D.13})$$

with the phase velocity c and ρ_{air} and ρ_{water} the densities of air and water.

D.3.2. Nonlinear wave – wave interaction

The calculation of quadruplet wave-wave interaction requires large computational resources because of the high number of possible quadruplet constellations. It is calculated with the discrete-interaction approximation (DIA) by [Hasselmann and Hasselmann 1985]. Only two constellations of wave quadruplets are considered to interact.

The frequencies must fulfill

$$\begin{aligned}\sigma_1 &= \sigma_2 = \sigma \\ \sigma_3 &= 1.25\sigma = \sigma^+ \\ \sigma_4 &= 0.75\sigma = \sigma^-\end{aligned}$$

The wave directions must be equal for the waves with frequency σ , while the waves with frequencies σ_3 and σ_4 lie at angles of $\theta_1 = -11.5^\circ$ [or $\theta_1 = 11.5^\circ$] and $\theta_2 = 33.6^\circ$ [or $\theta_2 = -33.6^\circ$] to them. The contribution for each quadruplet to the source term S_{nl} in Eq. (D.7) is:

$$S_{nl4}^*(\sigma, \theta) = 2\delta S_{nl4}(\alpha_1\sigma, \theta) - \delta S_{nl4}(\alpha_2\sigma, \theta) - \delta S_{nl4}(\alpha_3\sigma, \theta), \quad (\text{D.14})$$

where for $i \in \{1, 2, 3\}$

$$\begin{aligned}\delta S_{nl4}(\alpha_i\sigma, \theta) &= 2.12 \cdot 10^{(-4)}\sigma^{11} \cdot [(0.41E(\alpha_i\sigma^+, \theta)E^2(\alpha_i\sigma, \theta) \\ &+ 3.16E(\alpha_i\sigma^-, \theta)) - 54.6E(\alpha_i\sigma, \theta)E(\alpha_i\sigma^+, \theta)E^2(\alpha_i\sigma^-, \theta)].\end{aligned}$$

The coefficients are $\alpha_1 = 1$, $\alpha_2 = 1.25$, $\alpha_3 = 0.75$.

The above holds for infinite water depth and must be multiplied with a scaling factor

$$R(\tilde{k}d) = \max\left\{1 + \frac{22}{3}\tilde{k}d \left(1 - \frac{6}{7}\tilde{k}d\right) \times \exp(-1.25\tilde{k}d), 4.43\right\}, \quad (\text{D.15})$$

depending on the mean wave number \tilde{k} and the the water depth d to obtain the finite depth contribution to the source term for nonlinear wave – wave interaction.

D.3.3. Dissipation

Wave energy is dissipated by white – capping. The representation of this process originates from [Hasselmann 1974]:

$$S_{wc}(\sigma, \theta) = -2.36 \cdot 10^{-5} \frac{k}{\tilde{k}} \left(\frac{\tilde{s}}{\tilde{s}_{PM}}\right)^4 \frac{\tilde{\sigma}}{\tilde{k}} k E(\sigma, \theta), \quad (\text{D.16})$$

with $\tilde{s} = \tilde{k}\sqrt{m_0}$ being the overall wave steepness, k the wave number, $\tilde{\sigma}$ the mean wave frequency and $\tilde{s}_{PM} = \sqrt{3.02 \times 10^{-3}}$ the overall wave steepness of the Pierson – Moskowitz spectrum.

Bibliography

- Amoudry, L. O., and A. J. Souza, 2011: Impact of sediment-induced stratification and turbulence closures on sediment transport and morphological modelling. *Cont. Shelf Res.*, **31** (9), 912–928.
- Becherer, J., and L. Umlauf, 2011: Boundary mixing in lakes. 1. Modeling the effect of shear-induced convection. *J. Geophys. Res.*, **116**, C10017, doi:10.1029/2011JC007119.
- Blackadar, A. K., 1962: The vertical distribution of wind and turbulent exchange in a neutral atmosphere. *J. Geophys. Res.*, **67** (8), 3095–3102.
- Burchard, H., and H. Baumert, 1995: On the performance of a mixed-layer model based on the κ - ϵ turbulence closure. *J. Geophys. Res. C: Oceans*, **100** (C5), 8523–8540.
- Burchard, H., K. Bolding, T. P. Rippeth, A. Stips, J. H. Simpson, and J. Sündermann, 2002: Microstructure of turbulence in the northern North Sea: A comparative study of observations and model simulations. *J. Sea Res.*, **47**, 223–238.
- Burchard, H., K. Bolding, and M. R. Villarreal, 1999: *GOTM, a general ocean turbulence model: theory, implementation and test cases*. Space Applications Institute.
- Burchard, H., and R. D. Hetland, 2010: Quantifying the contributions of tidal straining and gravitational circulation to residual circulation in periodically stratified tidal estuaries. *J. Phys. Oceanogr.*, **40** (6), 1243–1262.
- Burchard, H., H. Schuttelaars, and A. Geyer, 2013: Residual sediment fluxes in weakly-to-periodically stratified estuaries and tidal inlets. *J. Phys. Oceanogr.*, **43** (9), 1841–1861, doi:10.1175/J.Phys.Oceanogr.-D-12-0231.1.
- Canuto, V., A. Howard, Y. Cheng, and M. Dubovikov, 2001: Ocean turbulence Part I: One-point closure model momentum and heat vertical diffusivities. *J. Phys.*

Oceanogr.

- Choi, B. H., K. O. Kim, and H. M. Eum, 2002: Digital bathymetric and topographic data for neighboring seas of Korea. *J. Korean Soc. Coast. Ocean Eng.*, **14** (1), 41–50.
- Christiansen, C., and Coauthors, 2002: Material transport from the nearshore to the basinal environment in the southern Baltic Sea: I. Processes and mass estimates. *J. Mar. Syst.*, **35** (3), 133–150.
- Cossu, R., and M. G. Wells, 2013: The interaction of large amplitude internal seiches with a shallow sloping lakebed: observations of benthic turbulence in Lake Simcoe, Ontario, Canada. *PLoS ONE*, **8** (3).
- Dade, W., A. Nowell, and P. Jumars, 1992: Predicting erosion resistance of muds. *Mar. Geol.*, **105** (1), 285–297.
- Ebner, R., 2015: Modelling of Surface Waves in the western Baltic Sea.
- Emeis, K., and Coauthors, 2002: Material transport from the near shore to the basinal environment in the southern Baltic Sea: II: synthesis of data on origin and properties of material. *J. Mar. Syst.*, **35** (3), 151–168.
- Emery, W. J., and R. E. Thomson, 2001: *Data Analysis Methods in Physical Oceanography*. 2nd ed., Elsevier, Amsterdam, NL, 638 pp.
- Endoh, T., Y. Yoshikawa, T. Matsuno, Y. Wakata, K.-J. Lee, and L. Umlauf, 2016: Observational evidence for tidal straining over a sloping continental shelf. *Cont. Shelf Res.*, **117**, 12–19.
- Feistel, R., G. Nausch, and N. Wasmund, 2008: *State and evolution of the Baltic Sea, 1952-2005: a detailed 50-year survey of meteorology and climate, physics, chemistry, biology, and marine environment*. John Wiley & Sons.
- Ferguson, R., and M. Church, 2004: A simple universal equation for grain settling velocity. *J. Sediment. Res.*, **74** (6), 933–937.
- Galperin, B., L. Kantha, S. Hassid, and A. Rosati, 1988: A quasi-equilibrium turbulent energy model for geophysical flows. *J. Atmos. Sci.*, **45** (1), 55–62.
- Garrett, C., 1991: Marginal mixing theories. *Atmos.-Ocean*, **29** (2), 313–339.
- Garrett, C., P. MacCready, and P. Rhines, 1993: Boundary mixing and arrested Ekman layers: Rotating stratified flow near a sloping bottom. *Ann. Rev. Fluid Mech.*, **25**,

291–323, doi:10.1146/annurev.fl.25.010193.001451.

- Goring, D. G., and V. I. Nikora, 2002: Despiking acoustic Doppler velocimeter data. *J. Hydraul. Eng.*, **128** (1), 117–126.
- Grant, J., U. Bathmann, and E. Mills, 1986: The interaction between benthic diatom films and sediment transport. *Estuar. Coast. Shelf S.*, **23** (2), 225–238.
- Grant, J., and G. Daborn, 1994: The effects of bioturbation on sediment transport on an intertidal mudflat. *Neth. J. Sea Res.*, **32** (1), 63–72.
- Grant, W. D., and O. S. Madsen, 1986: The continental-shelf bottom boundary layer. *Annu. Rev. Fluid Mech.*, **18** (1), 265–305.
- Hasselmann, K., 1974: On the spectral dissipation of ocean waves due to white capping. *Boundary-Layer Meteorology*, **6** (1-2), 107–127.
- Hasselmann, S., and K. Hasselmann, 1985: Computations and parameterizations of the nonlinear energy transfer in a gravity-wave spectrum. Part I: A new method for efficient computations of the exact nonlinear transfer integral. *J. Phys. Oceanogr.*, **15** (11), 1369–1377.
- Hinze, J. O., 1987: *Turbulence (2nd edition)*. McGraw-Hill, New York, USA, p.586.
- Holtermann, P. L., and L. Umlauf, 2012: The Baltic Sea tracer release experiment: 2. Mixing processes. *J. Geophys. Res. C: Oceans*, **117** (C1).
- Holthuijsen, L. H., 2007: *Waves in oceanic and coastal waters*. Cambridge University Press.
- Jay, D. A., and J. D. Musiak, 1994: Particle trapping in estuarine tidal flows. *J. Geophys. Res.: Oceans*, **99** (C10), 20 445–20 461.
- Jönsson, A., Å. Danielsson, and L. Rahm, 2005: Bottom type distribution based on wave friction velocity in the Baltic Sea. *Cont. Shelf Res.*, **25** (3), 419–435.
- Kahma, K. K., and C. J. Calkoen, 1992: Reconciling discrepancies in the observed growth of wind-generated waves. *J. Phys. Oceanogr.*, **22** (12), 1389–1405.
- Komen, G., K. Hasselmann, and K. Hasselmann, 1984: On the existence of a fully developed wind-sea spectrum. *J. Phys. Oceanogr.*, **14** (8), 1271–1285.

- Krone, R. B., 1962: Flume studies of the transport of sediment in estuarial shoaling processes.
- Kuhrts, C., W. Fennel, and T. Seifert, 2004: Model studies of transport of sedimentary material in the western Baltic. *J. Mar. Syst.*, **52** (1), 167–190.
- Lass, H., and V. Mohrholz, 2003: On dynamics and mixing of inflowing saltwater in the Arkona Sea. *J. Geophys. Res. C: Oceans*, **108** (C2).
- Lass, H., V. Mohrholz, and T. Seifert, 2001: On the dynamics of the Pomeranian Bight. *Cont. Shelf Res.*, **21** (11), 1237–1261.
- Lass, H., V. Mohrholz, and T. Seifert, 2005: On pathways and residence time of salt-water plumes in the Arkona Sea. *J. Geophys. Res. C: Oceans*, **110** (C11).
- Lass, H., and L. Talpsepp, 1993: Observations of coastal jets in the Southern Baltic. *Cont. Shelf Res.*, **13** (2), 189–203.
- Lefevre, F., C. Le Provost, and F. Lyard, 2000: How can we improve a global ocean tide model at a regional scale? A test on the Yellow Sea and the East China Sea. *J. Geophys. Res.*, **105** (C4), 8707–8725.
- Leipe, T., A. Loeffler, K.-C. Emeis, S. Jaehmlich, R. Bahlo, and K. Ziervogel, 2000: Vertical patterns of suspended matter characteristics along a coastal-basin transect in the western Baltic Sea. *Estuarine Coastal Shelf Sci.*, **51** (6), 789–804.
- Leipe, T., M. Naumann, F. Tauber, H. Radtke, and H. W. Arz, 2016: Geochemical mapping of German Baltic Sea sediments and relevance (connection) to ecosystem functioning. *J. Mar. Syst.*, *submitted*.
- Lorke, A., V. Mohrholz, and L. Umlauf, 2008: Stratification and mixing on sloping boundaries. *Geophys. Res. Lett.*, **35** (L14610), doi:10.1029/2008GL034607.
- Lorke, A., F. Peeters, and A. Wüest, 2005: Shear-induced convective mixing in bottom boundary layers on slopes. *Limnol. Oceanogr.*, **50** (5), 1612–1619.
- Lorrai, C., L. Umlauf, J. Becherer, A. Lorke, and A. Wüest, 2011: Boundary mixing in lakes. 2. Combined effects of shear-induced and convective turbulence on basin-scale mixing. *J. Geophys. Res.*, **116**, C10 018, doi:10.1029/2011JC007121.
- MacCready, P., and W. R. Geyer, 2010: Advances in Estuarine Physics. *Annu. Rev. Marine. Sci.*, **2**, 35–58.

- MacCready, P., and W. R. Geyer, 2014: The estuarine circulation. *Ann. Rev. Fluid Mech.*, **46**, 175–197, doi:10.1146/annurev-fluid-010313-141302.
- Meier, H. M., and Coauthors, 2006: Ventilation of the Baltic Sea deep water: A brief review of present knowledge from observations and models. *Oceanologia*, **48 (S)**.
- Mellor, G. L., and T. Yamada, 1982: Development of a turbulence closure model for geophysical fluid problems. *Rev. Geophys.*, **20 (4)**, 851–875.
- Mohrholz, V., M. Naumann, G. Nausch, S. Krüger, and U. Gräwe, 2015: Fresh oxygen for the Baltic Sea—An exceptional saline inflow after a decade of stagnation. *J. Mar. Syst.*, **148**, 152–166.
- Nielsen, P., 1992: *Coastal bottom boundary layers and sediment transport*, Vol. 4. World scientific.
- Pizarro, O., and G. Shaffer, 1998: Wind-driven, coastal-trapped waves off the Island of Gotland, Baltic Sea. *J. Phys. Oceanogr.*, **28 (11)**, 2117–2129.
- Pope, S. B., 2000: *Turbulent Flows*. Cambridge University Press, Cambridge, UK, 806 pp.
- Pritchard, D. W., 1952: Salinity distribution and circulation in the Chesapeake Bay estuarine system. *J. Mar. Res.*, **11 (2)**, 106–123.
- Reissmann, J. H., and Coauthors, 2009: Vertical mixing in the Baltic Sea and consequences for eutrophication—A review. *Prog. Oceanogr.*, **82 (1)**, 47–80.
- Rodi, W., 1987: Examples of calculation methods for flow and mixing in stratified fluids. *J. Geophys. Res. C: Oceans*, **92 (C5)**, 5305–5328.
- Rodi, W., 1993: *Turbulence models and their application in hydraulics*. CRC Press.
- Sander, J., 1998: Dynamical equations and turbulent closures in geophysics. *Continuum Mech. Thermodyn.*, **10 (1)**, 1–28.
- Sanford, L., and M.-L. Chang, 1997: The bottom boundary condition for suspended sediment deposition. *J. Coastal Res.*, 3–17.
- Sassi, M., M. Duran-Matute, T. van Kessel, and T. Gerkema, 2015: Variability of residual fluxes of suspended sediment in a multiple tidal-inlet system: the Dutch Wadden Sea. *Ocean Dynam.*, **65 (9-10)**, 1321–1333.

- Schulz, E., H. M. Schuttelaars, U. Gräwe, and H. Burchard, 2015: Impact of the depth-to-width ratio of periodically stratified tidal channels on the estuarine circulation. *J. Phys. Oceanogr.*, (2015).
- Schulz, K., and L. Umlauf, 2016: Residual transport of suspended material by tidal straining near sloping topography. *J. Phys. Oceanogr.*, doi:10.1175/JPO-D-15-0218.1, in press.
- Schwartz, M., 2006: *Encyclopedia of coastal science*. Springer Science & Business Media.
- Scully, M. E., and C. T. Friedrichs, 2003: The influence of asymmetries in overlying stratification on near-bed turbulence and sediment suspension in a partially mixed estuary. *Ocean Dynam.*, **53** (3), 208–219, doi:10.1007/s10236-003-0034-y.
- Scully, M. E., and C. T. Friedrichs, 2007: Sediment pumping by tidal asymmetry in a partially mixed estuary. *J. Geophys. Res.: Oceans*, **112** (C7).
- Seifert, T., W. Fennel, and C. Kuhrt, 2009: High resolution model studies of transport of sedimentary material in the south-western Baltic. *J. Mar. Syst.*, **75** (3), 382–396.
- Simpson, J. H., 1997: Physical processes in the ROFI regime. *J. Mar. Sys.*, **12**, 3–15.
- Simpson, J. H., J. Brown, J. Matthews, and G. Allen, 1990: Tidal straining, density currents, and stirring in the control of estuarine stratification. *Estuaries Coasts*, **13**, 125–132.
- Simpson, J. H., H. Burchard, N. R. Fisher, and T. P. Rippeth, 2002: The semi-diurnal cycle of dissipation in a ROFI: model-measurement comparisons. *Cont. Shelf Res.*, **22**, 1615–1628.
- Swart, D. H., 1974: Offshore sediment transport and equilibrium beach profiles. Ph.D. thesis, TU Delft, Delft University of Technology.
- Tauber, F., 2012: Meeresbodensedimente in der deutschen Ostsee/Seabed sediments in the German Baltic Sea.
- Thorpe, S. A., 2005: *The Turbulent Ocean*. Cambridge University Press, Cambridge, UK, 439 pp.
- Umlauf, L., and H. Burchard, 2003: A generic length-scale equation for geophysical turbulence models. *J. Mar. Res.*, **61**, 235–265.

- Umlauf, L., and H. Burchard, 2005: Second-order turbulence closure models for geophysical boundary layers. A review of recent work. *Cont. Shelf Res.*, **25**, 795–827.
- Umlauf, L., and H. Burchard, 2011: Diapycnal transport and mixing efficiency in stratified boundary layers near sloping topography. *J. Phys. Oceanogr.*, **41** (2), 329–345, doi:10.1175/2010J.Phys.Oceanogr.4438.1.
- Umlauf, L., H. Burchard, and K. Bolding, 2005: GOTM – Scientific Documentation. Version 3.2. Marine Science Reports 63, Leibniz-Institute for Baltic Sea Research, Warnemünde, Germany.
- Umlauf, L., W. D. Smyth, and J. N. Moum, 2015: Energetics of bottom Ekman layers during buoyancy arrest. *J. Phys. Oceanogr.*, **45** (12), 3099–3117.
- Uncles, R. J., R. C. A. Elliott, and S. A. Weston, 1985: Observed fluxes of water, salt and suspended sediment in a partly mixed estuary. *Estuar. Coast. Shelf S.*, **20** (2), 147–167.
- van Aken, H. M., 1986: The onset of seasonal stratification in shelf seas due to differential advection in the presence of a salinity gradient. *Cont. Shelf Res.*, **5**, 475–485.
- Van der Lee, E., and L. Umlauf, 2011: Internal wave mixing in the Baltic Sea: Near-inertial waves in the absence of tides. *J. Geophys. Res. C: Oceans*, **116** (C10).
- Van Leussen, W., 1988: Aggregation of particles, settling velocity of mud flocs a review. *Physical processes in estuaries*, Springer, 347–403.
- van Rijn, L. C., 1984a: Sediment transport, part I: bed load transport. *J. Hydraul. Eng.*, **110** (10), 1431–1456.
- van Rijn, L. C., 1984b: Sediment transport, part II: suspended load transport. *J. Hydraul. Eng.*, **110** (10), 1613–1641.
- Wakata, Y., T. Endoh, and Y. Yoshikawa, 2016: Transformation and disintegration of strongly nonlinear internal waves by topography in stratified lakes. *Cont. Shelf Res.*, (submitted).
- Wilcox, D. C., and Coauthors, 1998: *Turbulence modeling for CFD*, Vol. 2. DCW industries La Canada, CA.
- Wubber, C., and W. Krauss, 1979: The two dimensional seiches of the Baltic Sea. *Oceanologica Acta*, **2** (4), 435–446.

- Xianwen, B., G. Guoping, and Y. Ju, 2001: Three dimensional simulation of tide and tidal current characteristics in the east china sea. *Oceanologica Acta*, **24 (2)**, 135–149.
- Yoshikawa, Y., T. Matsuno, T. Wagawa, T. Hasegawa, K. Nishiuchi, K. Okamura, H. Yoshimura, and Y. Morii, 2012: Tidal and low-frequency currents along the CK Line (31deg 45min N) over the East China Sea shelf. *Cont. Shelf Res.*, **50**, 41–53.
- Zijlema, M., G. P. van Vledder, and L. Holthuijsen, 2012: Bottom friction and wind drag for wave models. *Coastal Eng.*, **65**, 19–26.